Dissertation

submitted to the

Combined Faculties for the Natural Sciences and for Mathematics

of the Ruperto-Carola University of Heidelberg, Germany

for the degree of

Doctor of Natural Sciences

by

MSc. (Biology), Fabian Nicolas Svara

Born in: Paris, France

Oral examination date: February 3, 2017

Volume Electron Microscopic Analyses in the Larval Zebrafish

Referees

Prof. Dr. Joachim Wittbrodt

Dr. Johann Bollmann

Dedicated to my parents.

Declaration according to §8 (3) b) and c) of the doctoral degree regulations:

b) I hereby declare that I have written the submitted dissertation myself and in this process have used no other sources of materials than those expressly indicated;

c) I hereby declare that I have not applied to be examined at any other institution, nor have I used the dissertation in this or any other form at any other institution as an examination paper, nor submitted it to any other faculty as a dissertation.

Munich, November 20th, 2016

Fabian Svara

Parts of this thesis are being prepared for publication

Authors: F. Svara, J. Kornfeld, W. Denk, J. Bollmann

Working Title: Wiring-specificity in a larval zebrafish premotor network

Poster Presentations

IZN (Interdisziplinäres Zentrum für Neurowissenschaften) Retreat
Schöntal 2011, 2012, 2013

Janelia Farm / Max Planck High Resolution Circuit Reconstruction Conference
Ashburn 2011, Berlin 2014

Society for Neuroscience Annual Meeting
New Orleans 2012, Washington 2013, San Diego 2014, San Diego 2016

Zebrafish Imaging Meeting
London 2012

The Assembly and Function of Neuronal Circuits Conference
Ascona 2015

Talks

IZN (Interdisziplinäres Zentrum für Neurowissenschaften) Seminar
Heidelberg 2015

Janelia Farm / Max Planck High Resolution Circuit Reconstruction Conference
Ashburn 2016

Acknowledgments

I am indebted to many people without whom this work would not have been possible.

Dr. Johann Bollmann for excellent supervision, for being open to starting this project in his lab and many constructive discussions. Prof. Dr. Winfried Denk, for luring me into a PhD project at the Max Planck Institute in Heidelberg and teaching me how to do science properly.

Prof. Dr. Jochen Wittbrodt, for agreeing to be my first supervisor. Prof. Dr. Ilme Schlichting for constructive criticism during TAC meetings. Prof. Dr. Christoph Schuster and Prof. Dr. Thomas Kuner for kindly agreeing to be part of my examination committee.

My friends and colleagues Dr. Chintan Trivedi, Dr. Stephanie Preuß and Jörgen Kornfeld for making work enjoyable, for many exciting and inspiring discussions.

Dr. Kevin Briggman for teaching me EM stainings and the basics of SBEM when I was just getting started. Dr. Jens Gabriel for showing me everything around the lab and teaching me how to use the two-photon microscope. Dr. Benjamin Titze for many helpful discussions about SBEM.

Prof. Dr. Herwig Baier and Dr. Fumi Kubo for a fruitful and effective collaboration on imaging of pretectal cells in the opto-kinetic response.

The great IT group at MPI Heidelberg, especially Chris Roome, Mario Hilpert and Thomas Stather, for being open to any kind of request and pretty much allowing Jörgen and me to run wild.

The wonderful electronics workshop in Heidelberg, in particular Jürgen Tritthardt for designing, building and always being happy to explain highly advanced electronics. The mechanical workshop, in particular Niklas Neef and Martin Lukat for always being available to help, even on short notice, with any microtome issues.

Fabienne Höfer-Elfner, Dominique Finkler, Vanessa Würges and Jutta Knaupp from the HR department in Heidelberg, who made it possible for Jörgen and me to maintain a small army of annotators.

The Heidelberg HiWi team, in particular Anna Biasotto, Annika Gable, Malte Grohmann, Hannah Jakobi, Liesa-Marie Schreiber and Ji-Hyun Youm who helped with the management of the army and made it all enjoyable. Many HiWis for contributing tracings: Enoch Antwo Boasiako, Anne Bamberg, Ilka Bartsch, Elisabeth Bau, Jenny Bauer, Alexandra Becker, Julia Benzinger, Abin Biswas, Martin Bochenek, Georg Boeing, Antonia Brings, Arne Buntjer, Karin Bustamente, Karina Böhm, Veronika Chevyreva, Matthäus Cieciera, Raphael Dietrich, Sven Dorkenwald, Wiebke Dürichen, Konstantin Eckel, Jan-Dirk Eckert, Niclas Engler, Raphael Erich, Kristina Ernst, Larissa Felgner, Alexander Fischer, Kai Fischer, Sebastian Flassbeck, Stephanie Freiß, Sebastian Fried, Sebastian Gippert, Robert-Ionut Glavan, Frederik Golibrzuch, Kathrin Gundel, Marleen Hanelt, Wladislav Hartmann, Katharina Hasch, Sebastian Hendricks, Johanna Herrmann, Sebastian Hess, Maret Heumannskaemper, Timm Hondrich, Lisa Hornung, Phillip Hottinger, Udo Häusler, Felix Hüting, Federica Inturrisi, Kevin Juaire, Evangeline Kang, Hannes Kettner, Bakhodur Khakimov, Severina Klaus, Richard Knorr, Christian Koellen, Sanne Kwakman, Henrik Landerer, Lukas Lehmann, Jonas Lehmann, Benjamin Lohrer, Mechthild Lütge, Maximilian Mastall, Christian Mauch, Lukas Merz, Jennifer Meyer, Ninja Münster, Nina Nasresfahani, Andreas Ochs, Sadia Oumohand, Bjoern Peter, Miriam Pohrath, Matthäus Prokscha, Shahid Rafique, Anna Reiling, Tobias Reimann, Maximilian Reinert, Marius Rimmler, Lukas Riso, Mohamed Salem, Vadim Saratov, Victoria Sauer, Sven Schaffer, Lara-Marie Schmitt, Lisa Schubert, Raphael Schumann, Constanza Schönfeld, Michelle Sebastian, Elisabeth Serger, Julian Sieber, Sonja Simon, Regina Specht, Anna Steinmann, Simon Tamyalew, Karen Tessmer, Dennis Ulmer, Florian Viehweger, John Walden, Nadine Waltrich, Anselm Weber, Jasmin Weber, Marco Werr, Katja Wiegert, Monika Witzenberger, Philipp Worst, Arlie Zegarra, Tobias Ziegler and Katharina Ziegler.

Boehringer Ingelheim Fonds and Max Planck Society for financial support.

My family for supporting me throughout all this time.

Contents

Summary

The goal of this work was two-fold: 1) To apply serial block-face electron microscopy (SBEM) to the spinal cord of a larval zebrafish, in order to gain a mechanistic understanding of motoneuron (MN) recruitment, based on a reconstruction of the wiring between spinal interneurons and MNs and 2) to implement technological improvements to SBEM that would allow datasets to be acquired at much higher speed, in order to acquire a dataset of a complete larval zebrafish brain.

The spinal cord of vertebrates contains a neural circuit known as a central pattern generator (CPG), which can generate the rhythmic muscle contractions underlying locomotion independently of the brain. In fish, the rhythm consists of muscle contractions that alternate between the left and right side of the tail and that travel down the length of the fish, from head to tail. When swimming fast, such as during escapes, the rhythm has a high frequency and muscles contract vigorously. During slow, routine swimming, the rhythm has a low frequency and muscles contract with less strength. The MNs in the spinal cord, which elicit the contractions of the tail musculature, are recruited to different degrees during these different behaviors. With increasing contraction strength, more and larger MNs are activated. This phenomenon is called orderly recruitment. The rhythmic excitation that recruits MNs is provided by Circumferential Descending (CiD) interneurons located in the spinal cord. These interneurons also follow a specific recruitment pattern: During weak swimming, ventral cells are active exclusively and dorsal cells are silent. As swims increase in vigor, the activity in these cells shifts towards more dorsal cells, with more ventral cells becoming inactive.

The aim of the first part of this thesis was to reconstruct the MNs along with the CiDs that excite them, using a high resolution SBEM dataset of the spinal cord, to identify the pattern of connectivity between these types of neurons and distinguish between competing hypotheses of orderly MN recruitment. Conceptually, orderly recruitment could either be implemented with unspecific connectivity, in which case it would be a consequence of the interplay of size-

dependent biophysical properties (in particular the input resistance) with the strengths of the synapses driving them. Alternatively, the wiring pattern could be specific and the CiDs could select the subset of MNs to activate by making synapses with just those cells.

MNs in the larval zebrafish spinal cord clustered into distinct subtypes, depending on their size: Small, intermediate and large. The small MNs received almost no synaptic inputs and appeared to be immature. CiDs differentially innervated the intermediate and large MNs: Ventrally located CiDs did not differentiate between the two subtypes, but the dorsal CiDs made synapses onto large MNs with high specificity. Since dorsal CiDs are active only during the fastest swims, this finding can be interpreted as a labeled line specifically recruiting the strongest MNs during the most vigorous behaviors. During weaker behaviors, when the dorsal CiDs are inactive and the more ventral ones are active exclusively, differences in MN excitability due to size would encode the recruitment order.

The second objective was to improve SBEM technology to acquire a whole larval zebrafish brain in a relatively short period of time. Due to the very high resolution required to trace small neurites and to identify synapses, even very small brains, such as the brain of a larval zebrafish, would take many months to acquire using a typical SBEM setup. Two main techniques were used to increase net speed. First, line-scanning of individual image tiles was implemented, where the electron beam scans the image in one axis only and the other axis is scanned by moving the stage. This allows larger individual images to be taken, greatly reducing the number of motor moves between images. Second, dynamic adaptation of the image tile mosaic to the shape of the sample was used to avoid scanning the blank plastic regions surrounding an irregularly shaped sample.

These improvements allowed the complete brain of a 5 day old larval zebrafish to be imaged in less than 30% of the time than would have been required previously. In a collaborative project with Dr. Fumi Kubo, two-photon calcium imaging was performed prior to EM imaging, revealing pretectal cells active during optokinetic stimulation. The two-photon dataset was successfully

registered to the EM data and a functionally identified pretectal cell could be traced. This dataset will be used to reconstruct the complete neural networks that compute the optokinetic response.

Zusammenfassung

Diese Arbeit hatte zwei Ziele: 1) Serielle Elektronenmikroskopie der Blockoberfläche (SBEM) im Rückenmark der Zebrafischlarve anzuwenden, um, basierend auf der Rekonstruktion der Verschaltungsmuster zwischen spinalen Interneuronen und Motoneuronen (MNs), zu einem mechanistischen Verständnis der Rekrutierung von MNs zu gelangen und 2) die SBEM-Akquisitionsgeschwindigkeit durch technologische Verbesserungen zu erhöhen, um einen Datensatzes des gesamtes Gehirns der Zebrafischlarve aufzunehmen.

Das Rückenmark von Wirbeltieren enthält ein Netzwerk von Nervenzellen, das als zentraler Mustergenerator bezeichnet wird. Dieses Netzwerk kann, unabhängig vom Gehirn, rhythmische Muskelkontraktionen produzieren, die der Fortbewegung des Tieres zu Grunde liegen. Bei Fischen heißt das, dass Muskelkontraktionen zwischen der linken und rechten Seite des Schwanzes alternieren, wobei die Kontraktionen den Schwanz in Richtung Schwanzende entlanglaufen. Wenn der Fisch schnell schwimmt, wie zum Beispiel bei Fluchtbewegungen, hat dieser Rhythmus eine hohe Frequenz und die Muskeln kontrahieren stark. Während langsamer Routinebewegungen hat der Rhythmus eine niedrige Frequenz und die Muskeln kontrahieren nur leicht. Die MNs im Rückenmark werden bei diesen unterschiedlichen Bewegungsmustern unterschiedlich aktiviert: Je stärker die Bewegung, desto mehr MNs und desto größere MNs werden aktiviert. Dieses Phänomen wird als geordnete Rekrutierung („orderly recruitment“) bezeichnet. Die rhythmische Erregung der MNs stammt von Circumferential Descending Interneuronen (CiDs) des Rückenmarks. Diese folgen ebenfalls einem speziellen Rekrutierungsmuster: Während langsamer Schwimmbewegungen sind ventrale Zellen exklusiv aktiv und dorsale inaktiv. Bei stärkeren Bewegungen verschiebt sich die Aktivität der CiDs zu dorsaleren Zellen, wobei die ventraleren inaktiv werden.

Das Ziel des ersten Teils dieser Arbeit war es, die MNs zusammen mit den CiDs, die diese rhythmisch erregen, mit Hilfe eines SBEM-Datensatzes zu rekonstruieren. Damit sollte das Verschaltungsmuster zwischen diesen zwei

Neuronentypen analysiert werden, um zwischen verschiedenen Hypothesen über die geordnete MN-Rekrutierung zu unterscheiden. Zwei konzeptionell unterschiedliche Mechanismen wären denkbar: Die geordnete Rekrutierung könnte bei zufälliger, unspezifischer Verschaltung aus dem Zusammenspiel von größenabhängigen biophysikalischen Zelleigenschaften (vor Allem dem Eingangswiderstand) mit Synapsen unterschiedlicher Stärke resultieren. Alternativ könnte das Verschaltungsmuster aber auch spezifisch sein und die CiDs könnten nur Synapsen auf genau jene MNs bilden, die sie aktivieren müssen.

MNs im Rückenmark der Zebrafischlarve bildeten drei Cluster, die sich in der Somagröße unterschieden: Kleine, mittlere und große MNs. Die kleinen MNs scheinen zu diesem Zeitpunkt noch unreif zu sein, da sie fast keine synaptischen Eingänge erhielten. Die mittleren und großen MNs wurden von CiDs differenziell innerviert: Ventral gelegene CiDs unterschieden nicht zwischen den beiden Klassen, aber die dorsalen CiDs bildeten mit hoher Spezifität Synapsen auf große MNs. Da dorsale CiDs nur während der schnellsten Schwimmbewegungen aktiv werden, kann dieses Resultat als eine dedizierte Leitung interpretiert werden, die beim schnellen Schwimmen speziell große MNs aktiviert. Während schwächerer Schwimmbewegungen, wenn die dorsalen CiDs inaktiv und nur die ventralen CiDs aktiv sind, würden Unterschiede in der Erregbarkeit unterschiedlich großer MNs die Rekrutierungsreihenfolge festlegen.

Das Ziel des zweiten Teils dieser Arbeit war, technische Verbesserungen der SBEM-Technologie zu realisieren, um einen Datensatz des kompletten Gehirns der Zebrafischlarve in relativ kurzer Zeit aufnehmen zu können. Auf Grund der hohen Auflösung, die benötigt wird, um kleine Neurite zu verfolgen und Synapsen zu identifizieren, würde es Monate dauern, selbst kleine Gehirne wie das der Zebrafischlarve mit SBEM aufzunehmen. Der Fokus des zweiten Teils der Arbeit war daher, die Akquisitionsgeschwindigkeit von SBEM zu erhöhen. Zwei Techniken wurden dazu eingesetzt. Erstens wurde das “line-scanning” von Einzelbildern implementiert. Dabei rastert der Elektronenstrahl nur eine Achse des Bildes ab, während die andere Achse durch das Verfahren des Probentisches gerastert wird. Das ermöglicht die Aufnahme von größeren

Einzelbildern, wodurch die Probe zwischen den Aufnahmen der Einzelbilder weniger häufig verfahren werden muss. Zweitens wurde das Einzelbilder-Mosaik präzise an die unregelmäßige Form der Probe angepasst, sodass vermieden werden konnte, unnötigerweise das Plastik, das die Probe umgibt, in den Datensatz mit aufzunehmen.

Diese Verbesserungen erlaubten es, das komplette Gehirn einer 5 Tage alten Zebrafischlarve in weniger als 30% der Zeit, die vorher benötigt worden wäre, aufzunehmen. In Zusammenarbeit mit Dr. Fumi Kubo waren zuvor im gleichen Fisch mit Hilfe von Zwei-Photonen Calcium-Bildgebung Zellen des Prätektums identifiziert worden, die bei optokinetischer Stimulation aktiviert wurden. Der Zwei-Photonen-Datensatz konnte erfolgreich mit den EM-Daten registriert werden und eine der funktional identifizierten Zellen wurde bereits vollständig rekonstruiert. Dieser Datensatz wird dazu verwendet werden, die Schaltkreise zu rekonstruieren, die dem optokinetischen Reflex zu Grunde liegen.

Introduction

“[The brain] is basically an alien technology.”

— Terrence Sejnowski

Brains allow animals and humans to extract a precise, abstract understanding of their dynamic environment from fleeting and noisy sensory inputs. This understanding is integrated with memories of similar situations encountered in the past and with models of the external world to decide on a course of action, in order to attain a rewarding goal or to withdraw from a dangerous situation. Eventually, a sequence of muscle contractions is produced, putting that decision into practice. Yet, as the above quote by Terrence Sejnowski succinctly states, we are still far removed from understanding how brains work in a comprehensive, mechanistic fashion. While computer science has made progress in building systems exhibiting some of the abilities formerly thought to be exclusive to brains, human technology still is unable to match many of the brain’s capabilities. Airplanes don’t pilot themselves, machines can’t play complex video games effectively and only humans understand language, to name but a few examples. In fact, how the brain can do all these things remains to a large degree uncharted territory.

One of the central reasons for our lack of understanding of brains is the complexity of the neural networks that comprise them. That complexity is due, for one, to the large diversity of different parts, i.e. neuronal cell types, making up a nervous system. For example, even the relatively simple mouse retina contains over 60 different cell types (Masland, 2012). More important, however, is the combinatorial complexity due to the dense inter-connectivity of neurons. This is illustrated by a simple calculation for a comparatively simple brain, that of the larval zebrafish, *Danio rerio*: Assuming a number of 80’000 neurons in the larval zebrafish (Hill et al., 2003), each of which could in principle be connected to any other neuron in the brain, there exist $2^{\binom{80000}{2}} > 10^{100000000}$ distinct ways of connecting these neurons, without yet accounting for any

Figure 1 | Comparison of the volumes of different published volume EM stacks and of the volumes of small animal brains.

differences in strength between these connections. Therefore, attempts at mechanistically understanding the neural networks that make up a brain at the level of individual neurons, using paired electrophysiological recordings or even large-scale optophysiological recordings from thousands of cells (Ahrens et al., 2013), can only provide limited insight.

Electron Microscopy based Circuit Reconstruction

The complexity of biological neural networks might become more tractable if the complete set of neurons and their connections were known. Such a wiring diagram could, at the very least, be used to quickly falsify mechanistic hypotheses about how neural networks implement specific behaviors (Denk et al., 2012). Since the diameter of an unmyelinated axon can be as low as 100 nm and individual synaptic vesicles have diameters of on the order of 50 nm (Gray, 1959), neural tissue must be imaged at very high resolution and speed to make it feasible to measure such a wiring diagram.

Recently, automated and semi-automated serial electron microscopy (EM) techniques have been developed to enable this task (reviewed in Briggman and Bock (2012)). These techniques all start with tissue fixation and *en bloc* staining with heavy metals, followed by plastic embedding, yielding a relatively inert, solid block of neural tissue. The block can subsequently be thinly sectioned, in the range of 5 – 40 nm. The sectioning is performed either using a diamond knife or a focused ion beam. Then, either the individual sections are imaged using Transmission Electron Microscopy (TEM) or Scanning Electron Microscopy (SEM) or the block face is imaged using SEM. The individual images are registered into a consistent volume on which analysis proceeds. The datasets obtained in this fashion are currently still relatively small compared to mammalian brains, but the largest ones produced to date are reaching the size range of the brains of small animals, such as the adult *Drosophila melanogaster* or larval zebrafish (Figure 1).

Descriptions of the major volume EM techniques are provided here for context, but all experimental work and methodological improvements described in this thesis were performed using Serial Block-Face Scanning Electron Microscopy (SBEM).

Serial Sectioning Transmission Electron Microscopy (ssTEM) is the oldest of these techniques, having been used in a fully manual fashion for classic work such as the imaging of a complete nervous system of *Caenorhabditis elegans* (White et al., 1986). In this approach, a person manually sections a block of tissue using an ultramicrotome and collects the individual sections on grids. The grids are later imaged destructively using TEM. Recent advances in imaging throughput, using charge coupled device (CCD) camera arrays (Bock et al., 2011), have made it more practical to use the technique to acquire relatively large datasets. Additionally, automatic section loading devices have been developed to further improve throughput through (semi-)automation (Bock, personal communication).

In Automatic Tape-Collecting Ultramicrotomy (ATUM) (Kasthuri et al., 2015), a regular ultramicrotome is modified for automatic operation by fitting it with a tape-collection mechanism, where individual thin sections float across a surface

of water to be collected on conductive tape. The tape is mounted on wafers and made conductive by coating with a conductive material. The wafers can then be imaged non-destructively in a random access fashion using SEM. Sections can be re-imaged multiple times at different resolution levels, so that high-resolution imaging can be targeted to specific regions of interest after first inspecting a lower resolution image.

Focused Ion Beam Milling Scanning Electron Microscopy (FIB-SEM) is a block-face imaging technique. That is, material is destructively removed from the surface of the sample and the freshly created surface is imaged using SEM. By

	ssTEM	**SBEM**	**ATUM**	**FIB-SEM**
Typical image resolution [nm]	4	10	4	5
Typical section thickness [nm]	40	25	30	5
Typical tile edge length [µm]	21	30	65	10
Typical pixel acquisition rate [MHz]	27.6	5	9.8	0.1
Typical tile overhead [s]	1	3	1	1
Typical sectioning overhead [s]	400	45	360	30
Unattended operation?	no	yes	yes	yes
Zebrafish brain				
Bounding box dimensions [µm]: 450 (Left-Right), 700 (Rostro-Caudal), 320 (Dorso-Ventral)				
Oblique cutting orientation (714.8 µm travel)				
# Tiles per section	100	50	11	
# Sections	17870	28592	23826	
Total imaging time [d]	21	29.6	78.8	
Total tile overheads [d]	20.8	48.3	2.6	
Total cutting time [d]	82.7	14.9	99.3	
Total time [d]	124.5	92.8	180.7	

Table 1 | Comparison of different volume EM techniques. Data from (Briggman and Bock, 2012), updated to reflect current developments. The estimates for the zebrafish brain are for a sample cut in a plane rotated 35° in yaw from the transversal plane (see Results for additional details on cutting orientation). Tile-tile overlap is not taken into account for these estimates. No time estimates for the zebrafish brain are provided in the case of FIB-SEM, since that technique can currently not be applied to samples of such a large size.

using a focused beam of ions, typically Ga^+, very thin layers can be removed even from surfaces that have been heavily electron dosed previously during imaging. This makes FIB-SEM the volume EM technology that delivers the highest resolution along all axes. However, it is currently severely limited by difficulties in milling large surfaces and can therefore only be applied to relatively small samples (Knott et al., 2008). Current research is aimed at mitigating this limitation by developing reliable techniques to cut large samples into smaller pieces that can then be imaged independently, without any data loss at the cuts (Hayworth et al., 2015).

Serial Block-Face Scanning Electron Microscopy (SBEM) is a diamond-knife based block-face imaging technology. As in FIB-SEM, material is serially removed from the surface of a block and the block-face is imaged (Denk and Horstmann, 2004). The use of a diamond knife instead of an ion beam allows much larger surfaces to be cut than with ion beams, at the cost of an increased section thickness. Electron-beam-induced surface damage due to imaging makes it more difficult to reliably obtain thin cuts, creating a tradeoff between beam current and voltage (and therefore image noise level) on the one hand and cutting thickness on the other hand.

The different serial EM techniques introduced here have different advantages and drawbacks (Table 1) (also reviewed in Briggman and Bock (2012)). Generally, techniques that rely on imaging sections can provide high axial resolution, but require relatively thick cuts. FIB-SEM can provide both high axial and sectioning resolution, at the cost of slow operation and limited field of view. Block-face imaging in general eliminates issues related to section handling, such as folding and tearing. It causes minimal distortions to the individual slice images and thus requires less sophisticated post-processing for image registration. Due to these properties and due to the possibility of fully unattended operation, SBEM is currently a strong candidate for the acquisition of relatively large datasets.

Technical Challenges

The challenges inherent to volume electron microscopy based neural circuit reconstruction are mainly consequences of 1) the high resolution required to follow neurites and identify synapses, which is on the order of 10 nm and 2) the volume typically required to be able to reconstruct entire neurons and their connections, which is very large relative to the size of a voxel and on the order of hundreds of micrometers. This means that both acquiring datasets within reasonable time frames and reconstructing connectivity from the raw data present significant challenges. This has, up to now, limited the sizes of datasets acquired, with the largest published dataset, acquired using ssTEM, being $\approx 8.2 \cdot 10^6$ µm³ in size (Bock et al., 2011). This is close to the size of the *Drosophila melanogaster* adult brain, but more than four times smaller than the brain of a 6 day post fertilization (dpf) larval zebrafish (Figure 1).

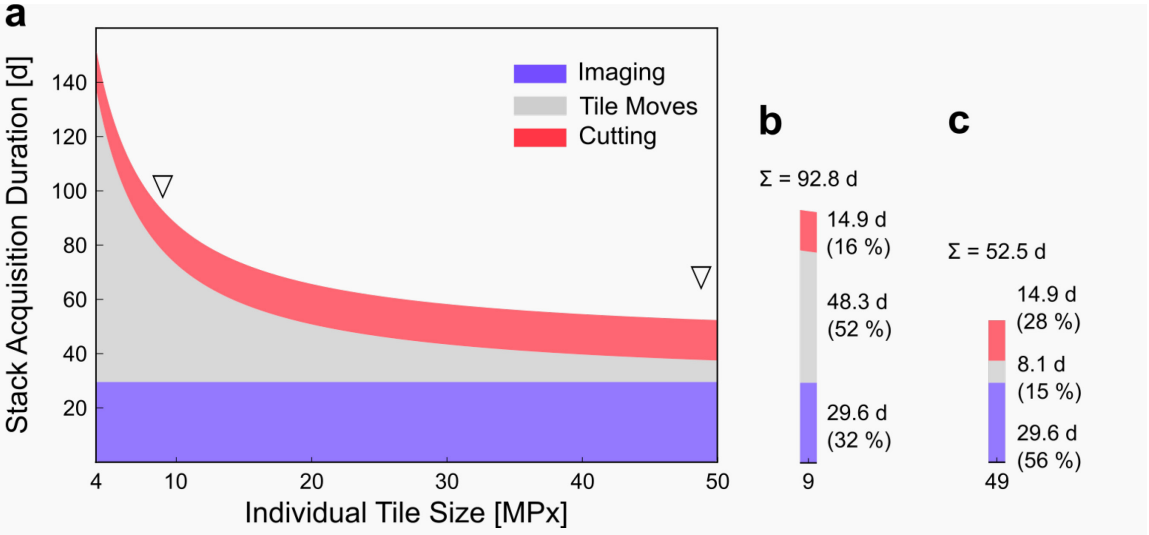

Figure 2 | Decomposition of SBEM acquisition time for a whole larval zebrafish brain. (**a**) Dependence of the acquisition time on the size of individual tiles. Arrowheads point at tile sizes shown in (b) and (c). (**b**) The total acquisition time is > 3 months, dominated by tile moves, at a typical individual tile size of 9 MPx. (**c**) The total acquisition time is less than 2 months, with negligible time spent on tile moves, at a tiles size of 49 MPx.

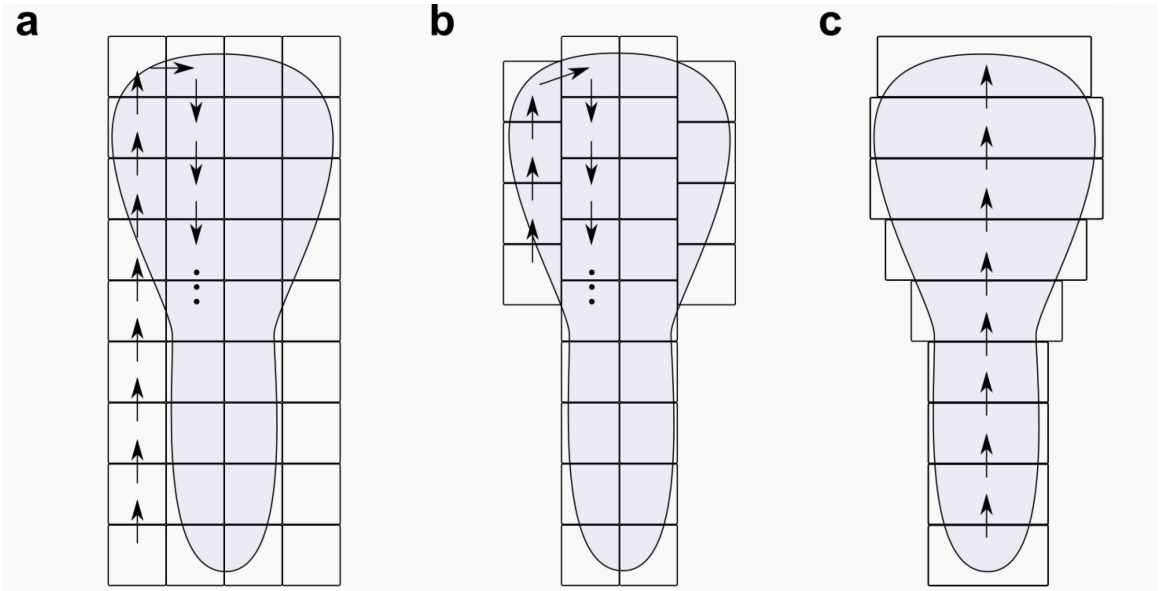

Figure 3 | Different tiling strategies for SBEM. (**a**) Standard rectangular tile pattern. Considerable imaging time is wasted when the sample geometry is irregular and many motor moves are required between individual tiles. (**b**) Adaptive tiling. The tile pattern is adapted to an irregular sample geometry. (**c**) Adaptive tiling with line scanning. In addition to adapting the tile pattern and tile geometry to the sample, individual tiles are very long on one axis, avoiding many motor moves.

The following sections provide a brief overview of the specific factors currently limiting our ability to acquire larger datasets, with a focus on SBEM, and introduce the technical improvements implemented in this thesis to help overcome these problems.

Acquisition of Large Datasets in SBEM

The time spent to acquire a dataset in SBEM can be decomposed into 1) the time required for cutting, 2) the time required for image scanning and 3) the overheads associated with image scanning (Figure 2).

Fields of view that are larger than the maximal size for an individual image need to be stitched together from multiple partly overlapping smaller images, called tiles. On the instrument used in this thesis (see Methods), the tile size is in the range of 40 µm. To acquire a mosaic of many tiles, the sample must be moved between imaging positions. These motor moves constitute the bulk of the image scanning overhead, each requiring on the order of 3 s. Since less of these moves are required when individual image tiles are larger, the size of the

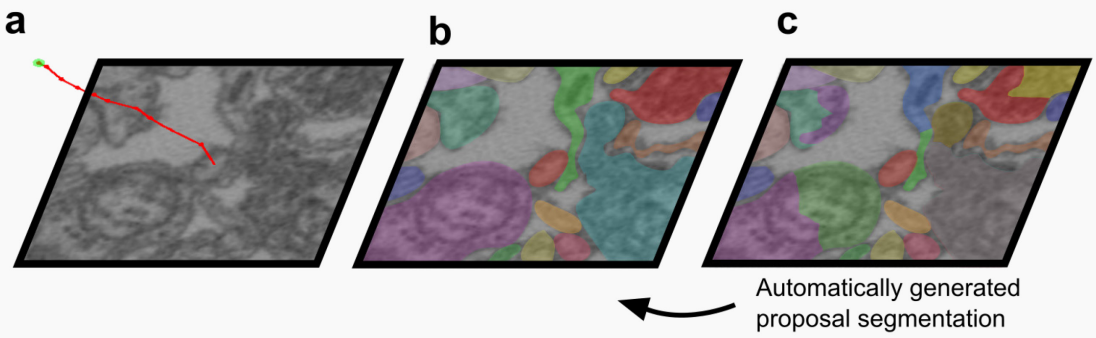

Figure 4 | Reconstruction strategies. (**a**) Skeletonization. A 3-dimensional graph is used to annotate tubular shaped neurites. (**b**) Segmentation. Dense, voxel-wise labeling of data. (**c**) Error-prone automatic segmentation can be used as a starting point for the creation of a final segmentation.

individual tiles determines how much time per SBEM acquisition is spent on them. At tile sizes in the range of 9 megapixels, typical in SBEM, the tile move overheads constitute the dominant time cost and become progressively less important at larger tile sizes (Figure 2).

In addition to this, a practical problem when acquiring volumes that have irregular 3-dimensional shapes, such as whole brains, is that the tile mosaic would have to be adapted exactly to that shape in order to not spend time scanning regions of the sample that are not of interest. The tile pattern would therefore have to change constantly while slicing through the sample. In SBEM, which cuts and images automatically, an adaptive tiling mechanism must therefore be implemented by which tile positions are either known ahead of time or are computed automatically during the acquisition. I describe the former type of solution in this thesis.

In summary, dynamically adapting the tile pattern to the sample geometry and reducing the number of motor moves between tiles are two approaches from which the speed of SBEM data acquisition can profit and that could bring the time required for the acquisition of a whole 6 dpf larval zebrafish brain down from circa 7 months to a more tractable 2 months (Figure 2, Figure 3).

Connectivity Reconstruction from Electron Microscopic Raw Data

Raw data acquisition is only the first step in a Volume Electron Microscopy project. To answer biological questions, neuronal morphology and connectivity must be extracted from the raw EM data. To this day, manual human input remains essential for this image analysis task and different software tools have been developed to support it (e.g. Knossos (Svara et al.), reviewed in (Helmstaedter and Mitra, 2012)).

Manual segmentation (Figure 4) aims at obtaining a fully 3-dimensional volumetric labeling. A human annotator views the raw EM data and outlines or paints structures of interest, which are usually individual neurites. By doing this for every plane, a 3-dimensional model of the volume of a complete cell is eventually obtained. This method is very time consuming, requiring on the order of 200 – 400 h for each mm of reconstructed neurite length (Helmstaedter et al., 2008).

The time required for such manual reconstructions can be reduced drastically by not labeling the complete volume, but by reconstructing neurites as spatial graphs, called skeletons, instead. This takes advantage of the fact that axons and dendrites are usually approximately tubular (Figure 4). This process is referred to as skeletonization. Fully manual skeletonization is approximately 50 times faster than fully manual segmentation (Helmstaedter et al., 2011) and has been applied to large-scale, dense reconstructions by parallelizing the task to hundreds of trained annotators (Helmstaedter et al., 2013). The drawback of skeletonization as compared to segmentation is that the data produced is not a fully 3-dimensional representation of the morphology of a cell. This issue can be overcome by combining skeletons with automatically generated segmentations (Helmstaedter et al., 2013). Automatically generated segmentations are currently of insufficient quality to reconstruct complete cells without further human input. Their generation typically relies on applying the watershed algorithm to a membrane probability map generated by Convolutional Neural Networks (CNNs) (see, for example, Berning et al. (2015)). The algorithm can be tuned so that it does not undersegment (merge two neighboring cells that should not be connected) and produces an oversegmentation (incorrectly splits one cell into many different compartments)

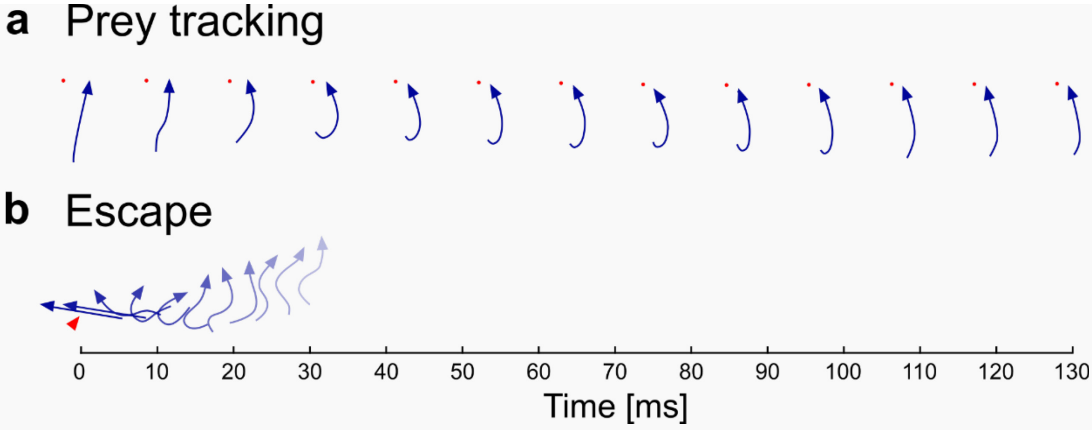

Figure 5 | Examples of different larval zebrafish motor programs. The arrow direction indicates the heading of the larva. (**a**) Prey tracking kinematics, re-drawn from McElligott and O'Malley (2005). Individual tail shapes are spaced by 10 ms. The red dot indicates the location of the prey, *Paramecium caudatum*. Note slow, low-amplitude bend of mostly the caudal tail. (**b**) Escape kinematics, re-drawn from Liu and Fetcho (1999). Individual tail shapes are spaced by 3 ms. Note rapid bending of complete tail into a C-shape. Red arrowhead indicates time point and location of mechanical stimulation with a water pulse.

instead. By collecting the individual oversegmented pieces of a cell using the manually generated skeletons, a complete, 3-dimensional reconstruction can be obtained.

Generation of Motor Outputs

Selecting and executing different motor programs is how the brain interacts with the outside world. Singing, dancing, speaking, walking, flying or swimming all have in common an orchestrated contraction of muscles, driven by neurons in the central nervous system. The neurons that directly cause muscle contractions by releasing acetylcholine at neuromuscular junctions are known as motoneurons (MNs) (Bear et al., 2015). MNs are organized in distinct pools that together innervate the same muscle. Within each pool, MNs vary in size, with larger MNs innervating more muscle fibers than smaller ones. In larval fish, the first MNs that develop are the primary MNs, of which there are 4 identifiable individuals per segment: the dorsal rostral primary (dRoP), the ventral RoP (vRoP), caudal primary (CaP) and middle primary (MiP) (Menelaou and McLean, 2012; Myers, 1985). They start developing very early and send their

axons out of the spinal cord within the first day of the embryo's life. They are followed during development by a much larger number of secondary MNs (SMNs), which are smaller and more ventral than the PMNs (Myers et al., 1986). Measurements of the total number of MNs per hemisegment in the larval zebrafish are quite divergent, ranging from 20 (Myers, 1985) to 63 (Asakawa et al., 2013).

Fish swim by rhythmically contracting their pectoral fin and axial (tail-lining) musculature, which is innervated by MNs in the spinal cord. The spinal MNs in turn receive inputs from spinal interneurons (Higashijima et al., 2004a; Kimura et al., 2006) as well as from reticulospinal (RS) projection neurons in the hindbrain (Fetcho, 1992; Wang and McLean, 2014) (see Grillner (2006) and Kiehn (2016) for review).

Locomotor repertoire of the larval zebrafish

Larval zebrafish produce a range of different swim patterns appropriate to the different situations they can find themselves in. This locomotor repertoire changes during development (Drapeau et al., 2002). The earliest tail movements, which larvae produce starting from the first day of their lives, are rhythmic coiling motions, where the fish repeatedly contract their tails into a corkscrew shape to break their egg shells and free themselves. From 2 dpf on, tactile stimulation elicits the C-start response, in which the entire tail is bent into a C-shape (Figure 5) (Budick and O'Malley, 2000) away from a noxious stimulus, followed by a high-frequency, high-amplitude swim, which begins at about 80 Hz and progressively decreases in frequency until it reaches 20 Hz, the tail beat frequency of routine exploratory swims (McLean et al., 2008). The pectoral fins are held close to the body and are not moved during this vigorous type of swim (McClenahan et al., 2012). On the other extreme of the spectrum, starting from 5 dpf, the fish produces visually guided, precisely tuned turns to orient itself towards prey, such as *Paramecium caudatum* (Figure 5). These individual tracking swim bouts have a duration of 100 – 200 ms with a tail beat frequency in the 20 – 30 Hz (Trivedi and Bollmann, 2013) range and involve alternating beats of the pectoral fins (McClenahan et al., 2012).

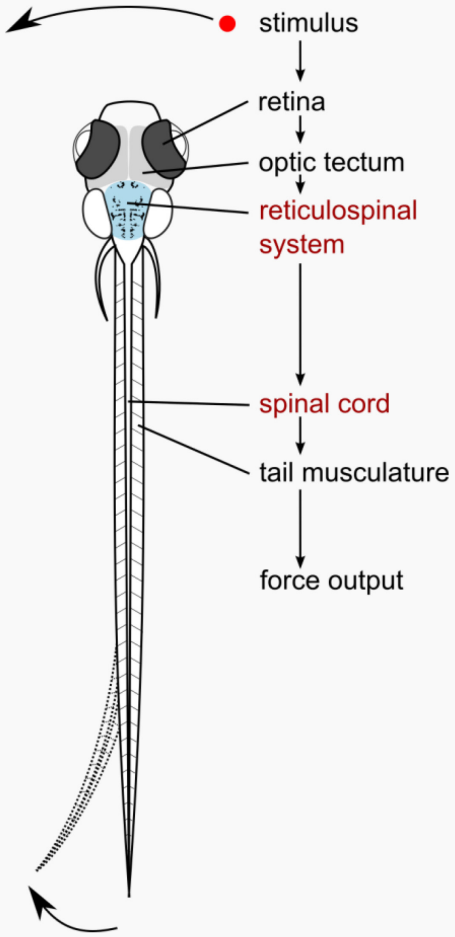

Figure 6 | Simple visuo-motor pathway for the larval zebrafish. A direct feed-forward connectivity from retina to optic tectum, from optic tectum to reticulospinal (RS) system and from RS system to spinal cord links the eyes to the muscles.

Initiation of Locomotion

How does the brain of the fish initiate these different motor programs? In higher vertebrates, corticospinal, rubrospinal and vestibulospinal projections, amongst others, descend into the spinal cord (Butler and Hodos, 2005). In fish, the situation is considerably less complex, since the only known glutamatergic projection from the brain into the spinal cord is the RS projection (Kimmel et al., 1982), suggesting a simple feed-forward network from eye to muscle (Figure 6). Therefore, all motor programs that are initiated by the brain must eventually be relayed by these 200 – 300 RS neurons in the hindbrain (Kimmel et al., 1982), which can be optically imaged in live fish and back-filled by tracer injections into the spinal cord (Orger et al., 2008). Yet, the code by which the brain, through the RS system, activates spinal networks is not known in detail. One example of a hindbrain RS cell with a dedicated behavioral role is the Mauthner cell, a cell reproducibly located exactly once on each side of the hindbrain and which is unusually large in size, with a length > 30 µm along its longer axis (measured in this work). The Mauthner cell specifically elicits short latency escape bends, but escapes can also be triggered without Mauthner activity, although non-Mauthner escape bends have a longer latency (Kohashi and Oda, 2008). All escapes, however, have in common the activation of a large fraction of RS cells (Gahtan et al., 2002). Weaker swims, such as those elicited by the opto-motor response (OMR), lead to lesser, but still widespread,

activation of the RS system. Of these, a small number are specific to the directionality of OMR-induced swims (Huang et al., 2013; Orger et al., 2008). These directional RS cells are individually named and identifiable across fish. For some of these, the MiV1, MiV2 and RoV3 cells, it could be shown that their degree of activation correlated with the expected degree of turning (Huang et al., 2013).

In addition to the motor programs commanded through the RS system, the fish has reflexes that do not require the brain to be involved in initiation. Mechanical stimulation of the tail activates Rohon-Beard (RB) cells, which activate commissurally projecting, excitatory Commissural Primary Ascending (CoPA) cells, which in turn activate MNs (Knogler and Drapeau, 2014), bypassing the brain in the initiation of a motor pattern.

Central Pattern Generators

Importantly, while neural circuits of the spinal cord are activated by commands sent to the tail from the brain, the spinal cord possesses the intrinsic ability to generate the rhythmic neural activity necessary for locomotion. This is vividly demonstrated by experiments in spinalized preparations, that is, experiments in which the spinal cord is isolated from the rest of the central nervous system. Even in the absence of actual muscle contractions, achieved for example by pharmacologically induced paralysis, fictive locomotion signals can be recorded directly from the motor nerves of spinalized preparations, mirroring the patterned activation generated by the spinal cord during locomotion of the intact animal. It can, for example, be elicited by bath-application of N-methyl-D-aspartate (NMDA) (McDearmid and Drapeau, 2006), by electrical stimulation (Gabriel et al., 2011), by optogenetic stimulation of specific spinal cell types (Ljunggren et al., 2014) and can also occur spontaneously (Masino and Fetcho, 2005). Fictive locomotion in spinalized preparations has been demonstrated in diverse species, including the lamprey (Wallen and Williams, 1984), tadpole (Li and Moult, 2012), fish (Masino and Fetcho, 2005) or cat (Kriellaars et al., 1994).

The neural network of the vertebrate spinal cord underlying its ability to independently generate motor patterns is called a Central Pattern Generator (CPG). CPGs exist not only in the spinal cord, and they do not only generate locomotor patterns. For example, the crustacean stomatogastric ganglion contains CPGs for the gastric and pyloric mills, which are responsible for grinding and mixing ingested food. Due to their easy experimental accessibility and the small number of neurons making up these circuits, these CPGs have been studied particularly well, with complete wiring diagrams having been obtained using electrophysiological techniques (reviewed in Marder and Bucher (2007)).

The focus of one half of this thesis is on the fish CPG for swimming. CPGs for swimming have been studied particularly well in lamprey (reviewed in Grillner (2006)) and tadpoles of *Xenopus laevis* (reviewed in Roberts et al. (2010)). In both cases, the rhythm they generate is characterized by motoneuron bursts alternating between the left and right sides of the tail, with a rostro-caudal

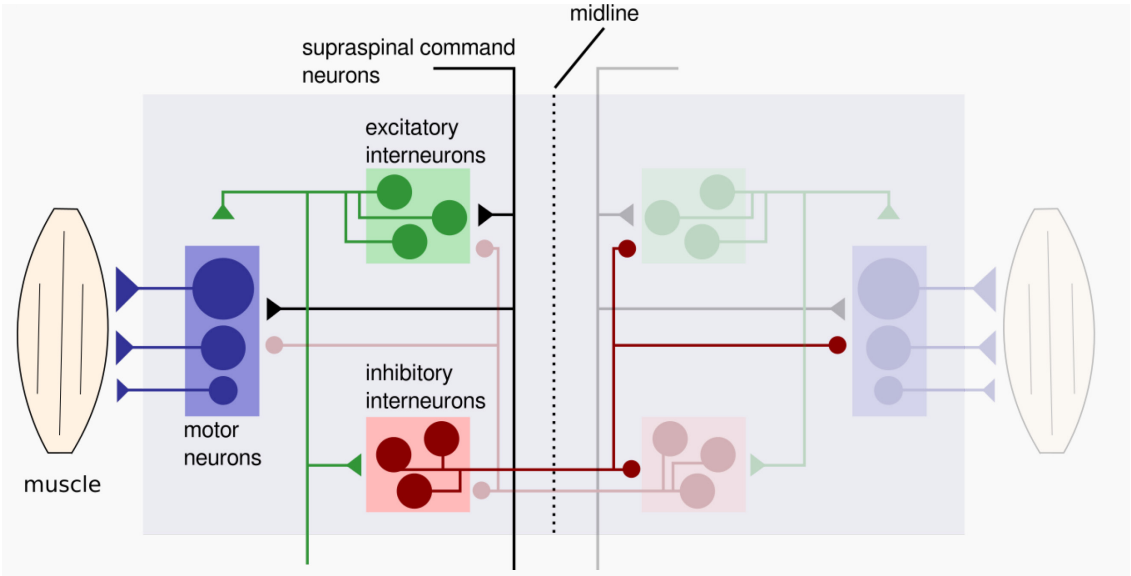

Figure 7 | Ground plan of a central pattern generator for swimming. Motor neurons are the output units, contacting muscles. They are driven rhythmically by excitatory interneurons. Commissural inhibitory interneurons ensure that the contralateral side is silent during ipsilateral contractions. Supraspinal commands activate the network. Adapted from Grillner (2006).

phase lag along the length of the tail. This causes a wave of bending to travel down the tail of the animal, propelling it through the water. Motoneurons in the spinal cord receive rhythmic in-phase excitatory drive and anti-phase inhibition (Kishore et al., 2014). Anti-phase inhibition to MNs was found to originate from a class of commissural inhibitory interneurons, called cIN in tadpoles (Dale, 1985) and CC in lamprey (Biro et al., 2006; Buchanan, 1982; Ohta et al., 1991). Based on morphology and transmitter phenotype, the Commissural Bifurcating Longitudinal (CoBL) interneurons were suggested to represent the zebrafish homolog of these cell types (Higashijima et al., 2004b). It was suggested that anti-phase inhibition could directly contribute to the generation of oscillatory activity through a rebound from inhibition mechanism, whereby inhibition of a neuron leads to the activation of low-voltage activated Ca^{2+} channels (Tegner et al., 1997), re-activating a neuron after a brief phase of inhibition. However, it was found that the transected spinal cord of the lamprey, in which all commissural axons are cut, can also generate rhythmic bursting that proceeds rostro-caudally but does not alternate between the two sides (Cangiano and Grillner, 2003). This finding shows that, while anti-phase inhibition is important to make sure that the tail does not contract synchronously on both sides, which would impair the animal's ability to move forward, it is the source of rhythmic in-phase excitation that most likely constitutes the key CPG component underlying the intrinsic burst generation capability of the spinal cord. The neuronal origin of this excitation was identified in lamprey as ipsilaterally projecting "glutamate interneurons" (Buchanan and Grillner, 1987), which were later named EIN (Buchanan et al., 1989). A homologous cell type was identified in the *Xenopus* tadpole and named dI (Dale and Roberts, 1985; Li et al., 2006). These ipsilateral excitatory interneurons have been shown to excite MNs, commissural inhibitory interneurons and other ipsilateral excitatory interneurons of the same type (reviewed in Grillner (2003, 2006)). In zebrafish, morphological characterizations of the interneurons of the spinal cord suggested that the Circumferential Descending (CiD) cells played the same functional role (Bernhardt et al., 1990). These cells, which were at first defined only morphologically through back-filling experiments, were later genetically characterized as V2a cells and were found to be excitatory (Higashijima et al.,

2004b), provide rhythmic drive to MNs (Kimura et al., 2006) and elicit fictive swimming upon optogenetic stimulation (Ljunggren et al., 2014).

Taken together, this data provides a simple ground plan for the spinal CPG: Ipsilaterally projecting excitatory interneurons drive their own side of the spinal cord rhythmically, including commissural inhibitory interneurons, which make sure that the other side remains inactive during the ipsilateral contraction (Figure 7).

This ground plan does however leave important questions open: When one side of the tail is active and contracts, how is that activity terminated? What causes the next cycle of activity to begin? One proposed burst-terminating mechanism is a cell-intrinsic mechanism known as a slow after-hyperpolarization (sAHP), first demonstrated in the lamprey spinal cord. The sAHP in lamprey interneurons is due to calcium-dependent potassium channels, which cause potassium efflux at high intracellular calcium levels (El Manira et al., 1994). Additionally, in lamprey, stretch receptor neurons were found that detect the stretch caused by the bending of the tail during swimming. These stretch receptors come in an inhibitory and excitatory type (SR-I and SR-E). The former provides recurrent inhibition to the ipsilateral side that contributes to burst termination; the latter provides excitation to the contralateral side contributing to the initiation of the counterbend (Di Prisco et al., 1990). However, as the generation of fictive locomotion in immobilized preparations shows, stretch receptors are not essential for the generation of the locomotor pattern. Additionally, no such receptors have yet been found in tadpoles and fish. In tadpoles, a type of inhibitory interneuron with ascending axons, called aIN, which is likely homologous to the zebrafish circumferential ascending (CiA) interneuron type, was shown to provide early-cycle inhibition to dI interneurons (Li et al., 2004). Since the aINs are rhythmically active in-phase with motor bursts, these neurons might be part of a negative feedback loop contributing to burst termination. Cell-intrinsic burst generation and termination has also been described in MNs themselves, with some MNs generating rhythmic bursts in response to tonic depolarization (Menelaou and McLean, 2012). Through electrical coupling with their presynaptic excitatory

interneurons, they may thus play a more active role in the rhythmicity of the network than previously thought (Song et al., 2016).

The circuits and cell-intrinsic properties introduced up to now can explain the generation of ongoing, alternating motor bursts in the presence of tonic excitation, but the other, very important property of the CPG for swimming, the rostro-caudal phase lag, has not yet been touched upon. One simple way to achieve a rostro-caudal delay would be to directly use axons as delay lines, as, for example, suggested for coincidence detection in the auditory system (Jeffress, 1948; Joris et al., 1998). This would require 1) the axonal conduction velocity to be the same as the speed of rostro-caudal wave propagation and 2) a rostrally restricted population of excitatory neurons to send axons caudally. Both conditions appear not to be met in fish. During the slowest swims, the rostro-caudal delay was found to be on the order of 0.06 m / s (McLean et al., 2008), an order of magnitude smaller than the 0.6 m / s expected for a very small unmyelinated axon with a diameter of 100 nm (Waxman and Bennett, 1972). Ipsilaterally projecting, descending excitatory interneurons appear to be rostro-caudally scattered in fish (Kimura et al., 2006), tadpoles (Li et al., 2001) and lamprey (Buchanan et al., 1989). Thus, the explanation for the rostro-caudal phase lag must be more subtle. Modeling studies based on anatomical and physiological measurements have suggested possible mechanisms: One is that MNs exhibit a rostro-caudal gradient in excitability, so that the rostro-caudal activation order of MNs along the tail depends on how long it takes a MN to reach its respective spike threshold (Tunstall and Sillar, 1993). A different but related idea is that some of the primarily descending excitatory interneurons also have ascending arbors, so that the distribution of synaptic outputs from these neurons is not equal over the length of the spinal cord, but is high rostrally and becomes progressively lower caudally. The net effect would be similar to that of a rostro-caudal gradient in MN excitability (Wolf et al., 2009).

Motor Unit Recruitment

To support the generation of a diverse set of motor patterns of different strength, CPGs must have different modes or degrees of activation. This is, in general, an active area of research. The physiological behavior of motor units

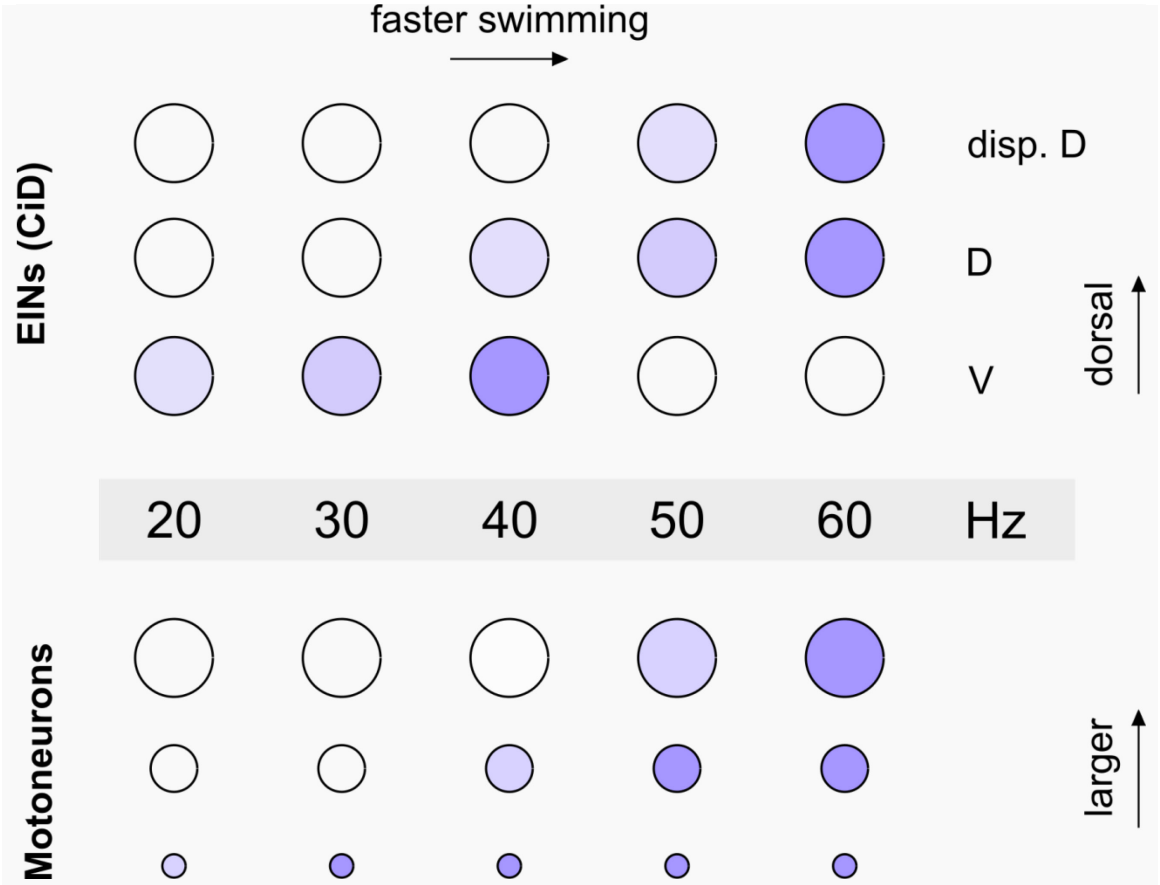

Figure 8 | Orderly recruitment of motoneurons from small to large and topographic recruitment of excitatory interneurons from ventral to dorsal. Filled circles represent active cells. Saturation of fill color represents degree of activation. In excitatory interneurons (CiDs), activity switches from ventral to dorsal as swims go from slow to fast. In motoneurons, activity increases within the pool, with larger motoneurons being added during faster swims. Larger motoneurons also tend to be located more dorsally in larval zebrafish. CiD: Circumferential descending interneurons. After (McLean et al., 2007; McLean et al., 2008).

during motor outputs of different strengths has been well described. A motor unit is defined as a MN and all the muscle fibers it contacts (Liddell and Sherrington, 1925). Motor units are recruited in an orderly fashion: only small MNs that contact a small number of muscle fibers are activated when weak contractions are performed. As muscle contractions become stronger, additional MNs are recruited into the active pool, progressing from smaller to larger MNs, which contact more muscle fibers (Figure 8).

This finding was first reported by Elwood Henneman for the MNs of the cat spinal cord (Henneman, 1957). He later coined the term “size principle” (Henneman et al., 1965), which, as “Henneman’s size principle”, has since become a common term describing this physiological phenomenon, which was found to generally hold across many different species (reviewed in (Cope and Pinter, 1995; Mendell, 2005)), including fish (Gabriel et al., 2011; McLean et al., 2007). The purpose of this recruitment pattern may be to allow fine-tuning of force output in proportion to the current muscle force generated (Henneman et al., 1965).

Henneman also proposed a mechanism for the establishment of the recruitment order, in which the presynaptic system activating MNs would connect to MNs of all sizes non-specifically. The specific recruitment sequence would then emerge from differences in input resistance due to the differences in MN sizes. By $\Delta U = R_{in} \cdot \Delta I$ (ΔU: change in membrane potential, R_{in}: input resistance, ΔI: change in membrane current due to synaptic activity), the larger MNs with lower input resistance would require more synaptic input current to reach the same voltage threshold and to be recruited compared to a smaller MN (Figure 9a). Early critics of this hypothesis included Burke (1968) and Zucker (1973), who argued that a larger MN would also receive proportionally more synapses and thus proportionally more synaptic current, offsetting the effect of input resistance on the recruitment order. Additionally, physiological evidence showing that the recruitment order could be reversed under specific conditions (Kanda et al., 1977) called into question at least the universal applicability of Henneman’s proposed mechanism. The precise mechanism by which the orderly recruitment of MNs is established remains, to this day, controversial. In any case, the mechanism must depend on the pattern of activity in the presynaptic network activating the MNs during different strengths of locomotion. This pattern has recently been elucidated for the ipsilateral excitatory interneuron network in larval and juvenile fish (McLean et al., 2008). In larvae, CiDs (also known as V2a) are recruited above a minimal swim frequency which correlates with the cell’s dorso-ventral soma position, with more dorsal cells exclusively recruited during fast swims. During the slowest

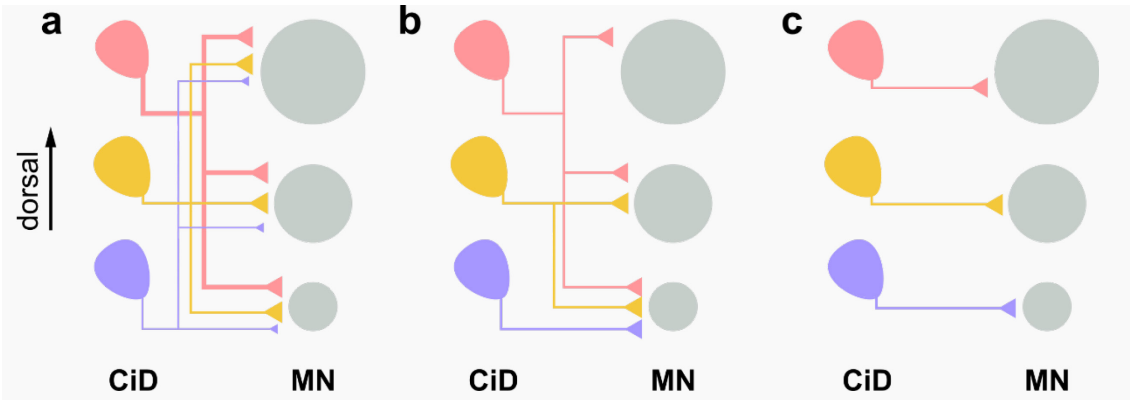

Figure 9 | Hypothetical wiring from excitatory interneurons (CiDs) to motoneurons (MNs) potentially explaining the orderly recruitment of MNs, given the recruitment patterns in CiDs. (**a**) All-to-all wiring, as originally suggested by Henneman et al. (1965). The recruitment order emerges from differences in biophysical properties on MNs. Since ventral CiDs are deactivated during the strongest swims, a difference in synaptic efficacy (synapse size) is additionally postulated here to make up for the loss of synaptic current from these cells. (**b**) Selection of subsets of MNs by specific CiDs through specific wiring (Menelaou et al., 2014). (**c**) Labeled-line subtype-to-subtype wiring postulated for adult fish (Ampatzis et al., 2014). Additional compensating mechanisms, or a lower wiring precision than schematically shown here, would have to be assumed to explain lack of derecruitment of small MNs during strongest swims.

swims, a different type of excitatory spinal interneuron, called MCoD, was also activated. Importantly, cells recruited for slow swims, up to a frequency of ca. 40 Hz, which included the MCoDs and the ventral CiDs, were silenced at higher frequencies. At those higher frequencies, a different subset of the CiDs, the dorsal CiDs and dorsally displaced CiDs were active instead (Figure 8). In juveniles, the silencing of CiDs interneurons at higher frequencies was not observed. While, as in the larval fish, CiDs had different minimal recruitment frequencies, they were not topographically organized in the spinal cord (Ampatzis et al., 2014).

The physiology of the CiDs in larval zebrafish suggested a wiring pattern from CiDs to MNs in which the specific recruitment sequence of MNs is encoded directly in the pattern of connections. That is, dorsal, high-frequency

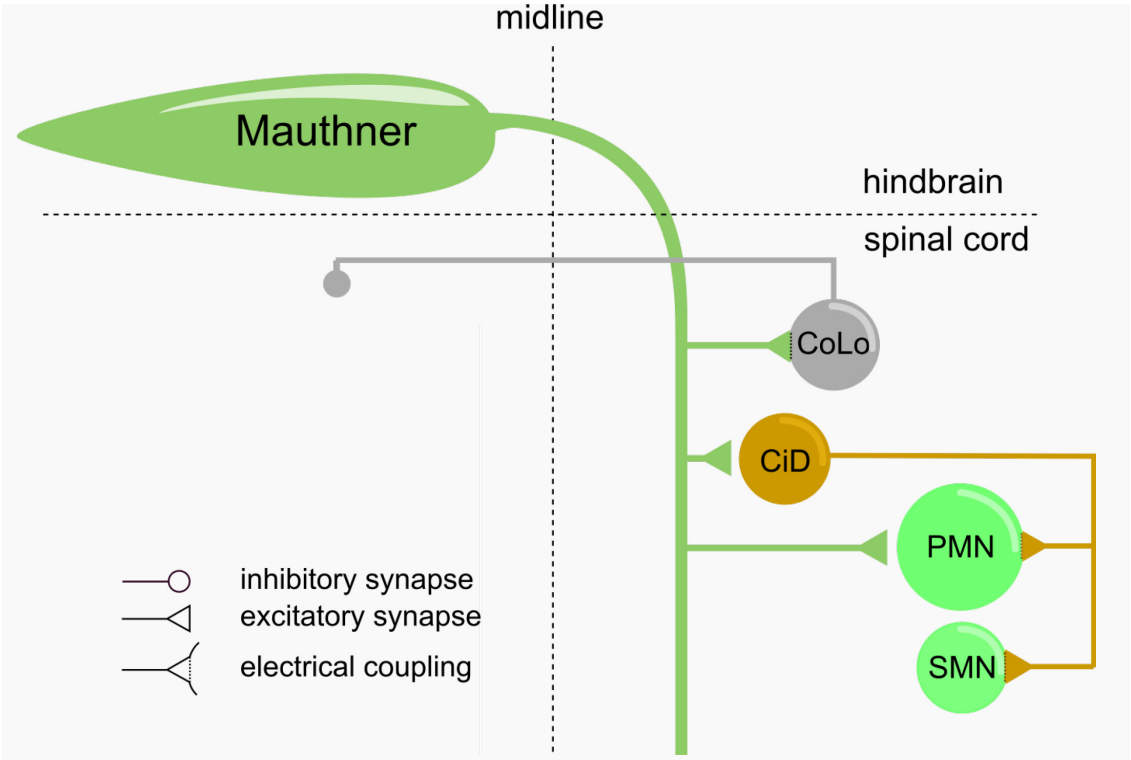

Figure 10 | Schematic of previously described connections in the goldfish escape network. Zebrafish interneuron nomenclature is used. The Mauthner cell directly activates commissural inhibitory interneurons that prevent a simultaneous contralateral bend (commissural local neurons, CoLos), primary motoneurons (PMNs) and ipsilaterally descending excitatory interneurons (circumferential descending, CiD), which in turn activate both PMNs and secondary motoneurons (SMN). Adapted from Fetcho and Faber (1988).

interneurons would make connections to the entire MN pool, since the complete set of MNs, from small to large, should be recruited when they are active. In contrast, the more ventral, low-frequency interneurons would contact exclusively small MNs (Menelaou et al., 2014) (Figure 9b). While this type of wiring would explain the physiological findings, it is not the only mechanism by which orderly recruitment can be achieved that is consistent with the physiology of the CiDs. With unspecific, all-to-all wiring, similar to that originally proposed by Henneman, orderly recruitment would still emerge if the more dorsal CiDs that are active during faster swims compensate for the loss of the more ventral ones by making stronger synapses onto the MN pool (Figure 9a).

In contrast to the findings in larval fish, paired recordings in juvenile fish suggested a different picture. Excitatory interneurons and MNs were categorized into three different physiological classes, based on their minimal recruitment frequency: Weak, intermediate and fast. Interneurons were likely to contact MNs of the same class, but rarely contacted MNs of a different class (Ampatzis et al., 2014) (Figure 9c).

To summarize, the mechanism by which the orderly recruitment sequence of MNs is achieved in larval zebrafish during stimulation from the rhythm generating CiD / V2a network is currently unknown. One explanation could lie in biophysical differences between MNs of different sizes, with unspecific connectivity (Figure 9a). Alternatively, CiDs may transmit their activity to just the subset of MNs that should be recruited through specific wiring (Figure 9b). Some degree of specific wiring has been shown in juvenile fish (Figure 9c), but that wiring pattern can't explain the situation in larvae, due to differences in the recruitment / derecruitment of CiDs.

A Hard-Wired Spinal Network for Escape

Independent of the network generating the sustained swimming rhythms, the spinal cord of fishes contains an escape network that generates low-latency C-shaped tail bends (C-bends). The initial bend away from the stimulus traps a bolus of water, which is forcefully accelerated backwards by the subsequent counter-bend (Gazzola et al., 2012), propelling the fish forward and away from a dangerous situation. C-bends elicited by stimulation of the otic vesicle activate the Mauthner cell (Kohashi and Oda, 2008), which has a large, myelinated commissural axon. The spinal targets of the Mauthner axon have been investigated particularly in the goldfish, *Carassius auratus*. Spikes in the Mauthner cell were shown to elicit a short-latency, electrical EPSP and a longer latency, chemical EPSP in primary MNs. Electrical connections are also made with the axon of a commissural inhibitory cell (Fetcho and Faber, 1988). Additionally, the Mauthner cell indirectly activates both primary motoneurons (PMNs) and secondary motoneurons (SMNs) through an ipsilateral, excitatory, descending cell type called DI in goldfish, which likely corresponds to the zebrafish CiD (Fetcho, 1991, 1992). A summary of the known connections of the Mauthner axon is given in Figure 10.

Larval Zebrafish as a Model Organism for the Study of Motor Pattern Generation

Larval zebrafish have recently gained popularity as a model organism for the study of motor pattern generation, a consequence of the ease of optical imaging through their transparent skin, the relative simplicity of the system and availability of genetic tools (see Gahtan and Baier (2004) for review).

Importantly, the inventory of different interneuron and motoneuron types, along with their transmitter phenotype, has been characterized using stochastic labeling approaches (Bernhardt et al., 1990; Hale et al., 2001; Higashijima et al., 2004b). Calcium imaging and patch clamp recordings have been used in paralyzed preparations producing fictive swimming to elucidate the recruitment orders for MNs and CiDs mentioned above (McLean et al., 2007; McLean et al., 2008). Optogenetic stimulation of specific, genetically defined cell types has led to the discovery of a role of cerebrospinal fluid contacting Kolmer-Agduhr cells in the initiation of slow, exploratory-like swims (Wyart et al., 2009).

As detailed above, sample size remains an important obstacle in volume electron microscopy studies. Yet, with a diameter of 50 – 60 µm and a segment length of ca. 70 µm, samples of the larval zebrafish spinal cord containing a small number of complete segments are well accessible and experimentally tractable.

Objectives

In the spinal cord, a detailed map of the connectivity between spinal interneurons and motoneurons would be highly instructive to mechanistically understand how motoneurons are recruited in an orderly fashion. Therefore, the aim of this thesis was to use Serial Block-Face Electron Microscopy (SBEM) circuit reconstructions to

1. characterize a complete motoneuron pool in an unbiased fashion, to reveal whether motoneurons are distributed on a graded scale in size and dorso-ventral position or whether they can be divided into subtypes.
2. identify the presynaptic partners of these motoneurons.
3. obtain a detailed map of the connectivity between CiDs and motoneurons, to answer the question of whether the CiDs contact motoneurons of different size differently, depending on the dorso-ventral position of the CiDs.

Currently, SBEM datasets are relatively small compared to the size of a complete brain and even small brains such as that of the larval zebrafish would take on the order of half a year to acquire. The aims of the second part of this thesis were

1. to implement line-scanning of individual SBEM tiles to increase their size, allowing most motor moves in a multi-tile mosaic to be avoided.
2. to dynamically match the layout of the tile mosaic to the irregular shape of a brain, to avoid scanning surrounding plastic.
3. to establish a conductive embedding protocol, allowing a whole brain to be imaged without charging artifacts in high vacuum.
4. to correlate the electron microscopy data to 2-photon calcium imaging data of cells that respond to opto-kinetic stimulation, obtained through a collaboration with Dr. Fumi Kubo in the department of Prof. Dr. Herwig Baier (MPI of Neurobiology, Martinsried).

Methods

Fish Maintenance

Mating pairs of adult zebrafish (*Danio rerio*) were set up in the evening and freshly laid eggs were collected the next morning. Eggs were maintained at 28°C in embryo medium under a 14 h light / 10 h dark cycle, as described previously (Westerfield, 2007). Starting from 5 days post fertilization, larvae were fed with *Paramecium caudatum*. All experiments were in accordance with German animal welfare law. Only larvae that successfully captured prey were used for subsequent experiments, to ensure good health.

Fish Lines

The spinal cord dataset was obtained from a *nacre*$^{-/-}$ mutant fish (Lister et al., 1999). The brain dataset was obtained from an *elavl3:GCaMP5G* transgenic fish (Ahrens et al., 2013; Akerboom et al., 2012), which expresses the Calcium sensor protein GCaMP5G pan-neuronally.

Tissue Sample Preparation for Electron Microscopy

Spinal Cord

At 6 days post fertilization, larvae were anaesthetized by placing them in embryo medium (Westerfield, 2007) containing 0.016 % MS-222 (Tricaine methanesulfonate, Sigma-Aldrich). A single larva was carefully placed in the center of a silicone (Sylgard® 184, Dow Corning) coated dish. All subsequent steps were performed under observation through a microscope (MZ 16-F, Leica) for fine control. Excess water droplets were removed using a fine paper towel (Kimwipes, Kimberley-Clark). The larva was then embedded in 4% low-melting point agarose (Roth GmbH) dissolved in embryo medium containing 0.016% MS-222, heated to just above melting temperature, and covered in the anesthetic solution after solidification of the agar. The tail of the larva was freed by removing surrounding agar and cut off at the level of the 15th myotome using fine scissors (Fine Science Tools GmbH) (Figure 11).

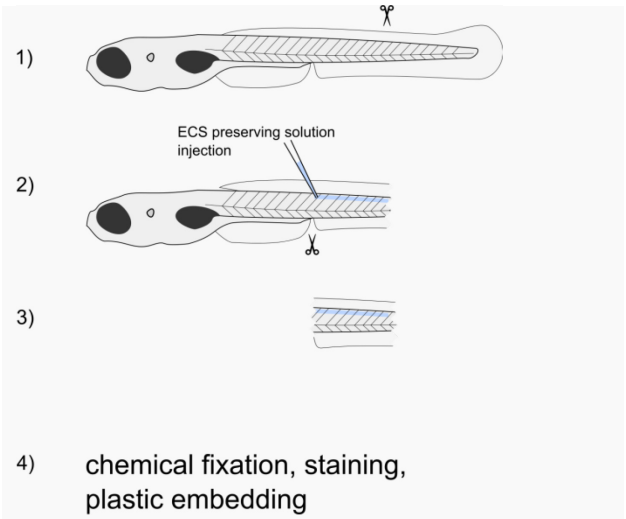

Figure 11 | Spinal cord preparation protocol. The tail is cut caudally (1) and a modified Ringer's solution containing Cesium Gluconate is injected into the spinal cord and allowed to flow through the tail (2). The perfused piece of the tail is cut off (3) and processed as usual for EM (4).

A glass pipette was pulled from borosilicate glass (outer diameter: 2 mm, inner diameter: 1 mm, Hilgenberg) using a pipette puller (Narishige). The pipette puller parameters were empirically optimized to yield pipette tips of a diameter of ca. 5 µm. The pipette was filled with a solution preserving the extracellular space of neural tissue during subsequent fixation and staining, which was developed based on a previously published protocol (Cragg, 1979, 1980). The solution was a freshly carbogen-bubbled modified teleost carbonate-buffered artificial cerebro-spinal fluid (ACSF) (Mathieson and Maler, 1988), for which half the molar proportion of NaCl (65 mM) was replaced with cell-impermeable Cesium Gluconate. This solution was injected into the spinal cord, 5 segments rostral from the cut location using a PicoSpritzer III (Parker Hannifin Corp.) at slight positive pressure and allowed to flow through the spinal cord and out through the cut for 2 minutes.

The perfused part of the tail was then cut off and chemically fixed, stained and embedded, based on the protocol described in (Briggman et al., 2011). Fixation was performed by immersing the tail sample in 0.1 M Cacodylate Buffer (CB) (made from Sodium Cacodylate (Sigma-Aldrich) with pH set to 7.4 with hydrochloric acid) containing 2% Glutaraldehyde (Sigma-Aldrich) and 4% sucrose (Sigma-Aldrich) for 3 hours. After rinsing with 4% Sucrose in 0.1 M CB, the rOTO (reduced Osmium, Thiocarbohydrazide, Osmium) stain was performed (Karnovsky, 1971; Seligman et al., 1966). All staining solutions in the following steps were freshly prepared. The reduced osmium stain was

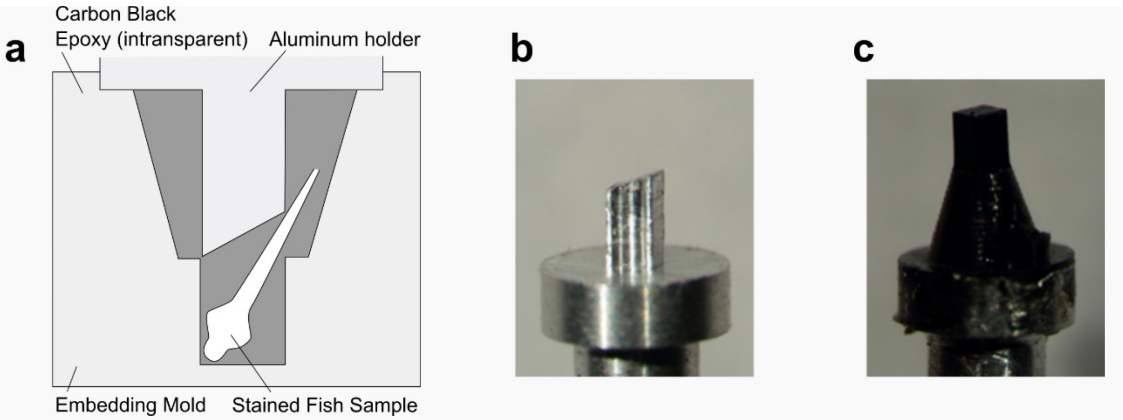

Figure 12 | Whole-fish embedding mold and holder. (**a**) Sketch of embedding mold filled with carbon black epoxy and fish sample, in the orientation and configuration in which polymerization is performed, rotated by 180° with respect to (b) and (c). The aluminum holder is inserted from the top. (**b**) Aluminum holder without sample. (**c**) Holder with sample.

performed using 2% osmium tetroxide (Electron Microscopy Sciences) in 0.15 M CB with 2.5% potassium hexacyanoferrate (Sigma-Aldrich) for 1 hour at room temperature. After rinsing with 4% sucrose in 0.1 M CB, Thiocarbohydrazide (TCH) (Sigma-Aldrich) amplification was performed using 1% TCH in water for 1 hour at 58°C.

After rinsing with water, Osmium staining was performed with 2% osmium tetroxide in water for 1 hour at room temperature. After rinsing with water, the sample was stained with 2% Uranyl Acetate (Sigma-Aldrich) for 2 hours at 52°C in darkness (Hayat, 1989). After rinsing with water, the sample was stained with lead aspartate (Walton, 1979) at 53°C at a pH of 5.0 for 2 hours. After rinsing with water, the sample was dehydrated using an ethanol series of 10 minutes in 70%, 90% and 100% ethanol (Electron Microscopy Sciences). The last step in 100% ethanol was repeated once for 30 minutes and ethanol was then replaced by propylene oxide (Sigma-Aldrich). To embed the sample, an Epon 812 replacement mixture was freshly made from dodecenylsuccinic anhydride (DDSA) (Serva), nadic methyl anhydride (NMA) (Serva) and glycid ether 100 (Serva) (proportions: 4.5 : 6 : 10), to which 0.3 % Benzyldimethylamine (BDMA) (Serva) was added as an accelerator. The sample was incubated for 5 hours on a rotator in a 1 : 1 mixture of the Epon

812 replacement with propylene oxide and was then transferred to the pure Epon 812 replacement mixture, and placed into embedding molds (Electron Microscopy Services). The plastic was allowed to polymerize for 48 hours at 60°C.

After complete hardening, the sample was trimmed into a rectangular frustum geometry, exposing the tail and spinal cord in transversal section at its top. The surface was then smoothed by cutting a series of 80 nm ultrathin sections on an EM UC7 (Leica) ultramicrotome using an ultra 45° boat knife (Diatome).

Brain

A 5 dpf fish was anesthetized in the freshly carbogen-bubbled extracellular space preserving ACSF solution described above, containing 0.016% MS-222. Instead of agar embedding, it was immobilized in a silicone coated dish by placing two short (ca. 500 µm) pieces of Tungsten wire (Advent Research Material) through its notochord and fixating the fish by these wires using insect pins, as described in (Masino and Fetcho, 2005). To additionally stabilize the head, another piece of fine tungsten wire was pushed through the lower jaw into the silicone base of the dish. A tungsten wire with a very sharp tip, obtained by electrochemical etching at 10 V in 1 M potassium hydroxide solution was used to make a small incision into the skin at the caudal end of the hindbrain. Through this incision, the tungsten wire tip was inserted under the skin and carefully pulled upward and rostrally, to pull away the skin without touching the brain. This allowed most of the skin to be pulled away cleanly. Any remaining pieces of skin were removed with fine forceps (Fine Science Tools). The whole fish was then fixed and stained as described above, up to the ethanol series dehydration, but not embedded in standard, clear plastic.

For conductive embedding, 2.5% Carbon Black (Ketjen Black® EC-600JD, Akzo-Nobel) Epon replacement was prepared by adding 2.5% Carbon Black, prepared from pestled pellets, to the Epon replacement mixture described above, which was then mixed in 1 : 1 proportion with propylene oxide. To obtain good dispersion of the carbon black, the mixture was sonicated for 3 hours at room temperature in a well-sealed container. To remove the propylene oxide, the mixture was spread out in a glass petri dish and placed in a vacuum

desiccator for 2 hours. The sample was then embedded in this mixture using a specially designed embedding mold and holder that allowed for reproducible positioning of the fish relative to the holder (Figure 12). The fish was positioned in the holder so that it would be cut in a plane rotated by 35° in yaw from the transversal plane.

Serial Block-Face Electron Microscopy Stack Acquisition

Spinal Cord

SBEM data was acquired on an Ultra Plus scanning electron microscope (Zeiss) equipped with a custom-built SBEM microtome and an additional external scan generator (Fibics Inc.). A custom acquisition control script implemented as an ImageJ (Schneider et al., 2012) plugin controlled the hardware through the application programming interfaces (APIs) of SmartSEM (Zeiss) and ATLAS (Fibics Inc.). The stack consisted of a 9874 single-tile slices with 8000 x 8000 pixels per tile at an axial resolution of 9 x 9 nm. The cutting thickness was 21 nm. The beam voltage was 2.1 kV at a current of 1 nA and dwell time of 200 ns, corresponding to an electron dose of 15.4 e^- / nm^2. The total stack acquisition time was 12 days.

Brain

The brain SBEM data was acquired on the same setup as the spinal cord data, after significant modifications. In particular, the microtome was fitted with additional stage-movement piezos (PICMA® stack multilayer piezo actuators, Physik Instrumente GmbH) allowing a smooth axial movement of the sample. The acquisition software was re-implemented in Java™ (Oracle Corp.), based on the ImageJ plugin implementation used for the spinal cord, to allow more convenient implementation of the additional features required for this acquisition. Prior to setting up the SBEM stack, the final sample was sent for X-Ray microCT scanning at a resolution of 4 x 4 x 4 µm (Scanco Medical). That data was used to manually define the region of interest (ROI), consisting of the entire brain, but not the rest of the head, for targeted SBEM acquisition. Custom Python code was used to generate text files containing sequences of microtome motor coordinates for individual SBEM tiles for every slice from the 3-dimensional ROI.

To operate the microscope in line-scanning mode, the voltage input to the y-axis beam scanner was disconnected. The ATLAS software generates a beam-unblank transistor-transistor logic (TTL) signal when image acquisition begins, and that unblank signal was used to trigger a function generator (AWG33522, Agilent) driving the stage-movement piezos, onto which a waveform moving the sample under the beam in the direction formerly covered by the y-axis scanner was pre-loaded. To compensate for piezo-scan nonlinearity due to creep and hysteresis, the piezo voltage was transformed using a dynamic model developed by W. Denk, which was implemented by me as a C library that could be used from the main acquisition software.

To avoid a loss of sensitivity of the back-scattered electron detector (Opto Diode Corp.) due to hydrocarbon coating during SBEM acquisition, the microscope was equipped with a GV10x down-stream asher (IBSS Group Inc.). Every 2-3 days, stack acquisition was interrupted to run the down-stream asher at a power of 70 W for 1 hour. The sample was allowed to settle for 1-2 hours after ashing. Stack acquisition was then resumed after manual refocusing.

Imaging was performed at an axial resolution of 14 x 14 nm at 2 kV beam energy, 2 nA current and 5 MHz, yielding an electron dose of 12 e^- / nm^2. The cutting thickness was 25 nm.

The total acquisition time, excluding interruptions due to technical issues with the microscope requiring servicing by the vendor, was 53 days.

EM Raw Data Registration

Spinal Cord

The single-tile image stack was aligned using the Linear Stack Alignment with SIFT ImageJ plugin (Saalfeld and Tomancak, 2008), using standard parameters except for selecting “Translation” as expected transformation, disabling interpolation and setting the maximal alignment error to 1024 pixels.

Brain

The multi-tile, line-scanned stack was aligned using Karsh’s aligner (Scheffer et al., 2013). To allow for a more powerful correction of the non-linearities introduced by piezo-based line-scanning, each one of the line-scanned tiles

was cut along the y-axis into pieces of 500 pixels y-length with 30 pixels overlap between the pieces, producing 8463946 individual input tiles for the Karsh pipeline. Prior to running the aligner on the cut tile pieces, the center regions of all the original tiles, sized 3000 pixels in width and 5000 px in height, were pre-aligned to obtain more precise information about the relative positioning of the tile pieces. The full alignment run was performed on a Grid Engine (Univa) cluster consisting of 18 nodes equipped with 20 1.6 GHz Xeon® E5-2660 v3 (Intel) CPU cores, for a total of 380 CPUs and took less than two weeks. The Karsh alignment pipeline only outputs the parameters of the affine transformations to be applied to each tile. Subsequent rendering of montaged slices and generation of cubed data compatible with Knossos was performed using custom Python code developed from code originally written by J. Kornfeld.

Serial Block-Face Electron Microscopy Data Annotation

Spinal Cord Anatomical Measurements

The average area, maximal dorso-ventral and maximal left-right extent of transversal spinal cord sections was measured from 4 sections, selected to span the entire length of the stack, by manual annotation in ImageJ (Schneider et al., 2012). Segment lengths were measured by using the ventral root (VR) locations as segment boundaries. For the ventral roots that were split into two bundles exiting separately, the rostro-caudal mid-point between the two bundles was used. The segment lengths were obtained by taking the average of the rostro-caudal distance between VR locations on both sides.

Neuron Tracing

Neuron reconstructions were performed by skeletonization using Knossos (Svara et al.) by a team of student annotators trained for the task. The annotator team was hired and trained by J. Kornfeld and F. Svara and was composed mostly, but not exclusively, of science students of the University of Heidelberg. Training consisted of a theoretical introduction into electron microscopic ultrastructure interpretation and practical neuron annotation exercises and training with Knossos. The ability of prospective students was evaluated in a short interview based on the performance on a tracing test. Students could work remotely. Raw SBEM data was provided either on external

hard-drives or was streamed over the internet. Tasks were distributed and work results were collected over the internet using a custom task management system, called “heidelbrain”, that was developed in Python and integrated into the Knossos user interface. The annotators were instructed to place a node approximately every 100 – 150 nm, to make sure that nodes and the connections between nodes never cross the boundary of a neurite and to value accuracy over speed. The mean neurite reconstruction speed for the spinal cord dataset was 170.4 µm / h.

A part of the tracings of Circumferential Descending (CiD) interneurons was out-sourced to Ariadne Service GmbH, a company specializing in volume EM data annotation. In that case, the company ensured the training of the annotators, but all task-specific instructions and performance assessments were performed by me. In that case, the annotators used the PyKnossos (Wanner) software, similar to Knossos, developed by Ariadne Service GmbH.

In order to reduce tracing mistakes, every tracing was performed independently by 3 different annotators. This required a consensus generation mechanism to obtain the final annotation. Two different approaches were used. In the simpler and less time-consuming approach, a fourth annotator was asked to carefully inspect every location at which the 3 tracings did not match. For every location at which only one tracer had continued tracing a correct continuation of the cell, the fourth annotator was instructed to follow and verify that complete branch. The second approached allowed consensus generation with minimal knowledge about the input tracings from the 3 original annotators, to reduce any potential bias originating from that knowledge. In that approach, termed “focused reannotation”, seed points were automatically generated for every location at which the tracings did not match. The seed point consisted of a short (500 nm) skeleton segment labeling a neurite where at least 2 original tracers agreed, and another segment labeling a potential continuation from that neurite that had only been found by one tracer. A fourth tracer was asked to inspect that seed and connect the two segments if they believed the continuation to be correct and leave them disconnected if they did not think so. In the former case, the fourth tracer also continued tracing into the rest of the continuation from the seed segment. Since this process potentially generated

new discrepancies during reannotation, it was performed iteratively until no discrepancies remained.

Synapse Detection, Annotation and Size Measurement

Several ultrastructural features were used to identify synapses: 1) Synaptic vesicles in the presynaptic partner, 2) an electron dense presynaptic active zone at the presynaptic membrane lining the synaptic cleft, 3) a postsynaptic density lining the postsynaptic membrane, 4) parallel pre- and postsynaptic membranes that were spaced by a typical synaptic cleft distance of ≈ 30 nm. Postsynaptic densities were often faint and could not always be clearly detected.

To comprehensively detect synapses between different sets of tracings, such as tracings for spinal interneurons and tracings for motoneurons, all proximity locations, where tracings of either type came within less than 1 µm of each other, were automatically identified using custom Python code. Annotators were instructed to inspect each of these proximity locations and decide whether a synaptic contact was present. Synaptic contacts were then annotated by drawing a line along the synaptic cleft in the orthogonal data (re-)slice view in which it appeared largest to obtain a measure of the contact size and unambiguously label the contact location. All proximity locations were inspected independently by two different annotators. All locations that were identified as synaptic by both were considered true synapses. Locations that had been labeled synaptic by only one of the two were inspected by a third expert (F. Svara), who made the final decision in these cases.

Since synaptic contact morphologies were often complex and not well approximated by a circle, synaptic contact sizes were measured by filling the complete synaptic cleft volume in Knossos with a 3-dimensional mask. To obtain a contact area measure from the painted clefts, the contact area described by the mask was approximated by a set of splines, fit individually to every slice of the mask volume.

General Data Presentation and Processing

Unless otherwise stated, all automated data analysis was performed using custom Python code, relying on the SciPy, NumPy (van der Walt et al., 2011)

and NetworkX (Hagberg et al.) modules. Two-dimensional plotting was performed using the matplotlib (Hunter, 2007) python module. Three-dimensional plots were made using Mayavi (Ramachandran and Varoquaux, 2011). Figures were compiled as vector graphics using Inkscape (www.inkscape.org, accessed August 2016). Raster graphics editing was performed using GIMP (www.gimp.org, accessed August 2016).

Spinal Cord Network Reconstruction

Classification of Interneuron Types

Interneuron types were classified using the trajectories of the axons and dendrites, based on the descriptions in Hale et al. (2001). Cells with an ipsilaterally descending axon, optionally with an ascending branch, were CiDs. Cells with an ipsilaterally ascending axon, optionally with a descending branch, were CiAs. Cells with commissural axons that bifurcated on the other side were CoBLs, unless the axon was myelinated in the commissural region and remained ventral and local to the segment, in which case they were CoLos. Unipolar cells with commissural axons that descended were UCoDs (we did not encounter a cell with that axonal trajectory that had a dendritic arbor as expected for the MCoDs). Commissural cells with an ascending axon were either CoSas or CoPAs. They were categorized as CoPA if they had large descending and ascending dendrites.

Comprehensive Detection of CiD Interneurons

Circumferential Descending (CiD) interneurons were comprehensively identified on one side of the tail, in the region rostral of the segment for which motoneurons had been identified, by placing seed points in the center of every soma in that area.

Annotators were instructed to follow a set of rules designed to rapidly stop tracing any neuron that could not be a CiD interneuron. 1) They were instructed to always prioritize tracing in the ventral direction at branch points and at soma exits, to make sure that the trajectory of the main axonal trunk, which is most useful for quickly eliminating tracings of other cell types, was quickly determined. 2) All tracings that crossed the midline in the ventral region of the spinal cord were to be canceled at that location. This rule avoids tracing all

commissural cell types. 3) All tracings that exited the spinal cord through a ventral root were to be canceled at that location. This rule avoids tracing motoneurons. 4) All glia tracings were to be canceled as soon as their identity became obvious. Glia were identified by a non-tubular, sheet-like morphology, and a less electron-dense membrane staining. Additionally, radial glia had a readily identified, prominent radial process running straight towards the surface of the spinal cord and forming a sheet lining the edge of the spinal cord. Oligodendrocytes formed small processes that were connected to the myelin sheets of neurons. Annotators were instructed to specify the rule they applied when canceling a tracing for one of these reasons.

These tracings were initially performed without redundancy, by only a single tracer. Each of the tracings that was canceled for one of the above reasons was inspected and the correct application of the rule was verified. Every tracing that was not canceled was additionally traced by two additional independent annotators. Of these tracings, those that had an ipsilaterally descending primary axon were retained as CiD interneurons.

Quantification of Neuron Location and Morphology

Soma sizes were measured by contouring the entire soma in sections spaced by 250 nm. The volume enclosed by these contours was calculated by triangulation. When reporting soma sizes as maximal cross-sectional areas, to allow a convenient comparison to published size measurements obtained from optical microscopy, the area was calculated from the volume by assuming spherical soma geometry. Soma locations were measured by calculating the center of mass of the contours and projecting that point onto manually drawn dorso-ventral (DV) and medio-lateral (ML) axes that were placed every 12.5 µm along the rostro-caudal length of the spinal cord. This approach yielded relative DV and ML positions for somata, independent of local differences in shape or rotation of the spinal cord, where the DV position was from 0 (most ventral) to 1 (most dorsal) and the ML position was from -1 (right) through 0 (medial) to 1 (left). When comparing the ML positions of groups of neurons, the absolute value of the ML positions was taken.

Neurite density contour plots were obtained by first interpolating tracings to a 50 nm inter-node distance and then calculating the 2-dimensional histogram of node positions projected onto the transversal plane, normalized as described above.

Gaussian Mixture Model of Motoneuron Soma Size Distribution

A Gaussian Mixture Model (GMM) was fit to the distribution of motoneuron soma sizes. The number of components (3) was chosen because it minimized the Akaike Information Criterion (AIC) and the Bayesian Information Criterion (BIC) and corresponded well to the visual appearance of the size histogram. The GMM was fit using the `sklearn.mixture.GMM` class of the scikit-learn (Pedregosa et al., 2011) Python module.

Principle Component Analysis and Clustering on Motoneuron Parameters

Principal Component Analysis (PCA) was applied to the motoneuron dataset to identify co-varying properties and to make any clusters more apparent. Motoneuron parameters included in the PCA analysis were 1) the normalized dorso-ventral soma position, 2) the normalized medio-lateral soma position, 3) the number of dendritic branch points, 4) the number of dendrites exiting from the soma, 5) the volume of the soma, 6) the total dendritic path length and 7) the number of axonal branch points. The number of input synapses was also included in an analysis restricted to the left hemisegment, since that parameter was not measured for both hemisegments, but did not change the overall results. PCA was performed using the PCA function of the FactoMineR package (Le et al., 2008) for R (R Core Team, 2013). Clustering and cluster count estimation was performed on the PCA-transformed data using the HCPC function, also of the FactoMineR package.

Motoneuron Size Weighted Average for Interneurons

To quantify the wiring selectivity of motoneuron-contacting interneurons to motoneurons of different sizes, a synapse size weighted motoneuron size average was calculated as follows for every interneuron *j:* $p_j = \sum_i w_{ji} s_i$, where the summation is over all motoneurons *i*, w_{ji} is the summed synaptic contact size from interneuron *j* to motoneuron *i* and s_i is the soma size of motoneuron *i*.

Approximate Permutation Testing of CiD to Motoneuron Specificity

To test the statistical significance of differences in motoneuron-subtype contact specificity for different subtypes of CiD interneurons, a permutation test was performed. The dorso-ventral positions of the CiDs were randomly shuffled and the ratio of CiD synaptic weights on PMNs versus SMNs was calculated for the more dorsally (> 0.75 dorso-ventral position, named “dorsally displaced CiDs”) and more ventrally (≤ 0.75 dorso-ventral position, named “standard CiDs”) located CiD subsets. The random shuffling was repeated 10000 times and the two-sided p-value was calculated from the number of results that were more extreme than that actually measured.

Estimation of Zebrafish Brain SBEM Stack Acquisition Duration

A precise measurement of the geometry of a 5 dpf zebrafish brain was obtained by anaesthetizing a larva in MS-222, as described above. Sulforhodamine 101 (ThermoFisher Scientific), dissolved in modified teleost ACSF (Gabriel et al., 2012) was injected through the skin, into the ventricle, using a glass pipette with a tip diameter of ca. 2 µm, obtained as described above. The Sulforhodamine intensely stained the extracellular space of the brain, allowing a clear delineation of its shape. Optical imaging was performed on a SP5 confocal microscope (Leica). The brain was manually reconstructed from these images using ImageJ (Schneider et al., 2012) and rendered using the Amira 3-dimensional visualization tool (FEI).

The number of slices required to cover the entire brain at a section thickness of 25 nm was measured using this reconstructed brain, assuming a sectioning plane rotated by 35° in yaw from the transversal plane. The time required for sectioning was calculated from the expected number of slices, assuming 45 s required for sectioning per slice. The area to be scanned per slice was also predicted from the reconstructed brain, disregarding tile-tile overlaps, which accounted for less than 10% of the total area. The imaging time was calculated from the areas for each slice, assuming a pixel size of 14 x 14 nm, a pixel dwell time of 200 ns, a tile width of 3000 pixels and a maximal tile height of 32768 pixels, which was never reached. The time spent moving the stage motors was calculated from the predicted number of tiles, assuming a duration of 3 s per tile move.

Brain Imaging During Opto-Kinetic Stimulation

These experiments were performed as part of a collaborative project with Dr. F. Kubo, in the group of Prof. Dr. H. Baier at the Max Planck Institute of Neurobiology, Martinsried. Dr. F. Kubo performed the 2-photon imaging experiments and analyzed the 2-photon Calcium imaging data. I performed all electron microscopy related preparations and imaging.

Two-photon calcium imaging during optokinetic response (OKR) inducing visual stimulation was performed in the pretectum of a 5 dpf zebrafish larva as previously described (Kubo et al., 2014). Briefly, *elval3:GCaMP5G* fish were shown moving gratings that could be independently displayed to the two eyes using a custom-built LED array. All $2^3 = 8$ combinations of temporalward grating motion, nasalward grating motion and no stimulation were displayed with three repetitions. The experiment was repeated for 8 imaging planes separated by 5 µm dorso-ventrally, to cover the pretectum completely. After the functional imaging experiment, an overview stack (512 x 512 x 48 pixels, 385 x 385 x 1000 nm) of the pretectum and surrounding regions was taken. Custom MATLAB™ (The Mathworks, Inc.) code was used to identify pretectal cells that were specifically activated by subsets of the visual stimuli.

Brain Stack Reconstructions

The two-photon overview stack was registered to a low-resolution version of the EM stack to find back individual somata identified by functional Calcium imaging. Custom registration software was developed in Python by C. Cascio, under my direct supervision. The software was then used by Dr. F. Kubo. The tool allowed corresponding locations to be selected in the EM and optical stacks. In particular, blood vessels could be easily identified in both stacks and were used as starting points for the selection of correspondence points. Once a series of correspondence locations was selected, the software optimized an affine transformation by minimizing the correspondence point distance. This allowed the two-photon stack to be transformed so that it could be overlaid over the EM data to find corresponding somata.

Statistics

Unless otherwise specified, the unequal variance t-test was used to test for significant differences of population means, using the `stats.ttest_ind` function of the SciPy Python module. Ranges reported around means are one standard deviation.

Results

Connectomic Analyses in the Spinal Cord

The spinal cord of the larval zebrafish contains a central pattern generator (CPG) for swimming. CPGs for swimming have been found to follow a simple ground plan: Rhythmic motor nerve bursts, traveling down the length of the tail, are generated by ipsilaterally projecting, primarily descending, excitatory interneurons, while commissural inhibitory interneurons ensure left-right burst alternation. The excitatory interneurons are known as Circumferential Descending (CiD) in the larval zebrafish, while the commissural inhibitory ones are called Commissural Bifurcating Longitudinal (CoBL). This ground plan has been elucidated primarily through physiological means, by which fine-grained connectivity between populations of cells is difficult to map. Yet, it is likely the detailed connectivity between CiD interneurons and motoneurons (MNs) that mechanistically explains the orderly recruitment of MNs during swims of different speed (Figure 9). Therefore, a detailed mapping of that connectivity using volume electron microscopy based circuit reconstruction was undertaken.

In addition to the CPG for swimming, the spinal cord contains elements dedicated to specific behaviors. A prominent example is the Mauthner axon, which causes a short latency, C-shaped bending of the tail which is used in escapes. The Mauthner axon contacts MNs as well as a range of interneurons in the spinal cord. Since the Mauthner axon based escape network has been particularly intensively investigated in goldfish, detailed predictions exist regarding its connectivity in larval zebrafish (Figure 10). The Mauthner escape network therefore provides a convenient entry point for circuit reconstructions, since it allows the traceability of a spinal cord dataset to be evaluated.

SBEM Stack Acquisition in the Spinal Cord

To enable the reconstruction of complete spinal neuron morphologies and, in particular, of complete motor neuron pools together with large fractions of their presynaptic inputs, a Serial Block-Face EM (SBEM) dataset of the spinal cord of a 6 dpf larval zebrafish was acquired from a sample of the tail freshly cut from an anesthetized fish. Extracellular space (ECS) was preserved by spinal

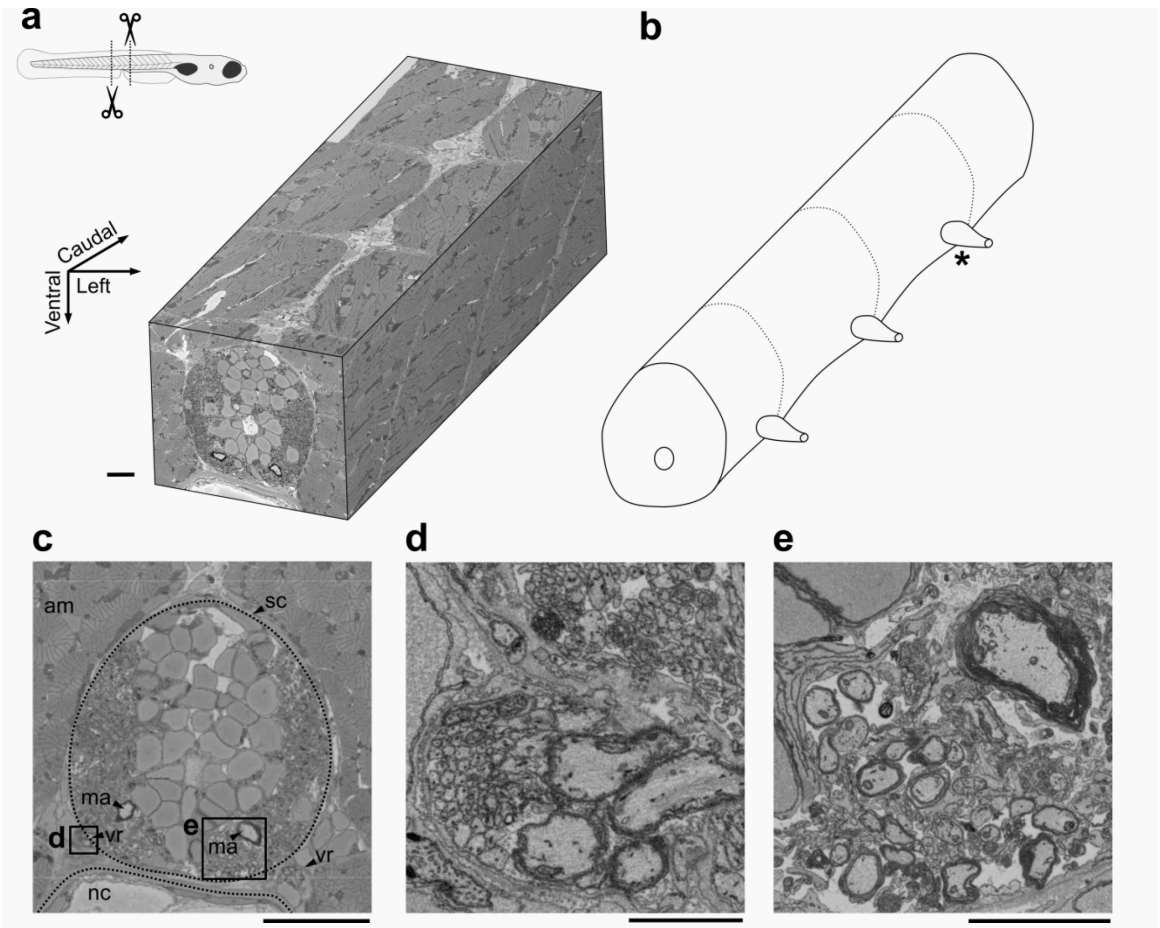

Figure 13 | SBEM dataset of a larval zebrafish spinal cord sample. (**a**) Location of tissue sampling and overview of the SBEM dataset. The spinal cord with its surrounding muscles and the notochord are visible. Scale bar: 10 µm. (**b**) Schematic drawing of the piece of spinal cord contained in the dataset. Two complete segments are contained and two partial segments are contained at the ends. Asterisk marks ventral root of segment chosen for motoneuron identification. (**c**) Transversal overview of the dataset, showing anatomical features visible at a coarse overview level. The medial region of the spinal cord contains the somata, the lateral region is neuropil. sc: spinal cord, am: axial musculature, ma: Mauthner axon, vr: ventral root, nc: notochord. Scale bar: 20 µm. (**d**) Close-up of ventral root, with four large, myelinated axons and a larger number of small, unmyelinated ones. Scale bar: 2 µm. (**e**) Close-up of ventral longitudinal fasciculus (vlf), with large myelinated axons, including the Mauthner axon. Scale bar: 5 µm. *This figure is adapted from a manuscript in preparation (Svara et al.).*

injection of an artificial cerebro-spinal fluid (ACSF) solution containing cell-impermeable cesium gluconate. This was found to be essential to achieve

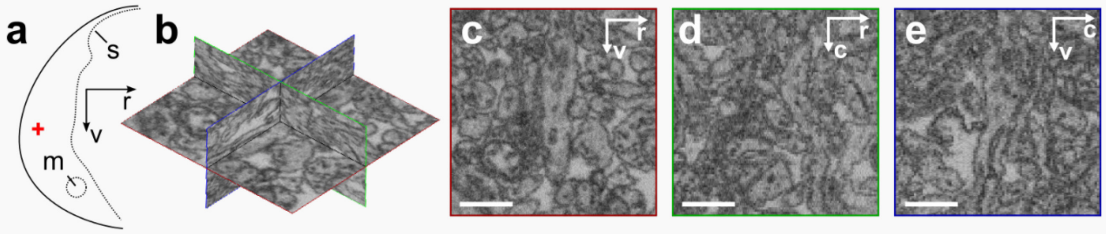

Figure 14 | Physical and virtual slices of the spinal cord SBEM dataset. (**a**) Neuropil location (red cross) chosen in this example. (**b**) Three-dimensional view of the orthogonal slices. (**c**) Transverse (physical section) view. (**d**) Coronal virtual slice view. (**e**) Parasagittal virtual slice view. Scale bars: 500 nm. m: Mauthner axon, s: soma / neuropil boundary, v: ventral, r: right. c: caudal.

good fixation and staining results, presumably because it improved the diffusion of chemicals from the cut locations into the spinal cord. The sample was fixed using glutaraldehyde, stained with osmium tetroxide, lead aspartate and uranyl acetate and embedded in plastic.

SBEM imaging was performed at a resolution of 9 x 9 x 21 nm, sufficient both to follow fine neurites and to identify synaptic contacts (Figure 13a, see Figure 22b, c for individual synapse examples). The final dataset contained complete transversal sections of the spinal cord, including some of the surrounding tissue: 8 – 15 µm of the dorsal part of the notochord, 13 – 21 µm on the left side of the lateral musculature, 5 – 13 µm on the right side and 7 – 15 µm of dorsal musculature. Ranges are reported here instead of exact values due to small changes in the imaging position and in the shape and rotation of the spinal cord over the length of the stack. The total length of the dataset was 207 µm, containing two complete segments and two partial segments at the rostral and caudal ends (Figure 13b). One of the two complete segments was the anal pore segment, segment 15. The rostro-caudal lengths of the two fully contained segments were found to be 65 and 64 µm. Using the mean of the two as the expected length for the neighboring segments, the rostrally adjoining partly contained segment was found to be contained to 51% (33 µm) and the caudally adjoining one was 71% (46 µm) contained. The mean transversal area of the spinal cord was 2010 µm², the mean maximal dorso-ventral extent was 52 µm and the mean maximal left-right extent was 47 µm.

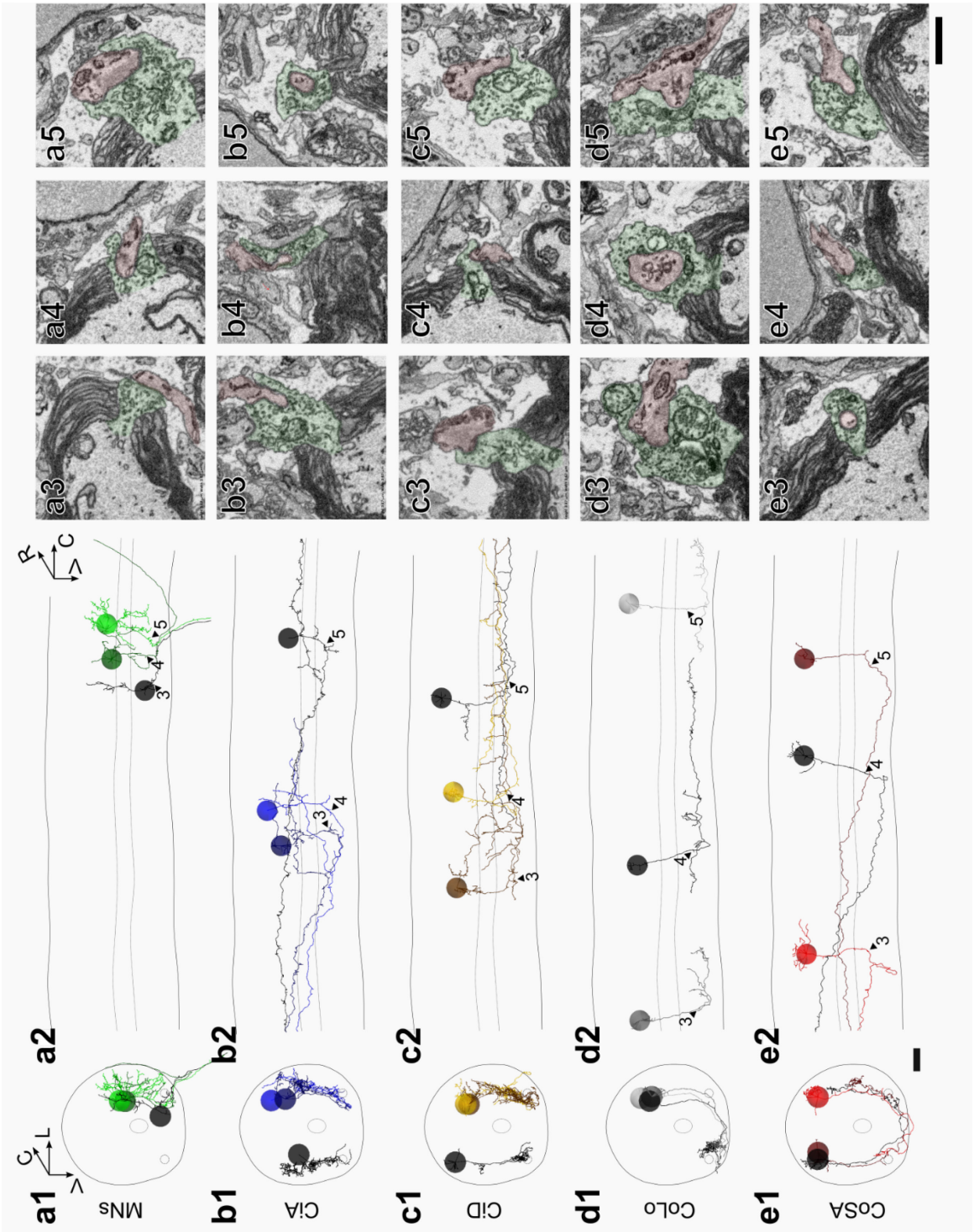

Figure 15 | Examples of different types of neurons postsynaptic to the Mauthner axon. (**a1**) Transverse view of motoneurons. The light green cell is a primary motoneuron (CaP). (**a2**) Same neurons as in a1, in sagittal view. Numbered arrowheads refer to the EM data views in panels 3-5. (**a3-5**) Transverse views of Mauthner synapses for the MNs. (**b1-5**) As in a, for Circumferential Ascending (CiA) interneurons. (**c1-5**) As in a, for Circumferential Descending (CiD) interneurons.

(**d1-5**) As in a, for Commissural Local (CoLo) interneurons. Note the distinct synaptic ultrastructure, which presumably represents an electrical contact. (**e1-5**) As in a, for Commissural Secondary Ascending (CoSA) interneurons. Scale bars for columns 2 and 3: 10 µm, Scale bar for columns 3, 4 and 5: 1 µm. R: right, L: left, V: ventral, C: caudal.

A range of anatomical features were readily distinguished even at a low-resolution overview level. At the ventral roots, axon bundles exited the spinal cord, running into the surrounding lateral musculature (Figure 13c, d). Large myelinated axons coursed longitudinally in the ventral and dorsal regions of the neuropil (Figure 13c, e), making up the ventral and dorsal longitudinal fasciculi (vlf, dlf), respectively. These tracts contain the reticulospinal axons descending from the hindbrain. The Mauthner axon was easily identified on both sides as the largest and most strongly myelinated axon in the vlf. At two locations in the dataset (one on the right side, one on the left side), the ventral roots were split into two smaller axon bundles exiting the spinal cord separately in close proximity (compare Figure 16).

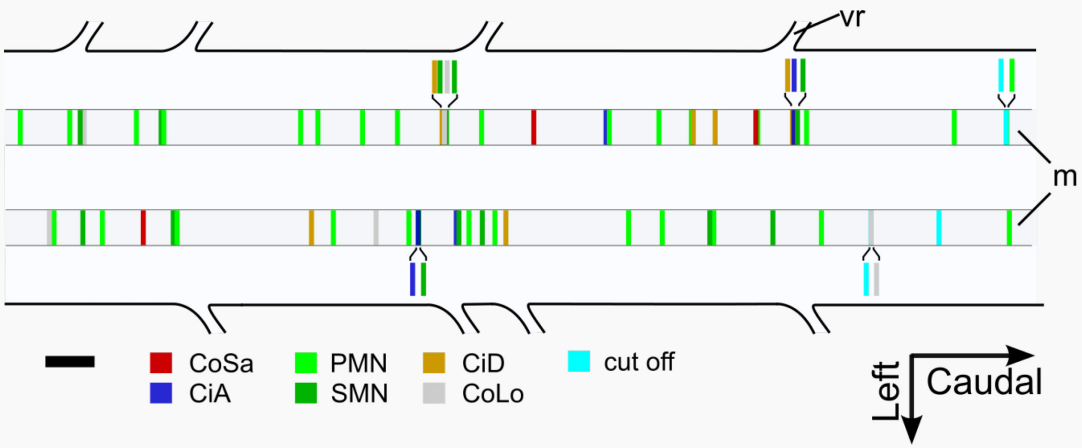

Figure 16 | Overview of Mauthner synapse locations and type of postsynaptic neurons contacted at those locations. m: Mauthner axon, vr: ventral root. PMN: Primary Motoneuron, SMN: Secondary Motoneuron, cut off: neuron type classification was not possible because a large part of the tracing was cut off at the dataset boundaries. Other abbreviations, as well as colors, as in previous figure. Scale bar: 10 µm.

The somata contained in the spinal cord were counted by placing a node in the center of every spinal soma, revealing a total number of 2177 somata, corresponding to 676 somata per segment.

Since the sectioning resolution was not much lower than the imaging resolution, the volume EM data could not only be interpreted in the original transverse view, but could be virtually resliced and interpreted in parasagittal and coronal views, too (Figure 14).

The Spinal Cord Escape Network

In order to confirm the traceability of the dataset, the possibility to detect synaptic contacts and the possibility to identify neuron types based on morphology, the postsynaptic partners of the two Mauthner axons were reconstructed. The Mauthner synapses have an unusual morphology, in that they consist of short vesicle-filled stubs, 1 – 2 µm in length, that sprout from the

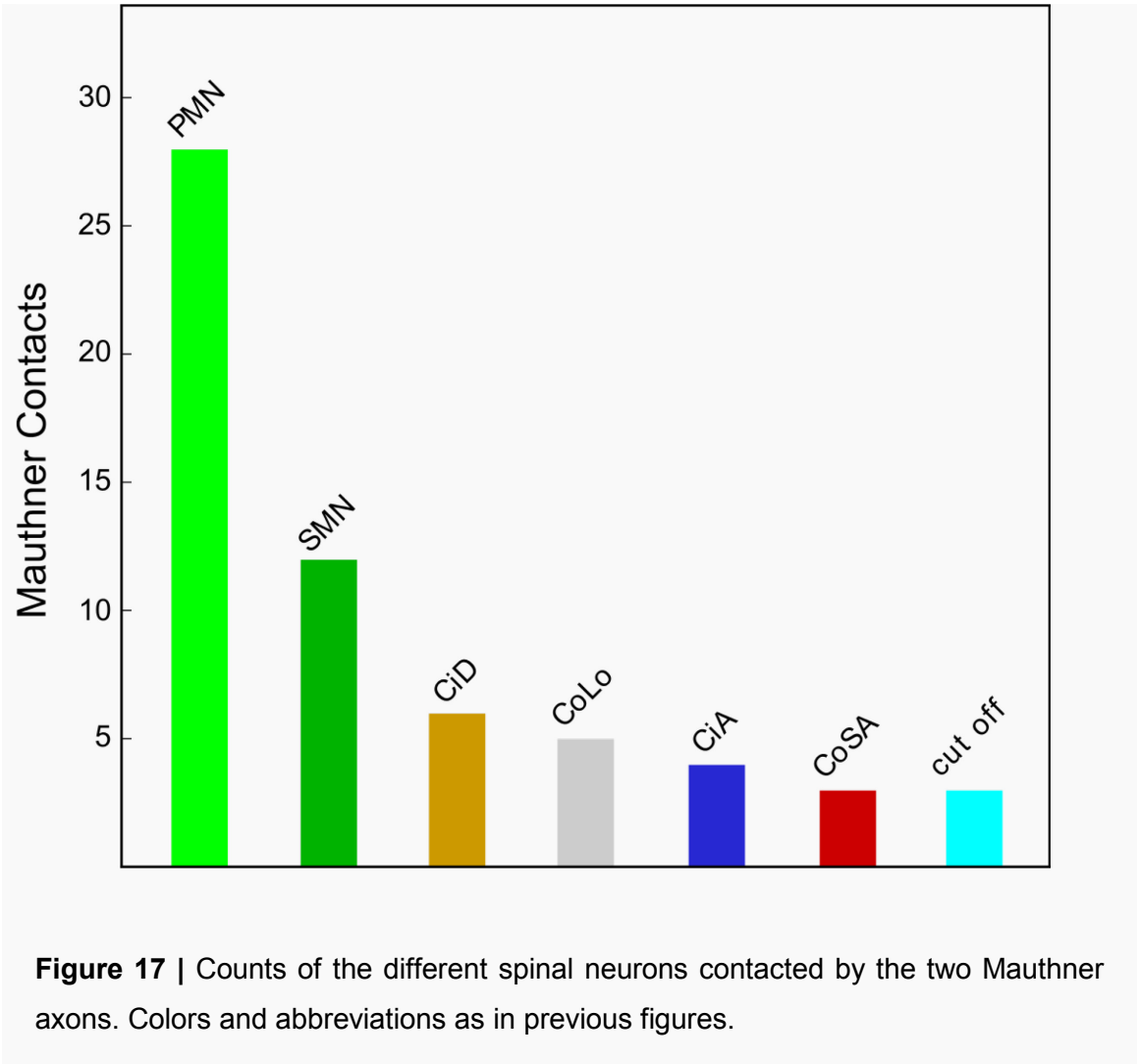

Figure 17 | Counts of the different spinal neurons contacted by the two Mauthner axons. Colors and abbreviations as in previous figures.

main Mauthner axon trunk and break through the myelin sheet (see Figure 15, columns 3 – 5 for examples). The myelination is not interrupted and the branching does not occur at nodes of Ranvier. In fact, the whole dataset does not contain any location at which the Mauthner axon myelination is interrupted. For the left Mauthner axon, 23 of these locations were found, versus 22 for the right one, corresponding to an average distance of 9.2 µm between stubs. In most of these cases (total: 31 / 45, left side: 17 / 23, right side: 14 / 22), exactly one postsynaptic neuron was contacted per stub, but in some cases (total: 13 / 45, left side: 6 / 23, right side: 7 / 22), two contacts were made on the same stub and in one case on the right side 4 contacts were made on the same stub. Thus, in total, the left Mauthner axon made 29 different synapses with spinal neurons and the right one made 32, corresponding to an average of 9.5 spinal neurons contacted per hemisegment. The cell types were categorized based on morphology (see Figure 16 for an overview of Mauthner synapse locations), revealing that by far the most commonly contacted neurons were, as expected, primary motoneurons (PMNs) (total: 28 / 61, left: 12 / 29, right: 16 / 32). Both of the Mauthner axons contacted exactly 4 PMNs in each of the fully contained central segments. These fit the morphological descriptions of the four individually described dRoP, vRoP, MiP and CaP PMNs (Menelaou and McLean, 2012; Myers et al., 1986), suggesting that the Mauthner axon makes synapses with all or almost all PMNs. The next most commonly contacted cells were secondary motoneurons (SMNs) (total: 12 / 61, left: 7 / 29, right: 5 / 32), revealing that the Mauthner axon contacts SMNs not only indirectly as previously thought (Fetcho, 1991), but also makes some direct SMN synapses. Conspicuously, three of these SMNs had ventral somata (normalized dorso-ventral positions: 0.18, 0.26 and 0.32), placing them amongst the most ventral MNs (Menelaou and McLean, 2012) (compare also Figure 19). Since ventral SMNs are typically considered to be weak MNs, this observation could hint at a special functional role for these very ventral SMNs. The third most commonly targeted cells were Circumferential Descending (CiD) interneurons (total: 6 / 71, left: 2 / 29, right: 4 / 32), also in agreement with expectations. The fourth most common contacts were contacts with Commissural Local (CoLo) interneurons (total: 5 / 61, left: 3 / 29, right: 2 / 32). The functional role of the homologs of these interneurons in goldfish is thought be to ensure that a

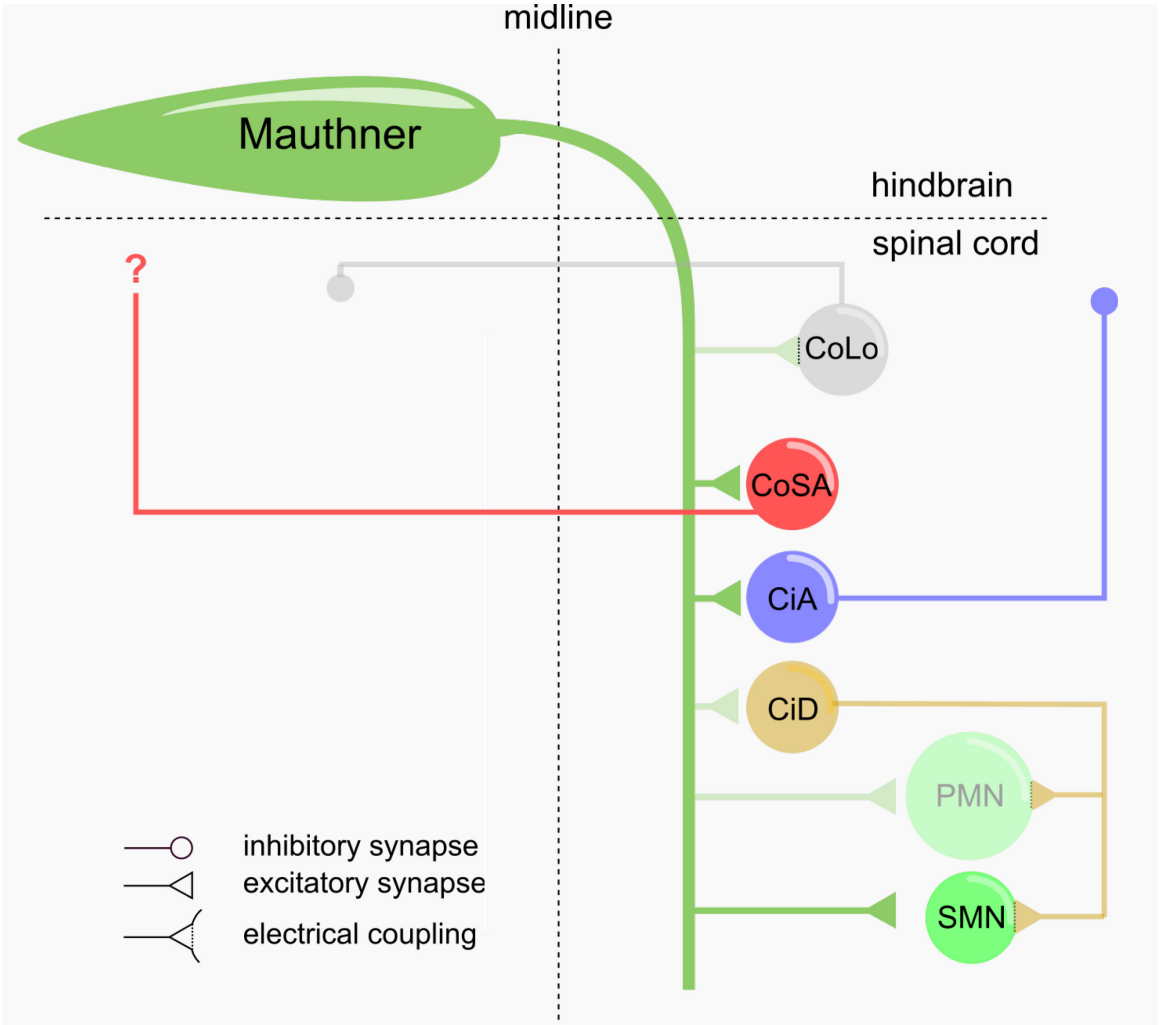

Figure 18 | Schematic Mauthner Escape Network. Connections that have been previously described (PMN, CiD and CoLo, compare Figure 10) are drawn more lightly than connections newly identified in this work. Colors and abbreviations as in previous figures.

Mauthner-initiated C-bend can only occur on one side of the tail at the same time, to avoid the fish becoming immobilized in the attempt to escape into two directions simultaneously. The Mauthner contact with these interneurons was described to be electrical (Fetcho and Faber, 1988). Indeed, these synapses were ultrastructurally distinct from other synapses made by the Mauthner axon (compare Figure 15d).

There was no detectable synaptic cleft over most of the contact area and the pre- and postsynaptic membranes came so close to each other that they became indistinguishable and appeared as a single membrane (Figure 15d3-5). Just after the Mauthner contact, the axons of the CoLo cells increased in

diameter (mean diameter: 1.3 µm), became myelinated and crossed to the contralateral side. These were the only myelinated commissural axons detected in this dataset. Notably, exactly 1 CoLo cell was found per hemisegment for the fully contained segments. Taken together, these observations suggest that there is exactly 1 CoLo cell per hemisegment, responsible for shutting down its contralateral partner segment during C-bends. All further detected types were relatively rare (Figure 16, 17), but not expected to be contacted by the Mauthner axon based on previous physiological work (Figure 10). Circumferential Ascending (CiA) cells (left: 2, right: 2) are inhibitory and may be involved in termination of the C-bend motor bursts. The Commissural Secondary Ascending (CoSA) cells identified here (left: 1, right: 2) cannot be unambiguously assigned to a cell type, since cells of that morphology were shown to have both an excitatory and an inhibitory subtype (Higashijima et al., 2004b). A few cells were not assigned to any cell type because they were cut off by the boundaries of the dataset (left: 2, right: 1). See Figure 17 for a summary of these counts and Figure 18 for a schematic summary drawing of the escape network as revealed by these reconstructions.

Identification and Characterization of the Motoneuron Pool

The reconstructions of the Mauthner-postsynaptic escape network confirmed the traceability of the data by confirming all connections expected by homology from goldfish, but also revealing additional details not described in previous physiological experiments. Therefore, it appeared promising to use the dataset for a comprehensive reconstruction and characterization of the MN pool, aimed at understanding the mechanisms of orderly recruitment of MNs. MN pools in the larval zebrafish have not been characterized in an unbiased, comprehensive fashion up to now. Yet, the distribution of MN sizes within a pool must be known in order to understand MN recruitment mechanistically. The MN size distribution alone would already be potentially instructive in constraining recruitment mechanisms, since the MN pool could either be organized into a small number of distinct subtypes separated by size, as described in adult fish (Ampatzis et al., 2013), or could consist of MNs gradually distributed in size, as suggested for larvae (Menelaou and McLean, 2012).

To identify all MNs in an unbiased way, a seed point was placed in every axon exiting through the ventral roots of the more caudal of the two fully contained segments (asterisk in Figure 13b). From that seed point, annotators traced forward into the lateral musculature and backwards into the spinal cord,

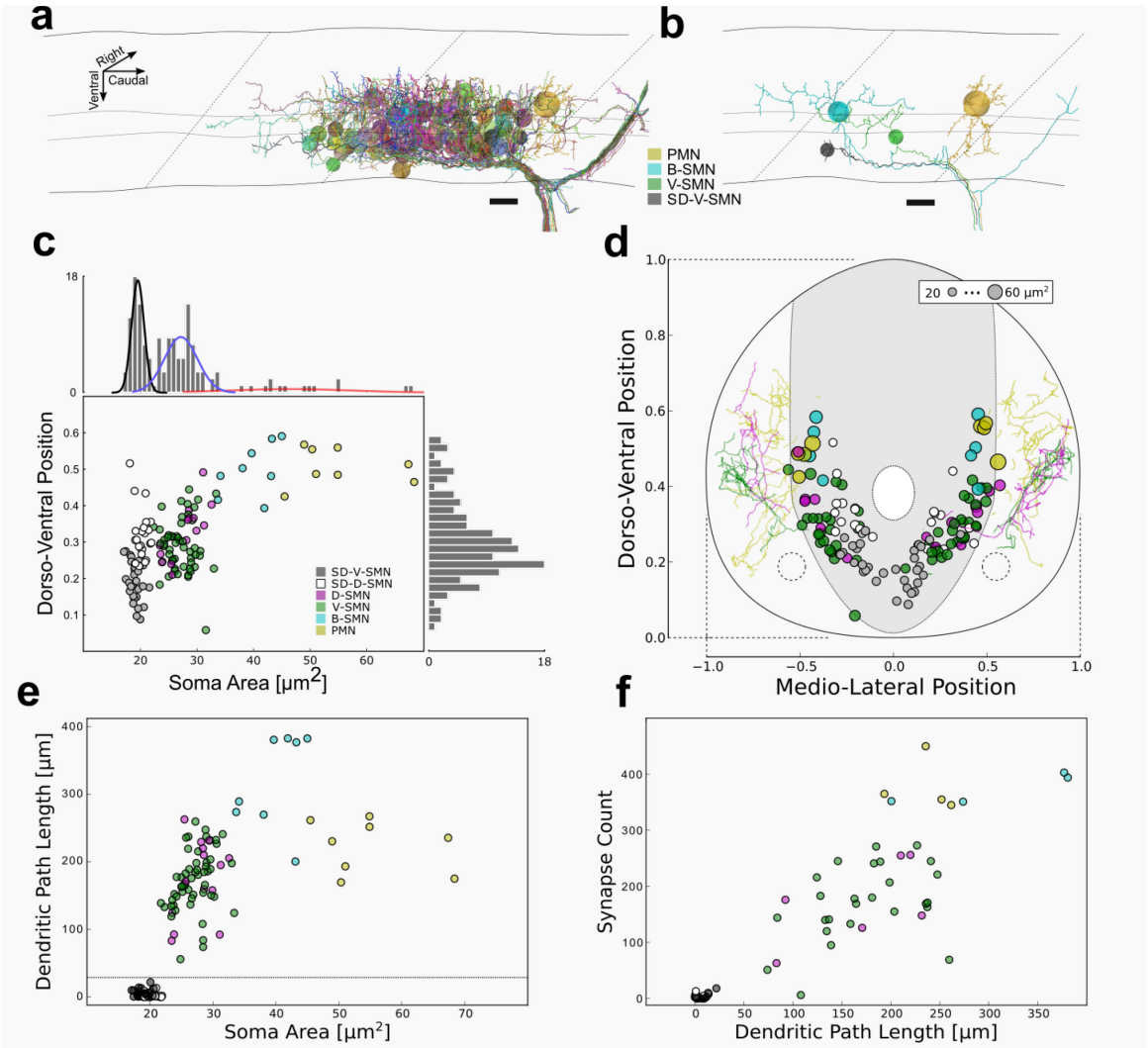

Figure 19 | Comprehensive Identification and Characterization of Motoneurons. (**a**) All 68 motoneurons (MNs) in the left hemisegment. Soma sizes represent the measured volumes of the somata, but are drawn as spheres for clarity. Scale bar: 10 µm. (**b**) Individual examples of MNs of different types. PMNs and bifurcating secondary MNs (B-SMNs) have large, dorsal somata. Ventrally projecting SMNs and ventrally projecting SMNs with short dendrites (V-SMNs and SD-V-SMNs) have small, ventrally located somata. Scale bar: 10 µm. (**c**) Scatter plot of normalized soma dorso-ventral position vs. cross-sectional area, with histograms of both measures. Colored Gaussian fits of soma area are the results of a Gaussian

mixture model. (**d**) Normalized dorso-ventral vs. medio-lateral positions of MN somata. Areas are proportional to soma cross-sectional areas, but not drawn to scale for clarity. Examples of the dendritic trees of a PMN, D-SMN and V-SMN are shown on each side. Grey shaded area represents the soma layer, ventrally located dotted circles represent the locations of the Mauthner axons, centrally located dotted circle represents the location of the central canal. (**e**) Total dendritic path length vs. cross-sectional soma area. Note separation of SD-SMNs from other MNs based on dendritic path length. Dotted line represents dendritic path length threshold used for separation (30 µm). (**f**) Synapse counts vs. total dendritic path length are linearly correlated ($r^2 = 0.79$, $p < 0.01$). Note scarcity or even absence of synaptic inputs onto SD-SMNs. *This figure is adapted from a manuscript in preparation (Svara et al.).*

revealing the MN's complete morphology up to the initial course of the axon into the lateral musculature (Figure 19a, examples in b). There were 68 MNs in the left hemisegment and 71 in the right one. To measure the size of the MN somata, annotators were asked to contour them. The volumes and cross-sectional areas were computed from these contours. Additionally, for the left hemisegment only, annotators labeled all locations at which a synapse was made onto a MN. These annotations allowed the quantification of a range of morphological parameters: 1) The normalized dorso-ventral position of the soma, 2) its normalized left-right position, 3) its rostro-caudal position, 4) the number of dendrites exiting from the soma, 5) the total dendritic path length, 6) the size of the soma, 7) the number of branches made by the axon within the spinal cord, 8) whether the initial course of the axon outside of the spinal cord was dorsal, ventral or bifurcating (both dorsal and ventral), 9) whether the axon was myelinated and 10) how many synaptic inputs were received, for the MNs of the left hemisegment (see Figure 20 for a visualization of all non-categorical morphological features available for both hemisegments).

The plot of the dorso-ventral soma position against the cross-sectional soma area (Figure 19c) suggested a categorization of the MN pool into three sub-classes: There was a population of MNs with small somata (soma cross-sectional area 19.5 ± 1.1 µm²), that tended to be ventral (normalized dorso-ventral position 0.25 ± 0.08), another population of larger MNs (soma area

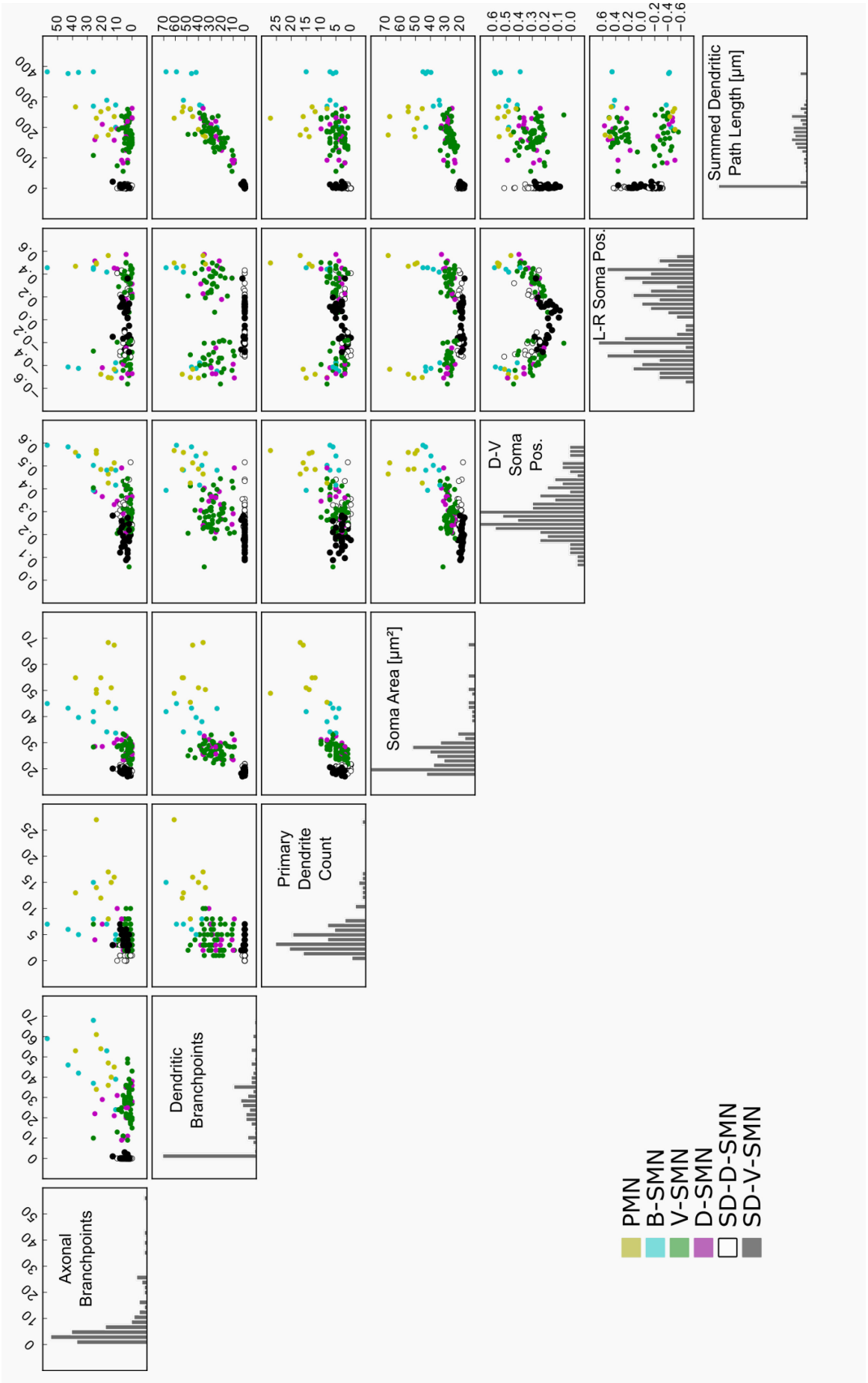
Axonal Branchpoints
Dendritic Branchpoints
Primary Dendrite Count
Soma Area [µm²]
D-V Soma Pos.
L-R Soma Pos.
Summed Dendritic Path Length [µm]
PMN
B-SMN
V-SMN
D-SMN
SD-D-SMN
SD-V-SMN

Figure 20 | Scatterplot matrix for all non-categorical parameters measured for all motoneurons in a spinal segment. Note that particularly the soma size, normalized dorso-ventral soma position and dendritic path length, support a categorization into three sub-classes. Compare also Figure 21a for a visual representation of these parameters. *This figure is adapted from a manuscript in preparation (Svara et al.).*

27.2 ± 2.7 µm²) that were slightly more dorsal (normalized dorso-ventral position: 0.30 ± 0.07) and MNs that were large (47.5 ± 9.9 µm²) and dorsal (normalized dorso-ventral position: 0.50 ± 0.06).

The small MNs were also separated from other MNs by their dendritic path length, which was very short (Figure 19e) (small-soma MNs: 3.8 ± 4.6 µm, all other MNs: 191.3 ± 65.1 µm, $p < 0.001$). They will therefore be referred to as short-dendrite secondary MNs (SD-SMNs). For all the MNs in this group, the initial trajectory of the axon outside the spinal cord was either in the ventral (V) or dorsal (D) direction, allowing further subdivision into SD-V-SMNs and SD-D-SMNs. The SD-D-SMN somata were located more dorsally in the spinal cord than the SD-V-SMN somata (SD-D-SMN: 0.32 ± 0.07, SD-V-SMN: 0.20 ± 0.05, $p < 0.001$) and all SD-SMN somata were located more medially than other MN somata (Figure 19d, normalized medio-lateral position for SD-SMNs: 0.20 ± 0.10, other MNs: 0.37 ± 0.11, $p < 0.001$). Since the SD-SMNs had very short dendrites or even no dendritic trees at all and since they received very few or no synapses (Figure 19f), it is unlikely that they represent functional MNs at this developmental stage. They may be developing in parallel to slow muscle fibers, which are also not yet fully developed at 6 dpf (Devoto et al., 1996), which would also be consistent with the fact that their number was similar to the number of red muscle contacting MNs described in previous studies (van Raamsdonk et al., 1983).

The large MN subtype was made up of a set of cells that, in addition to having very large and dorsal somata, had large, myelinated axons and a dense endoplasmic reticulum (ER) network in the cytoplasm of their somata. These were the only MNs with myelinated axons and there were exactly 4 of them per hemisegment. Their morphology corresponded to the individually described CaP, MiP, vRoP and dRoP morphologies, leading to the conclusion that these

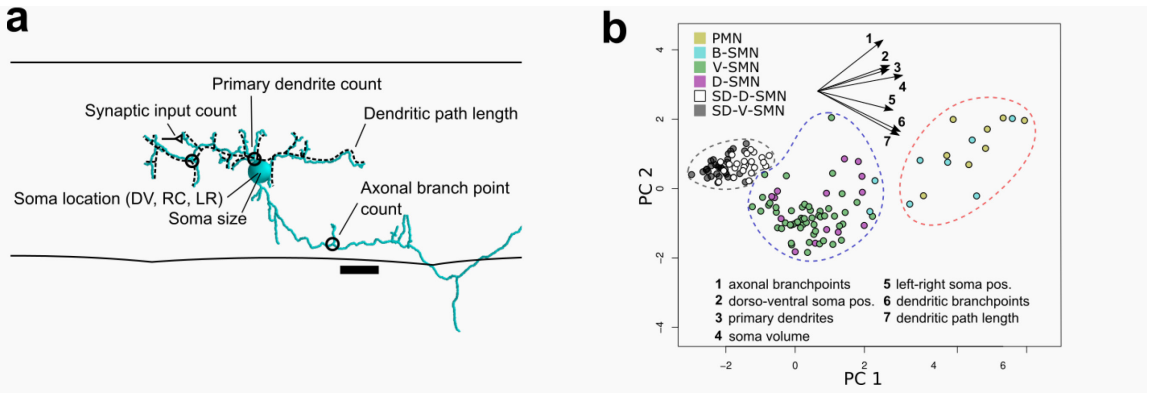

Figure 21 | Principal component analysis and hierarchical clustering on the MN dataset. (**a**) Overview of all MN parameters included in Principal Component Analysis (PCA). Scale bar: 10 µm. (**b**) MN dataset in the space of the first two principal components (PCs). Note that most of the variation is captured by PC1, which mostly correlates with different aspects of MN size and position. Dotted lines represent the results of a hierarchical clustering on the PCA dataset, with cluster counts estimated based on the elbow method. The colors (black: small MNs (SD-SMNs), blue: intermediate MNs (D- and V-SMNs), red: large MNs (B-SMNs and PMNs)) approximately correspond to the colors in Figure 19c. *This figure is adapted from a manuscript in preparation (Svara et al.).*

represent the PMNs. The large MNs, in addition to the PMNs, also contained a set of cells that had slightly smaller somata and did not have myelinated axons.

Their axons bifurcated shortly after the ventral root and had a dorsally projecting and ventrally projecting branch. These are referred to here as bifurcating SMNs (B-SMNs), since their morphology does not fit any of the known PMN morphologies well.

The intermediate MNs lay between the small and large MNs in size and were broadly distributed in dorso-ventral position. Subdividing them based on the initial trajectory of their axons into D-SMNs and V-SMNs did not reveal any additional structure (D-SMNs and V-SMNs in Figure 19c, d, e, f).

The visual impression of a clustering into three subtypes was supported by an unbiased estimation of the number of components for a Gaussian mixture model (GMM) of the soma size distribution, using the Bayesian information criterion (BIC), which was minimal for three components (the GMM fit is shown

overlaid on the soma size histogram in Figure 19c; black: small MNs, blue intermediate MNs, red: large MNs).

The distribution of MN sizes and dorso-ventral positions suggested three underlying populations, corroborated by the GMM fit and the fact that the three populations were also separated in other dimensions, such as the axonal trajectory and dendritic path length (Figure 19, 20). Yet, the boundaries between the presumed subclasses were not completely sharp. In particular, the B-SMNs fell between the very large PMNs and the intermediate MNs in size. In order to obtain a clearer separation between the three classes, all non-categorical morphological parameters (Figure 20, 21a) were used for a principal component analysis (PCA, see Methods).

Most of the separation of the MNs in principal component (PC) space was along the first PC, which was well correlated with soma size (Figure 21b). Additionally, hierarchical clustering with cluster count estimation based on the elbow method (Le et al., 2008), was performed on the PCA dataset (black, blue and red dotted lines in Figure 21b indicate cluster boundaries and correspond

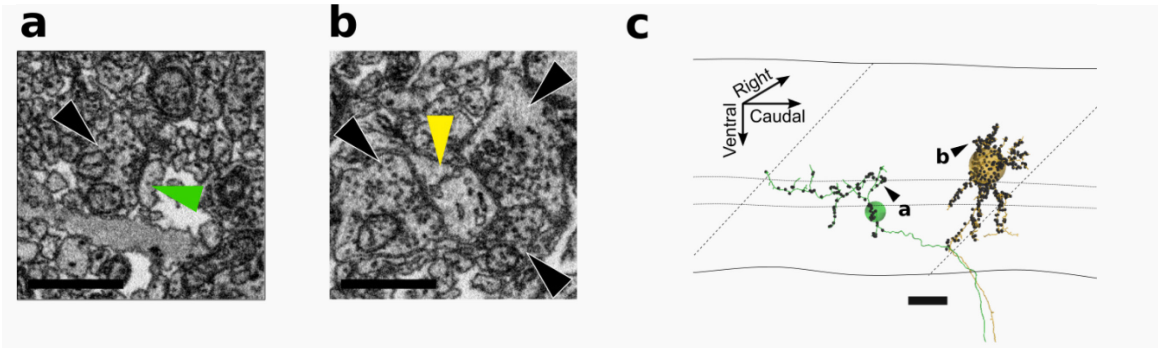

Figure 22 | Synapses on motoneurons. (**a**) Example synapse on an intermediate MN of the V-SMN type. Black arrowhead indicates presynaptic structure; green arrowhead indicates postsynaptic dendrite. Scale bar: 1 µm. (**b**) Example synapse on a large MN (the CaP PMN). Black arrowheads indicate presynaptic structures; yellow arrowhead indicates postsynaptic dendrite. Scale bar: 1 µm. (**c**) Three-dimensional rendering of two MNs with black spheres indicating synaptic locations. There are 92 synaptic locations on the V-SMN and 403 on the PMN. Arrowheads indicate locations of synapses shown in panels (a) and (b). Scale bar: 10 µm. *This figure is adapted from a manuscript in preparation (Svara et al.).*

approximately to the colored lines in Figure 19c). While PCA retained the overall structure visible in the plot of dorso-ventral position versus soma size, it improved the separation of large MNs from intermediate MNs only marginally and did not appear to make the categorization of the B-SMNs clearer. In fact, in PC space, most B-SMNs and PMNs were less well separated and two B-SMNs were placed close to the intermediate MN group. At the level of pure MN morphology, the boundaries between MN subtypes of different size therefore remain slightly blurry.

Presynaptic Partners of Motoneurons

The reconstruction and morphological characterization of a complete MN pool had revealed that the pool was structured into subsets of smaller and larger MNs. Larger, more dorsal MNs have been shown to be recruited only during strong swims in larval zebrafish (McLean et al., 2008) and it can therefore be assumed that the MN subpopulations identified here on the basis of morphology are differentially recruited during swims of different strength. To find out whether the different MN subsets were embedded into different presynaptic networks that may underlie their differential recruitment, their presynaptic partners were identified. Since 8579 synapses were made onto the MNs in the left hemisegment, a complete mapping of these presynaptic inputs was not feasible in a realistic time frame. Instead, a representative large MN (the CaP PMN) and a representative intermediate MN (a V-SMN, the more common type of intermediate MN) in the left hemisegment were selected. No MN of the small class was selected, since these neurons presumably are not yet functional at this developmental stage and since they have very few or no presynaptic partners in the first place. There were 92 synaptic locations on the V-SMN and 403 on the PMN (Figure 22). For each of these presynaptic locations, redundant manual tracings were performed to identify the type of the cell making the synaptic contact. Note that the counts reported for the different cell types in the following paragraphs are, unless otherwise specified, the counts of individual synaptic locations of a given type and do not necessarily correspond to as many distinct presynaptic cells, since the same cell can make several synapses with the same MN.

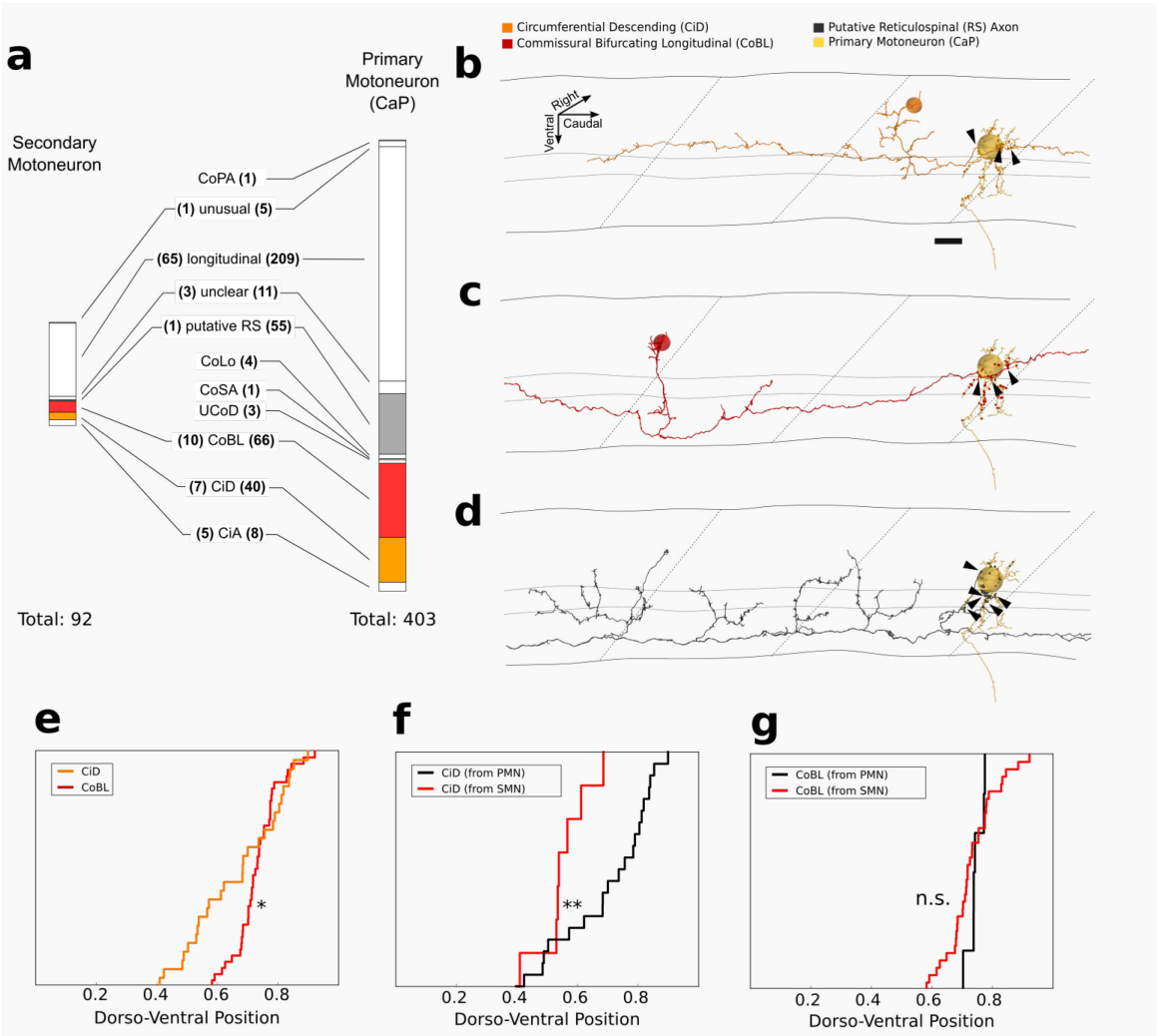

Figure 23 | Different types of neurons identified by back-tracing from motoneurons. (**a**) Counts of the different classes of tracings. CoPA: Commissural Primary Ascending, RS: reticulospinal; UCoD: Unipolar Commissural Descending; CoBL: Commissural Bifurcating Longitudinal; longitudinal: axons that exited the dataset without having a soma within the dataset and that could not further be categorized as RS; unclear: tracings that did not contain a soma and did not exit the dataset due to tracing problems; unusual: tracings of a type that had not previously been described. (**b**) Example of a CiD identified by back-tracing from a PMN. Arrowheads indicate locations at which this CiD makes synapses with the PMN. Orange spheres dotting the PMN represent other locations at which different CiDs make synapses on this cell. Scale bar: 10 µm. (**c**) As in (c), for a CoBL. (**d**) As in (c), for an RS axon. (**e**) Cumulative distributions of the normalized dorso-ventral soma positions of CiD and CoBL cells. CoBLs are significantly more dorsal, $p = 0.03$ (**f**) As in (e), comparing the soma positions of CiDs identified from the SMN with positions of CiDs identified from the PMN. CiDs identified from the PMN are significantly more

dorsal, p = 0.004. (**g**) As in (e), comparing the dorso-ventral positions of CoBL somata identified from the PMN with those identified from the SMN. There is no significant difference. *This figure is adapted from a manuscript in preparation (Svara et al.).*

Of all the presynaptic tracings (Figure 23a), 151 or 30.5% (SMN: 23 or 25.0%, PMN: 128 or 31.8%) had a soma contained within the dataset. For these tracings, a cell type could be assigned based on morphology. Most of the remaining tracings represented axons of neurons with more distant somata that had been cut off at the dataset boundaries and which could originate either from spinal interneurons or from reticulospinal (RS) command neurons located in the hindbrain. A small number of tracings (total over both motoneurons: 14 or 2.8%, SMN: 3 or 3.3%, PMN: 11 or 2.7%) did not exit the dataset without reaching a soma and must contain reconstruction mistakes or problematic data locations ("unclear" in Figure 23a). Of the longitudinally running axons, some could be identified as RS based on previously published light microscopy based morphological descriptions of RS axons (Gahtan and O'Malley, 2003) (example in Figure 23d). These axons ran in the vlf or dlf tracts and were often myelinated. Since the axonal morphology in the spinal cord has been characterized only for a subset of RS axons, the possibility remains that some of the longitudinal axons found here that were not classified as RS also originate from the hindbrain. There was a large difference in RS contacts between the SMN and PMN, with a total contact number over both motoneurons of 56 or 11.3%, but only 1 or 1.1% on the SMN versus 55 or 13.6% on the PMN. This difference is consistent with the idea that the brain controls large MNs directly during vigorous behaviors that have to be executed with low latency, such as escapes, as shown previously and in this work for the Mauthner axon, but that the main source of excitation to weaker MNs is from spinal interneurons that make up the central pattern generator (CPG), which activates the MN pool during routine swimming.

In fact, many of the neurons with somata in the dataset were found to belong to types previously described to be part of the CPG. The CiD, Commissural Bifurcating Longitudinal (CoBL) and CiA types together account for most of the remaining tracings (136 or 27.5% in total over both motoneurons, 22 or 23.9%

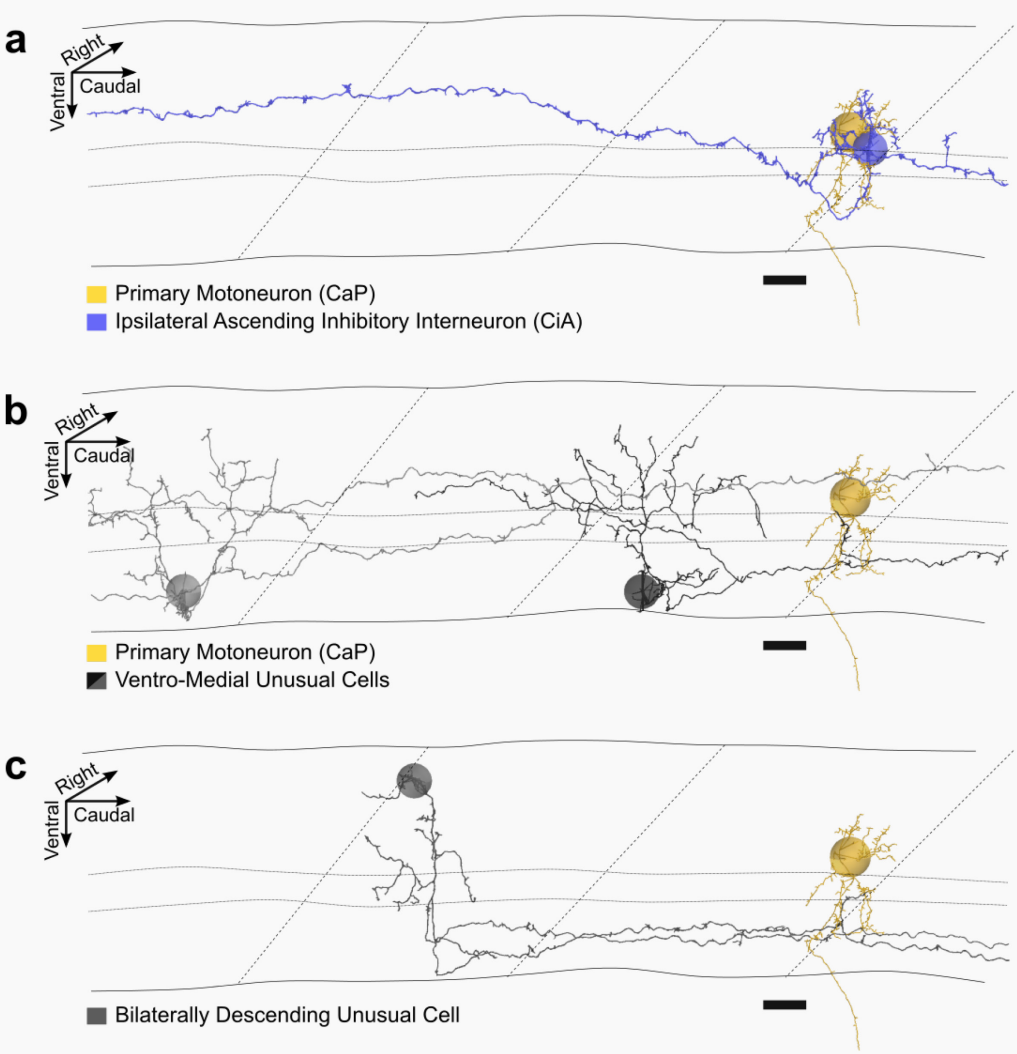

Figure 24 | Examples of less commonly found motoneuron-presynaptic cells. (**a**) A CiA neuron. (**b**) Two examples of a previously undescribed type that has a descending axon ipsilateral to the seed MN, a ventrally and medially located soma and a dendritic tree on the contralateral side. (**c**) A previously undescribed cell with two descending axons, one on each side of the spinal cord. Scale bars: 10 µm. *This figure is adapted from a manuscript in preparation (Svara et al.).*

for the SMN, 114 or 28.3% for the PMN) and are three typical components of the CPG: The CiDs generate motor bursts by rhythmically exciting the ipsilateral side, the CoBLs ensure left-right alternation by inhibiting the contralateral side and the CiA are involved in ipsilateral burst termination and rostro-caudal propagation of activity by inhibiting the ipsilateral side rostrally. Of these, the CiAs were the rarest (13 or 2.6% over both neurons, 5 or 5.4% for

the SMN, 8 or 2.0% for the PMN) (example in Figure 24a). This likely reflects a bias in the reconstruction strategy: Since the two MNs were located in the more caudal one of the two fully contained segments and since CiA cells have primarily ascending axons, most of the CiA cells contacting the reconstructed MN pool would be expected to lie in the caudally adjoining, partially contained segment or even further caudal, limiting the possibility to detect them in this analysis. In contrast, CiDs have primarily descending axons and so should be more readily identified when tracing the presynaptic partners from a caudally located MN. In total, 47 or 9.5% CiD contacts were found (SMN: 7 or 7.6%, PMN: 40 or 9.9%), which corresponded to 27 distinct cells, each making on average 1.7 synapses with the two selected MNs (example in Figure 23b). Since CiDs located at different dorso-ventral positions have been shown to be recruited differentially during different swim speeds, the dorso-ventral location of CiD somata identified from the two different types of MNs was compared. Indeed, CiDs identified from the PMN were significantly more dorsal than CiDs identified from the SMN (Figure 23f, $p = 0.004$, mean dorso-ventral position for CiDs identified from SMN: 0.55 ± 0.08, from PMN: 0.70 ± 0.14). A total of 76 or 15.4% (SMN: 10 or 10.9%, PMN: 66 or 16.5%) of contacts were from CoBLs, which have bifurcating axons that both descend and ascend. They were made by 36 distinct neurons (example Figure 23c). These cells were significantly more dorsal than the CiDs (Figure 23e, normalized dorso-ventral position for CoBLs: 0.73 ± 0.07, for CiDs: 0.67 ± 0.14, $p = 0.03$). However, there was no significant difference in the dorso-ventral soma position of CoBLs detected by starting from the SMN and CoBLs detected by starting from the PMN (Figure 23g, from SMN: 0.74 ± 0.02, from PMN: 0.73 ± 0.08, $p = 0.41$).

Several other types of cells were identified in addition to these CPG components, but were less abundant. Four synaptic contacts (0.8%) onto the PMN were from Commissural Local (CoLo) interneurons. As described above in the context of the Mauthner network, this connection underlies the suppression of contralateral activity when one side of the tail executes a Mauthner induced C-bend. Synapses of this type were not found to contact the SMN, reflecting the role of this interneuron in a highly specific, forceful behavior. Three synaptic contacts onto the PMN (0.6%) were found to be with

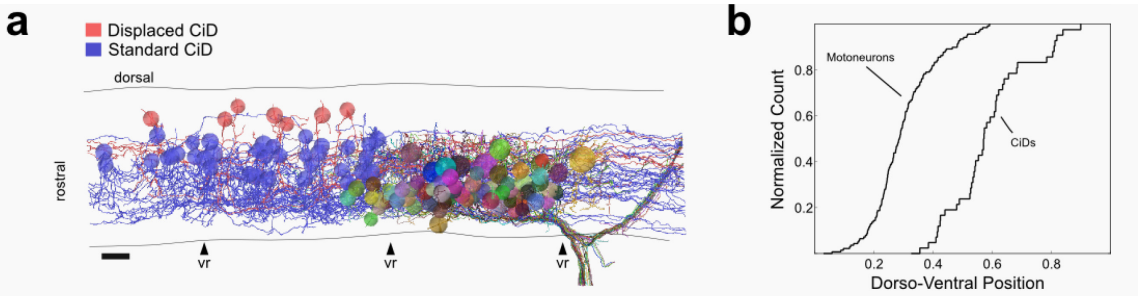

Figure 25 | Comprehensive identification of CiD interneurons. (**a**) CiDs located rostrally from the reconstructed MNs, together with the MNs. Note the difference in dorso-ventral location between CiDs and MNs. The categorization into displaced and standard CiDs is performed based on dorso-ventral position, as described below. vr: ventral root locations. Scale bar: 10 µm. (**b**) Normalized cumulative distribution of normalized dorso-ventral CiD soma positions. *This figure is adapted from a manuscript in preparation (Svara et al.).*

Unipolar Commissural Descending (UCoD) interneurons, a functionally poorly characterized type of interneuron.

Exactly one contact onto the PMN was found to be from a Commissural Primary Ascending (CoPA) interneuron, an interneuron type involved in a propriospinal reflex arc mediated by Rohon-Beard (RB) sensory neurons, which excite CoPAs upon tactile stimulation of the tail and are thought to be homologous to the dorsolateral commissural (dlc) interneuron in hatchling *Xenopus* (Knogler and Drapeau, 2014). These are known to monosynaptically excite contralateral MNs (Li et al., 2003), consistent with the finding of a direct synaptic contact here. Another synapse onto the PMN was found to be from a CoSA. The morphologically defined CoSA type is known to consist of a glutamatergic and a glycinergic subtype (Higashijima et al., 2004b), making the interpretation of this connection unclear, especially since the glycinergic subtype is known to be involved in a range of different swim behaviors, such as escapes, struggling and routine swimming (Liao and Fetcho, 2008).

Finally, 5 synapses (1.2%) onto the PMN were made by cells that did not fit any of the previously published descriptions of spinal interneurons. Three of these were made from two distinct interneurons which had medially located, ventral somata, with extensive dendritic arbors on one side of the spinal cord and a

descending axon on the other (Figure 24b). The other two synapses were made by a cell that had a dorsally located soma, with an axon that first coursed ventrally and branched, sending one branch down each side of the spinal cord (Figure 24c).

Comprehensive Identification of CiD Interneurons

The reconstruction of the presynaptic partners of two MNs of different type had revealed a differential innervation of these cells. In particular, the analysis suggested that dorso-ventrally separated subsets of CiD interneurons contacted different MNs (Figure 23f). Since the overall goal of the spinal cord reconstructions was to obtain a detailed, mechanistic understanding of orderly MN recruitment by CiDs, a comprehensive and unbiased approach to detecting CiDs and reconstructing their connectivity to the entire MN pool was taken. This was done since the above analysis did not necessarily uncover all CiD interneurons present in the dataset and since the two specific MNs chosen as starting points might have biased the analysis towards subsets of CiDs.

Thus, a seed point for tracing was placed in every rostrally located soma on the left side of the spinal cord. The analysis was restricted to the rostral region, since CiDs are primarily descending. Since a complete tracing of all rostrally located spinal neurons would have been prohibitively time-consuming, annotators were given a set of simple instructions allowing them to cancel tracings early if they clearly did not represent a CiD. That is, they were asked to stop tracing and go to the next seed soma as soon as 1) the axon crossed to the contralateral side, 2) the axon exited the spinal cord through a ventral root or 3) the cell was a glia. To make sure that the first two rules could be applied as quickly as possible, annotators were instructed to always follow more ventrally pointing branches first at branch points and at somata. In total, annotators started tracing from 597 rostrally located somata. Of these, 73% were canceled early due to one of the above rules. All remaining tracings that had a primary descending axon were CiDs, of which there were 42 or 7% (Figure 25a). CiD somata spanned the dorso-ventral range of 0.36 – 0.90 with a mean position of 0.61 (Figure 25b**).**

CiD-to-Motoneuron Connectivity

To test the different wiring models (Figure 9) that may underlie the orderly recruitment of MNs by the rhythmically active CiD interneurons, the connectivity between the CiDs and MNs was reconstructed. This was done by automatically generating lists of proximity locations between CiDs and MNs and asking annotators to manually inspect each location and decide whether an actual synaptic contact was present or not (see Methods). At locations that were deemed true synapses, the synaptic contact area was measured as a proxy for synaptic strength. The average number of synapses made onto the MN pool per CiD was 6.71 ± 6.12 s.d. with an average of 1.44 ± 0.79 s.d. synapses per connected CiD / MN pair and an average aggregate synaptic contact area of 0.43 µm² with a standard deviation of 0.46 µm².

This allowed a wiring matrix to be compiled and to identify CiDs that wired selectively to subsets of MNs. Some CiDs preferred large, dorsal MNs (example in Figure 26a), while others were less specific (example in Figure 26b). When the complete wiring matrix was plotted with CiDs sorted by dorso-ventral position and MNs sorted by size (Figure 26e, 27), a pattern became apparent whereby the 7 most dorsal CiDs, separated by a gap in dorso-ventral position from the other CIDs, in the dorso-ventral range of 0.75 - 0.9, specifically made large synapses onto large MNs, i.e. PMNs and B-SMNs. The more ventral CiDs presented a mixed picture, where some (9 / 31) did not display any selectivity for MNs of a particular size and contacted both large and small MNs. However, some cells appeared to contact mostly smaller MNs (17 / 31) and others yet (5 / 31) appeared to be specific to larger MNs (compare Figure 27a). Yet, when the population of CiDs with a dorso-ventral position of less than 0.75 was split into a dorsal and a ventral half, no significant difference in MN size preference was apparent between the two halves (Figure 27b). This lack of dorso-ventral separation implies that the CiDs that preferred smaller MNs and the CiDs that were unspecific are recruited together in a common

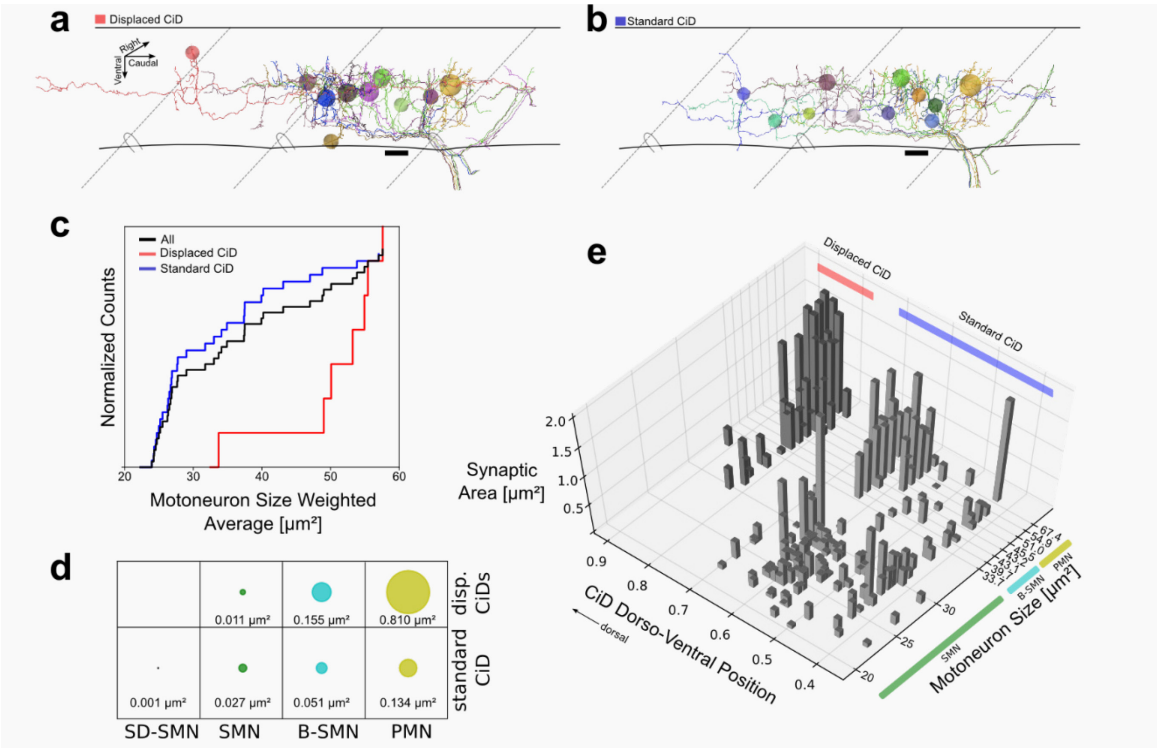

Figure 26 | Comprehensive reconstruction of connectivity between CiDs and MNs. (**a**) Example of a dorsally located CiD that contacts large MNs specifically. Scale bar: 10 µm. (**b**) Example of a more ventrally located CiD that contacts MNs of different sizes non-specifically. Scale bar: 10 µm. (**c**) Cumulative distributions of MN sizes contacted by different CiDs, weighted by synaptic contact area. Dorsal, displaced CiDs are specific to large MNs. (**d**) Summarized wiring matrix from different types of CiDs to different types of MNs. Dorsal, displaced CiDs strongly contact large MNs. Reported areas are summed synaptic contact areas normalized to the number of MNs and CiDs in each class. (**e**) Complete wiring matrix of CiDs, sorted by their normalized dorso-ventral soma positions, to MNs, sorted by their soma sizes. Dorsal, displaced CiD strongly prefer large MNs and have large aggregate synaptic areas contacting them. Color labels for MNs correspond to colors in Figure 19. See also Figure 27 for a different presentation of the same wiring matrix data. *This figure is adapted from a manuscript in preparation (Svara et al.).*

swim frequency range (McLean et al., 2008). Those cells are therefore collectively referred to as standard CiDs. By the nomenclature introduced in (McLean et al., 2008), these would correspond to the D-CiD and V-CiD populations and the CiDs with a dorso-ventral position of > 0.75 would

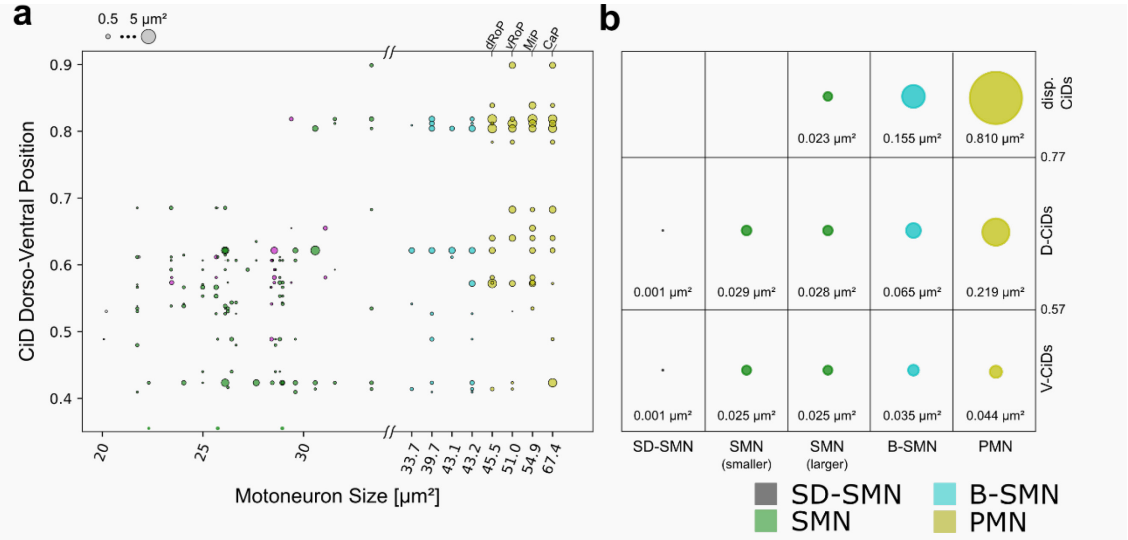

Figure 27 | Wiring from CiDs to MNs. (**a**) Wiring matrix with CiDs sorted by normalized dorso-ventral soma position and MNs sorted by size. Note that the x-axis is not linear for the large MNs (≥ 33.7 µm²), but that large MNs are evenly spaced for clarity. Dorsal, displaced CiDs strongly prefer large MNs. (**b**) Same data as in (a), but summarized by CiD and MN type and averaged over CiDs and MNs. Note little separation between the dorsal and ventral half of the standard CiDs (D-CiDs and V-CiDs). *This figure is adapted from a manuscript in preparation (Svara et al.).*

correspond to the dorsally displaced CiDs (McLean et al., 2008). The MN size specificity for the CiDs was quantified by taking the average size of postsynaptic MNs, weighted by the synaptic contact area, for every CiD (Figure 26c). Standard CiDs and displaced CiDs had significantly different weighted MN size averages ($p = 0.0019$). The overall CiD-to-MN connectivity was summarized by plotting the average synaptic size between CiDs and MNs of different types (Figure 26d, 27b). This enabled an approximate permutation test for the significance of the difference in the ratios of the synaptic size onto PMNs to the synaptic size onto SMNs between displaced CiDs and standard CiDs, which was highly significant ($p = 0.0036$, see Methods for details). In contrast, the difference in that ratio between the dorsal and ventral halves of the standard CiDs was not significant ($p = 0.144$).

Importantly, when the locations of the displaced CiD axons were compared to the locations of the SMNs (Figure 28a) and when the standard CiD axons were

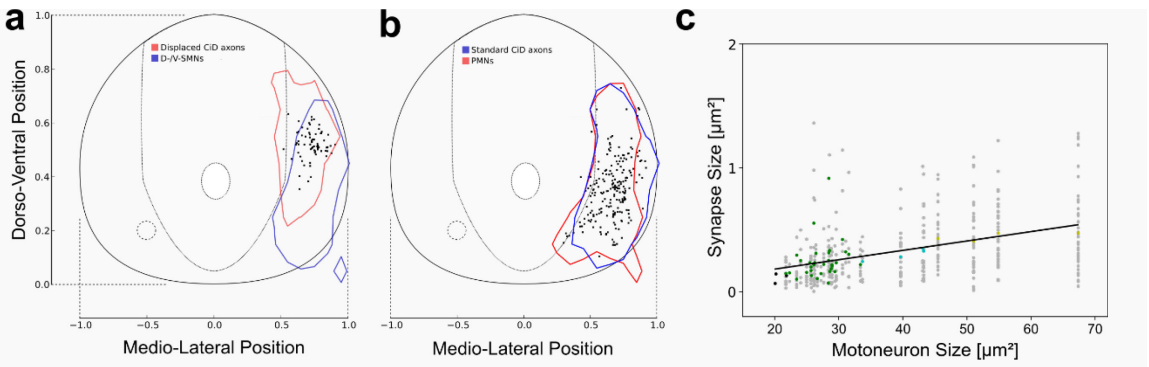

Figure 28 | Locations and sizes of CiD synapses. (**a**) Contours of displaced CiD axon densities (red) and D-/V-SMN densities (blue) Contour lines represent 10 % of peak density. Black dots indicate synaptic locations. Note considerable overlap, in particular in the region in which synapses are made. (**b**) As in (a), for standard CiD axons and PMNs. (**c**) CiD synapse sizes (contact areas) versus MN sizes. Individual synapses are plotted in grey, the averages per MN are colored as in Figure 19. Note linear correlation, r = 0.48, p = 0.02. *This figure is adapted from a manuscript in preparation (Svara et al.).*

compared to the locations of the PMNs (Figure 28b), a considerable overlap was found in both cases. This indicates that the highly specific displaced CiD axons are placed so that they could contact SMNs, yet they choose specifically the B-SMNs and PMNs as synaptic partners.

To test whether the strong connections from displaced CiDs to PMNs were the consequence of having many synapses or of having large synapses, we compared the number of synapses made by displaced CiDs and standard CiDs. Both types of CiDs made a similar number of synapses onto the MN pool per axon (displaced CiDs: 9.0 ± 8.7 s.d, standard CiDs: 7.1 ± 5.1 s.d., p = 0.62, not significant), implying that the high aggregate synaptic contact area onto large MNs is partly explained by the convergence of displaced CiD axons on a small number of selected postsynaptic MNs. Additionally, displaced CiD synapses were significantly larger than standard CiD synapses (standard CiD: 0.30 µm² ± 0.26 s.d, displaced CiD: 0.41 µm² ± 0.25 s.d, p = 0.002). Finally, when the average CiD synapse size was plotted against MN size (Figure 28c), a linear dependence became apparent (r = 0.48, p = 0.02).

The CiD-to-MN connectivity found here displays important properties of two different hypothetical wiring models described earlier: Standard CiDs have little selectivity for MNs of a specific size, which is reminiscent of the model originally proposed by Henneman (Figure 9a). In a swim regime where only standard CiDs are active, orderly MN recruitment would therefore rely on biophysical properties of the postsynaptic MNs. In contrast, displaced CiDs, which are recruited during vigorous swimming, are highly specific to large MNs, as in a labeled line model (Figure 9c).

Acquisition of a Whole Brain SBEM Dataset

The spinal cord dataset acquired here is relatively small, compared to the total size of the animal's nervous system – the entire spinal cord is made up of over 30 segments. This means that long-range connections cannot be resolved. By taking datasets that cover a larger volume of the nervous system, progressively larger-scale and higher-level connectivity can be reconstructed. The gold standard in this endeavor would be, of course, the acquisition and reconstruction of datasets spanning a complete brain or nervous system, ensuring that any circuit of interest will be completely contained. This goal has been difficult to reach in many cases, since imaging the large volume of a complete brain at the high spatial resolution required to identify individual synaptic contacts means that a large number of voxels will have to be acquired and that the total experiment duration will be high. In fact, no vertebrate brain has been completely imaged to date at a resolution allowing neural circuits to be reconstructed. One of the smallest vertebrate brains, that of the larval zebrafish, would have taken more than 7 months to acquire if that experiment had been attempted using the same setup as was used here for the acquisition of the spinal cord dataset (Figure 2).

In this second part of the thesis, the aim was to implement a series of improvements, specifically adaptive tile patterning and line-scanning, for SBEM allowing the acquisition of the first volume EM dataset covering a complete vertebrate brain at a resolution suitable for neural circuit reconstruction within a feasible time-frame.

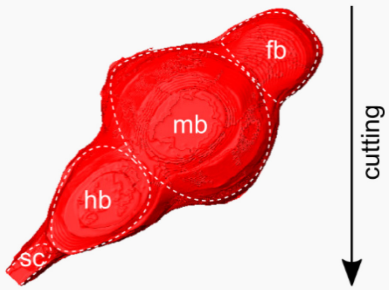

Figure 29 | Cutting orientation of the whole-brain sample. fb: forebrain; mb: midbrain; hb: hindbrain; sc: spinal cord.

The long-range projections that could be resolved in such a dataset, such as those that connect distinct brain areas, are important in many behaviors. For example, the opto-kinetic response (OKR) requires multiple sensory areas and motor areas of the brain to work together. A collaborative project based on the functional characterization of neurons in the pretectum during the OKR (Kubo et al., 2014) was established, in which Dr. F. Kubo (Baier lab, Max Planck Institute of Neurobiology, Martinsried) performed a two-photon calcium imaging based functional characterization of pretectal cell types, and the SBEM improvements developed and implemented by me would be used to acquire a whole-brain stack of one of the fish previously imaged by Dr. Kubo. The pretectum contains cells that respond to gratings moving in different directions. Some of these cells, the simple cells, appear to inherit their activity directly from direction selective (DS) retinal ganglion cells (RGCs). Others, the complex cells, have response patterns that might be explained by combinations of simple cell response patterns. (Kubo et al., 2014) Some of these combinations, such as cells that respond when both eyes see forward motion, but not when just one eye does, can be achieved by feed-forward excitation with summation and thresholding. Others would additionally require inhibition, such as cells that respond only when one eye sees forward motion, but not when both eyes do. The aim of this collaboration was to identify the neural networks that underlie these combinations of complex response patterns from more simple ones. Since the pretectum contains thousands of neurons, many of which are not active during the OKR, the functional characterization was essential to target subsequent reconstruction efforts.

It was decided to fix, stain and embed a complete fish instead of just the head or brain and target the imaging to just the areas of interest in the sample, in order to minimize any dissection related damage to the sample. A special

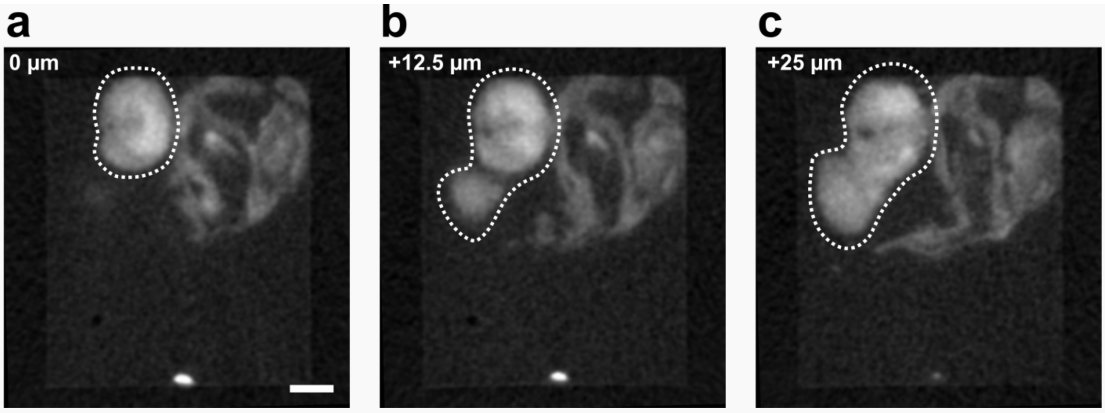

Figure 30 | Changing shape of the tissue of interest over the acquisition run. (**a**) Virtual section of X-Ray microCT data of a plastic embedded whole-brain sample, at the level of the telencephalon, oriented and sliced as it would be in SBEM. (**b**) and (**c**) Sections of the microCT data deeper within the sample. Slices are spaced by 12.5 µm or 500 sections, corresponding to approximately 1 day of SBEM acquisition. The dotted line indicates the boundary of the brain. Other X-ray dense material next to the brain corresponds to the jaw and gills. Note the considerable changes in brain shape within one acquisition day, the disconnected part of the brain in (b) and the difficulty in distinguishing the brain from the rest of the head just based on pixel intensity. Scale bar: 100 µm.

orientation of the sample was chosen: The cutting plane was rotated 35° in yaw from the transversal plane (Figure 29). This cutting plane was chosen so that bilaterally symmetric axon tracts were usually cut in different angles, allowing a subsequent evaluation of whether the dataset's anisotropic resolution influenced traceability.

Dynamic Tile Patterning

Previous SBEM datasets were acquired with static, rectangular tile patterns, which is often sufficient when small parts of larger brain regions are imaged. Complete brains, however, have irregular shapes, making it wasteful to scan the entire bounding box. Based on a 3-dimensional reconstruction of the shape of the 5 dpf larval zebrafish brain from an optical overview dataset, it was found that, in the orientation described above, only 42% of the bounding box volume would contain brain tissue (Figure 29). Ideally, the tile pattern would be adapted on every slice to match the 3-dimensional sample geometry. Techniques for

achieving this must be able to deal with several complicating factors (Figure 30). In particular, 1) the location of the outline can change by more than 100 µm within 24 h, 2) parts of the brain can be disconnected within a slice and 3) when just the brain is to be imaged within a larger sample containing the entire head, the surrounding tissue must be distinguished from the region of interest.

For these reasons, several techniques for adapting the tile pattern that were initially considered could not be applied. Manually contouring the region of interest in regular intervals would have required very short intervals to be efficient. Propagating manually drawn contours from one slice to the next would not have been compatible with disconnected brain areas appearing during cutting. Automatically generating contours based on the image contents would have required a highly reliable algorithm for distinguishing brain tissue from the rest of the head. Therefore, it was decided to decouple contour generation from SBEM acquisition by manually defining the regions of interest (ROIs) on a separately acquired X-Ray microCT stack of the sample (see Methods, p. 38).

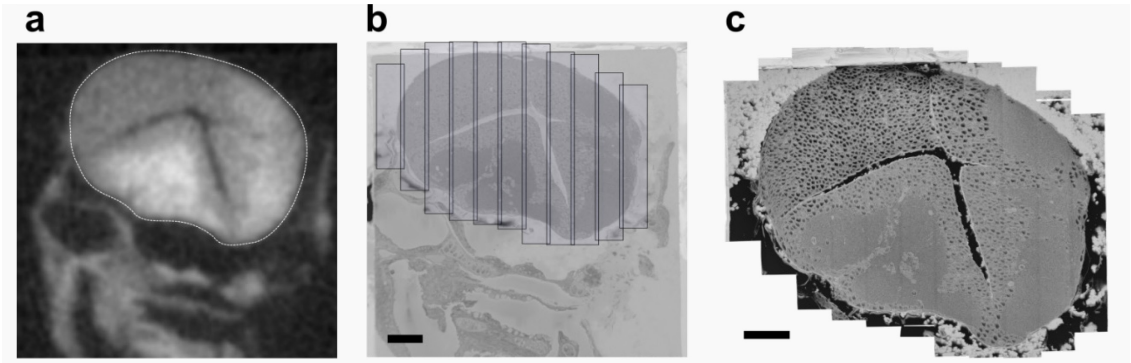

Figure 31 | Generation of SBEM tile patterns from a X-ray microCT scan of a SBEM sample. (**a**) Virtual slice of X-ray microCT data from an embedded brain sample ready for SBEM imaging. Dotted line indicates manually defined region of interest (ROI). (**b**) Low-resolution EM image of the same sample, in the same slice plane. The positions of the overlapping stripes tiling the brain represent the microtome motor positions and scan lengths of SBEM mosaic tiles, pre-computed from the X-ray based ROI. Scale bar: 50 µm (**c**) High-resolution multi-tile SBEM slice composed of the 11 tiles acquired at the positions shown in (b). Scale bar: 50 µm.

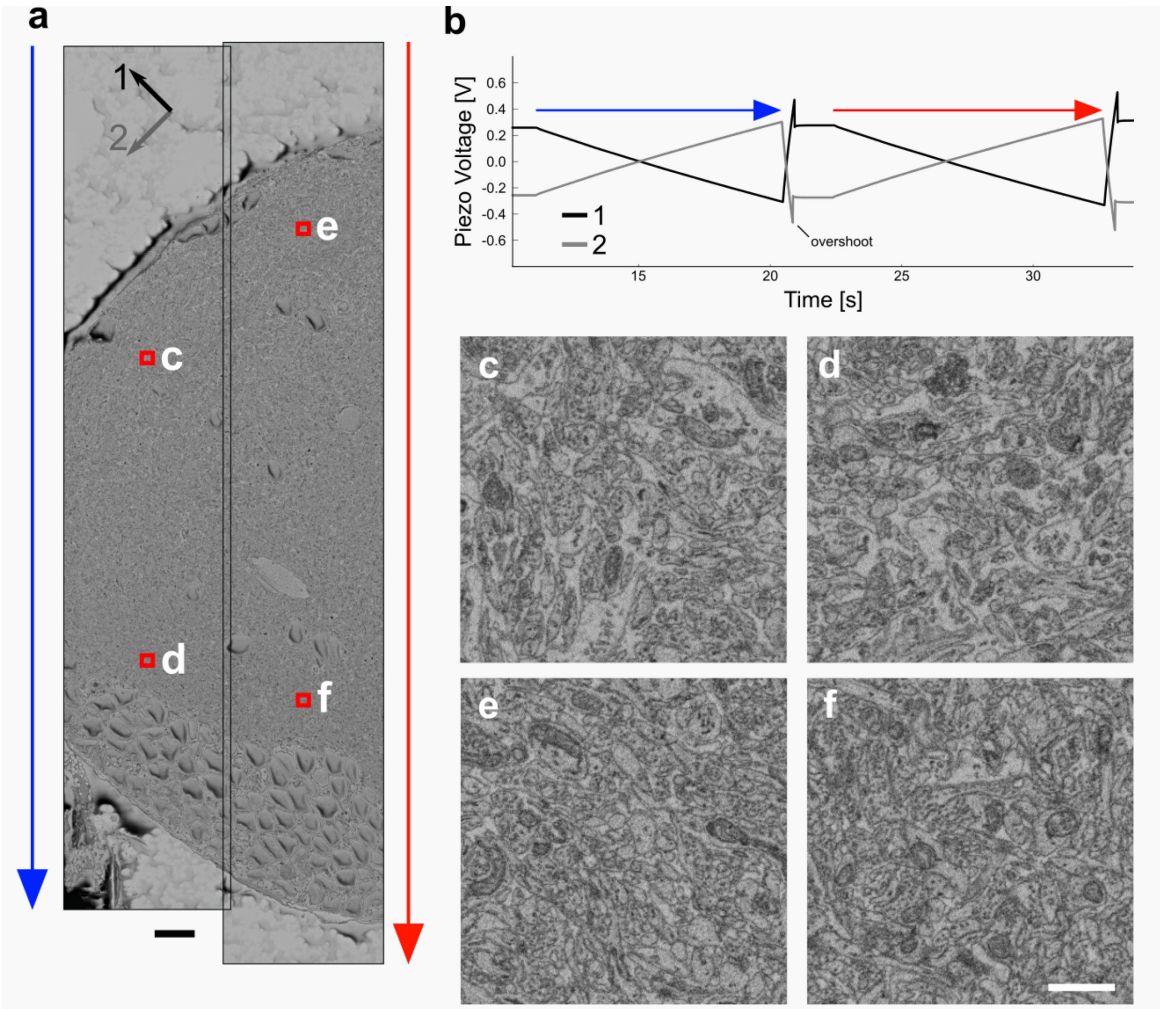

Figure 32 | Line-scanning of stripe-shaped image tiles. (**a**) Overlapping line-scanned tiles of 14665 px and 16061 px length and constant 3000 px width. Arrows labeled 1 and 2 correspond to the stage motor orientations, driven by the voltages shown in (b). Colored arrows represent the stage-scan for the two tiles, corresponding to the arrows in (b). Scale bar: 10 µm. (**b**) Trace of the voltages driving the stage motors for the scans shown in (a). The voltages overshoot the start positions for the next tile to avoid piezo creep. (**c**), (**d**), (**e**), (**f**) Full-resolution data examples from different locations within the line-scan. Scale bar: 1 µm.

Both the X-Ray microCT data and the SBEM microtome motors were precisely calibrated, allowing SBEM motor positions to be pre-computed from the X-Ray data. SBEM dataset acquisition could then proceed unattended, scanning only at the tile locations defined ahead of time (Figure 31) and targeting only the 42% of the bounding box that were actually of interest.

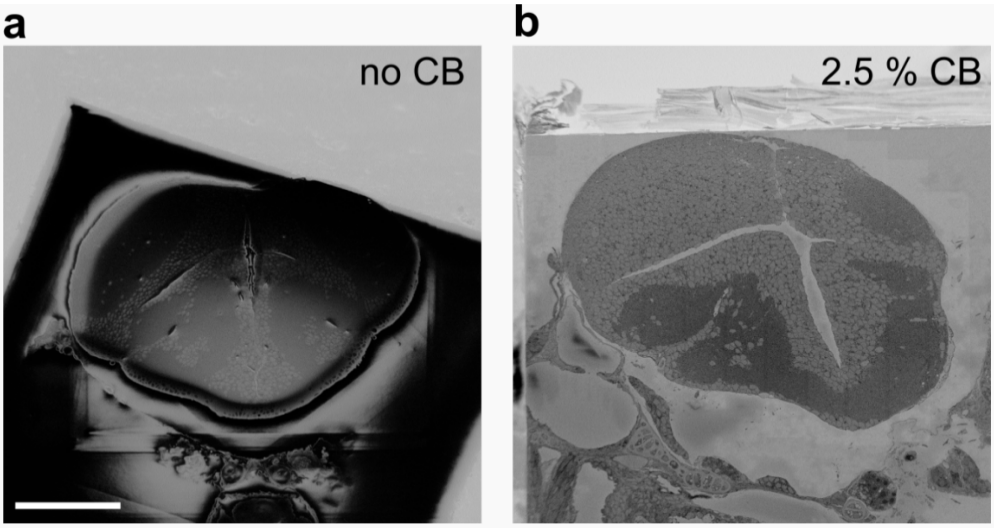

Figure 33 | Avoiding charging artifacts in high vacuum SEM imaging. (**a**) A whole-brain sample embedded in standard, non-conductive plastic, sectioned at the level of the tectum. Note the intense dark appearance of the plastic and parts of the brain, a typical charging artifact. (**b**) Brain sample embedded in plastic containing 2.5% Carbon Black, but otherwise identically prepared and imaged with identical parameters. Note dramatic reduction in charging artifacts. CB: Carbon Black. Scale bar: 100 µm.

Line-scanning

In multi-tile SBEM, stage motor moves between tiles can make up a considerable part of the total imaging time (Figure 2). The total number of stage moves required depends on the size of the individual tiles. Since the tile size is mainly limited by imaging aberrations that occur when the primary electron beam is deflected far off-center, a way of increasing the tile size is to scan only one of the image axes using the microscope's electromagnetic scan coils and to scan the other axis by moving the sample. This method is referred to here as line-scanning.

On the experimental setup used for these experiments, a combined movement and settling time of 3 s was found to be necessary for all movement induced stage vibrations to dampen sufficiently to allow the next tile to be imaged. The maximal tile size that could be taken without line-scanning without unacceptable distortions at the edges and corners was found to be 42 µm x 42

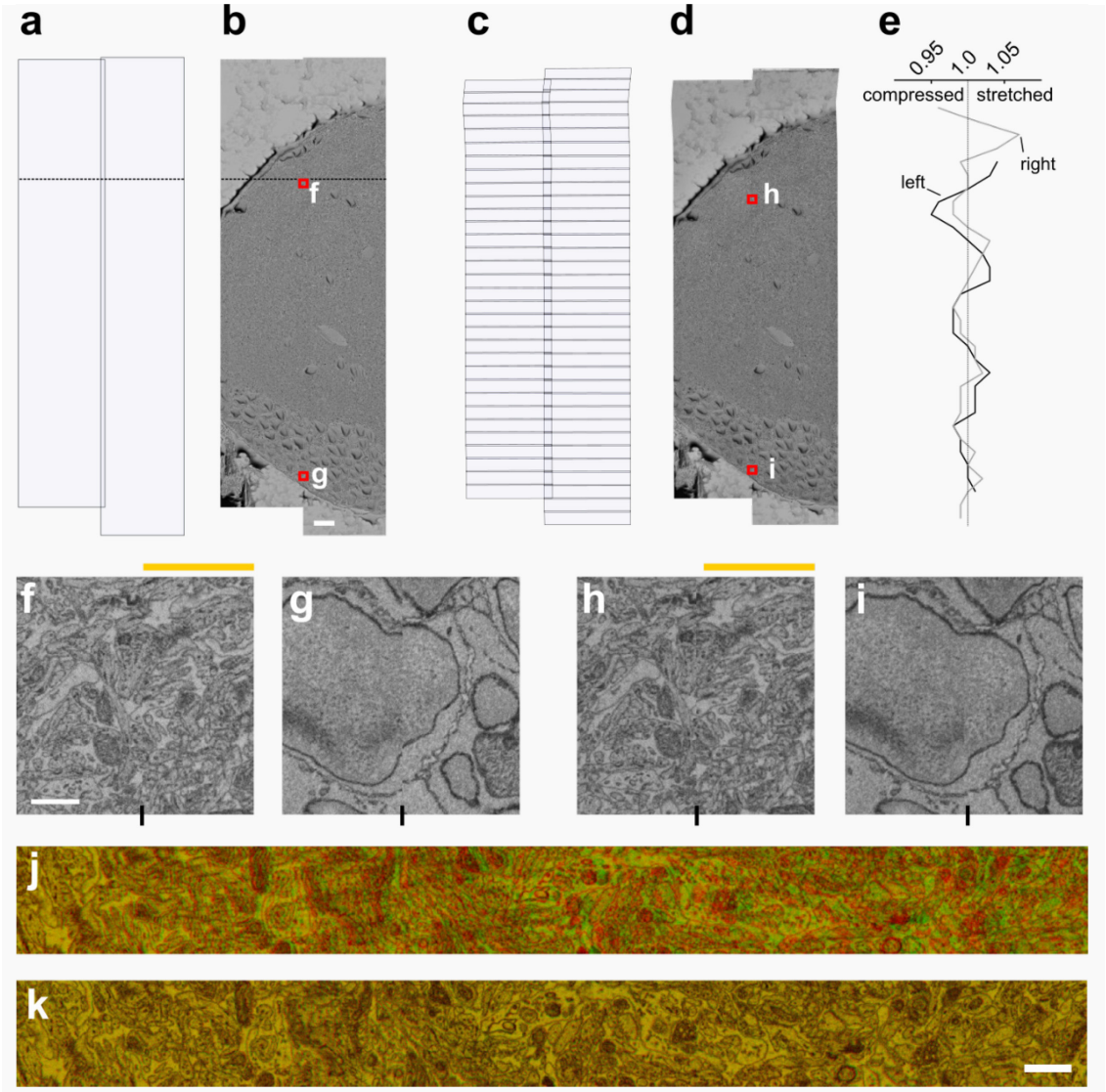

Figure 34 | Registration of a line-scanned multi-tile SBEM dataset. (**a**) Two neighboring line-scanned tile outlines, registered by translation at the level of the dotted line. (**b**) Registered image data corresponding to (a). Scale bar: 10 µm. (**c**) The same tiles as in (a) and (b), cut into overlapping 500 px pieces along the long axis and registered using affine transformations applied to every piece. (**d**) Image data corresponding to (c). Scale as in (b). (**e**) Stretching and compression factors of the tile pieces in (c) and (d). Note the non-trivial dependence of the stretch factor on the y-position. (**f**), (**g**) High resolution examples from the data aligned by translation at the locations indicated in (b). The yellow label indicates the region in which both tiles overlap, the black mark indicates the seam location. Note how the alignment is good at the seam locations close to the matched position (dotted line in (a) and (b)), but gets worse at a larger distance from that position. Scale bar: 1 µm. (**h**), (**i**) As (f) and (g), for the data aligned by piece-wise affine

registration shown in (d). Note the absence of any obvious shifts in the data at the seam. Scale as in (f). (**j**) Red / green overlay of the overlap region of the translation registered data. Matched position is at the left edge of the panel. Note how the match become progressively worse with the distance from that location. Scale as in (k). (**k**) As (j), for piece-wise affine registered data. Note good match over the entire length of the panel. Scale bar: 1 µm.

µm, corresponding to an image size of 9 megapixels (MPx) at an imaging resolution of 14 nm x 14 nm. At those parameters, the total SBEM acquisition time for the larval zebrafish brain with adaptive tiling would be 92.8 days, of which 48.3 days or 52% would be spent moving the stage motor between tiles (Figure 2).

If the field of view (FOV) limitations were completely eliminated along one of the axes, the zebrafish brain could be covered with a series of stripe-shaped tiles (as shown in Figure 31), with an average tile size of 49 MPx. At this size, the total acquisition time for the brain would be reduced to 52.5 days, of which 8.1 days or 15% would be spent on the stage movements between the tiles. That is, the total acquisition time for the brain would be reduced to just 57% of the total acquisition time without line-scanning.

Line-scanning was therefore implemented by equipping the SBEM microtome stage with piezo actuators that allowed a smooth and precise movement of the stage. Prof. Dr. W. Denk designed the mechanics of the system, which was built by the mechanical workshop at the Max Planck Institute for Medical Research, Heidelberg. I developed the software driving the system. The system made it possible to scan stripe-shaped tiles up to 32768 pixels in length, corresponding to 459 µm at a pixel size of 14 nm (Figure 32a), without any visible image aberrations along the length of the stripes (Figure 32c, d, e, f). Importantly, piezos are affected by hysteresis and creep, where creep means that piezos continue moving slowly in their last movement direction even though the voltage applied does not change. Therefore, the piezos could not be driven simply with a linear voltage, but were driven by a voltage transformed using a dynamic model of the piezo behavior developed by Prof. Dr. W. Denk. Additionally, to reduce creep, rapid piezo movements between the initial tile

positions were designed to overshoot and dash back by an empirically determined fraction (20%) of the travel distance (Figure 32b).

Sample Discharging

When performing SBEM in high vacuum, the densely heavy metal stained and conductive sample is usually grounded by cutting into it and coating its sides with gold, since charge build-up otherwise causes artifacts that compromise image quality (Figure 33a). When a complete brain is to be imaged, this approach can't be used, since cutting into the sample means destroying a part of the tissue of interest. Additionally, any margin left next to the brain, where bulk plastic would be included in an image, would cause local charging artifacts, even if the sample itself was grounded. This was avoided by dispersing 2.5% Carbon Black particles in the bulk plastic, rendering it conductive and non-transparent (Figure 12), which allowed high-vacuum imaging without any damage to the sample (Figure 33b).

Registration

Tiles in a SBEM multi-tile mosaic must be aligned (registered) to their neighbors within a slice and across slices. Line-scanned tiles present an additional challenge in registration, since the two image axes are not scanned using the same physical method.

This can be seen when attempting to register two neighboring line-scanned tiles. When they are translated relative to each other so that they match perfectly at a given y position, the match gets worse with the distance from that position (Figure 34a, b, f, g, j). This problem was solved by cutting the large stripe tiles into pieces of 500 pixels in length, with 50 pixels overlap, along the y axis (Figure 34c, d). Each of these pieces was then registered to its neighbors using an affine transformation using the alignment software package provided by Bill Karsh at Janelia Farm (Scheffer et al., 2013) (Figure 34d, e), which produced a satisfactory registration over the entire length of the stripes (Figure 34h, i, k).

Whole-Brain Acquisition

With both adaptive tiling and line-scanning having been established, the expected total acquisition time for a whole larval zebrafish brain was 52.5 days

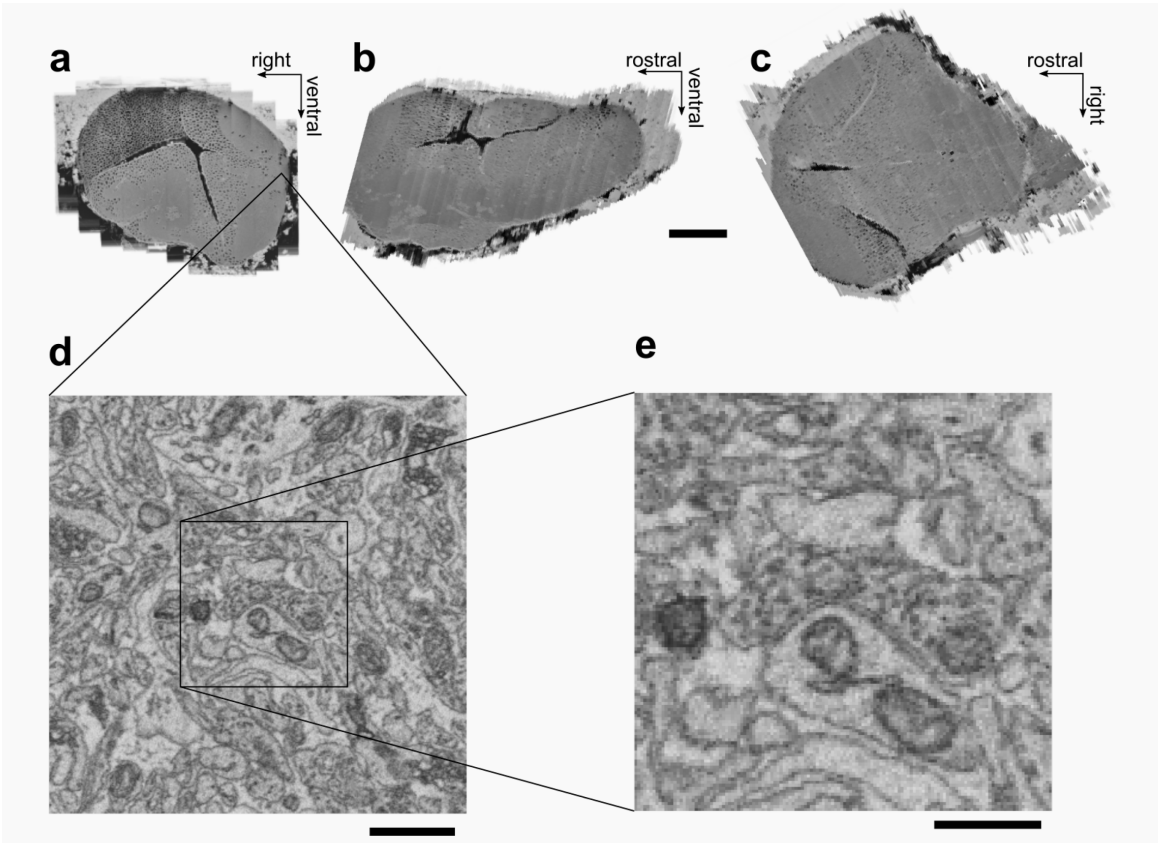

Figure 35 | Larval zebrafish whole-brain stack. (**a**) Zoomed-out, transverse slice from the whole-brain dataset, at the level of the tectum. (**b**) Parasagittal view. (**c**) Coronal view. Scale bar: 100 µm. (**d**) Close-up of the pretectal neuropil, showing a tissue densely packed with small neurites and numerous putative synapses. Scale-bar: 1 µm. (**e**) Full-resolution view of the pretectal neuropil, showing a synaptic contact. Scale bar: 500 nm.

(Figure 2), a realistic time frame for a SBEM experiment. To avoid loss of detector sensitivity over the duration of the experiment, data acquisition was interrupted once per week for hydrocarbon deposit removal using a downstream asher.

A 5 dpf elalv3:GCaMP5G fish was imaged by Dr. F. Kubo to identify subsets of pretectal cells that were active during specific types of whole-field motion. Then, I prepared the fish by chemical fixation, staining and plastic embedding and performed SBEM imaging. The SBEM dataset consisted of 28592 slices, corresponding to a cutting travel of 714.8 µm, and a total of 264173 individual tiles. It was acquired over the course of 59.6 days, not including 23.4 days of unexpected downtime that was necessary for servicing the microscope by the

microscope vendor's technicians, and was 14.2 TB in size. This duration was slightly higher than the prediction mentioned above, due to tile-tile overlap overhead and downstream asher runs, which were not included in the calculation.

The data covered the entire brain from the olfactory bulbs to the spinal cord / hindbrain boundary. However, a setup malfunction caused a loss of overlap between neighboring tiles over 755 sections (18.875 µm) between the telencephalon and the midbrain. For this reason, only the 23390 sections caudal from the telencephalon / midbrain boundary were included in the final registration. The data allows both for zooming out to a coarse overview of brain regions (Figure 35a, b, c) and to zoom in and identify individual synaptic contacts (Figure 35d, e).

Correlation of 2-Photon and SBEM Imaging

The two-photon Ca^{2+} imaging experiment performed by Dr. F. Kubo was aimed at identifying pretectal cells with responses to specific types of whole field visual motion (optic flow). Some cells were of a simple type, that is, their response pattern could be explained by assuming that they are driven by input from direction-selective DS-RGCs. However, simple cells of the same response type can be found on both sides of the brain, which implies that, since RGC axons are commissural, an additional commissural cell must relay the RGC output back to the other side. More complex wiring hypotheses can be formulated for the neurons with a complex response type (Kubo et al., 2014).

To enable a direct test of these wiring hypotheses, functionally characterized pretectal cells were identified in the EM dataset. To this end, an affine transformation was applied to a 2-photon overview stack of the pretectum, aligning it with the EM stack. The affine transformation was computed from a set of manually chosen correspondence points between the two stacks, which were chosen at locations that were easily identified in both, such as blood vessels or prominently placed somata. The correspondence point selection was performed by Dr. F. Kubo, using custom software that C. Cascio had specially developed for the task under my supervision. Due to non-linear deformations between the 2-photon and EM datasets, which were likely introduced during

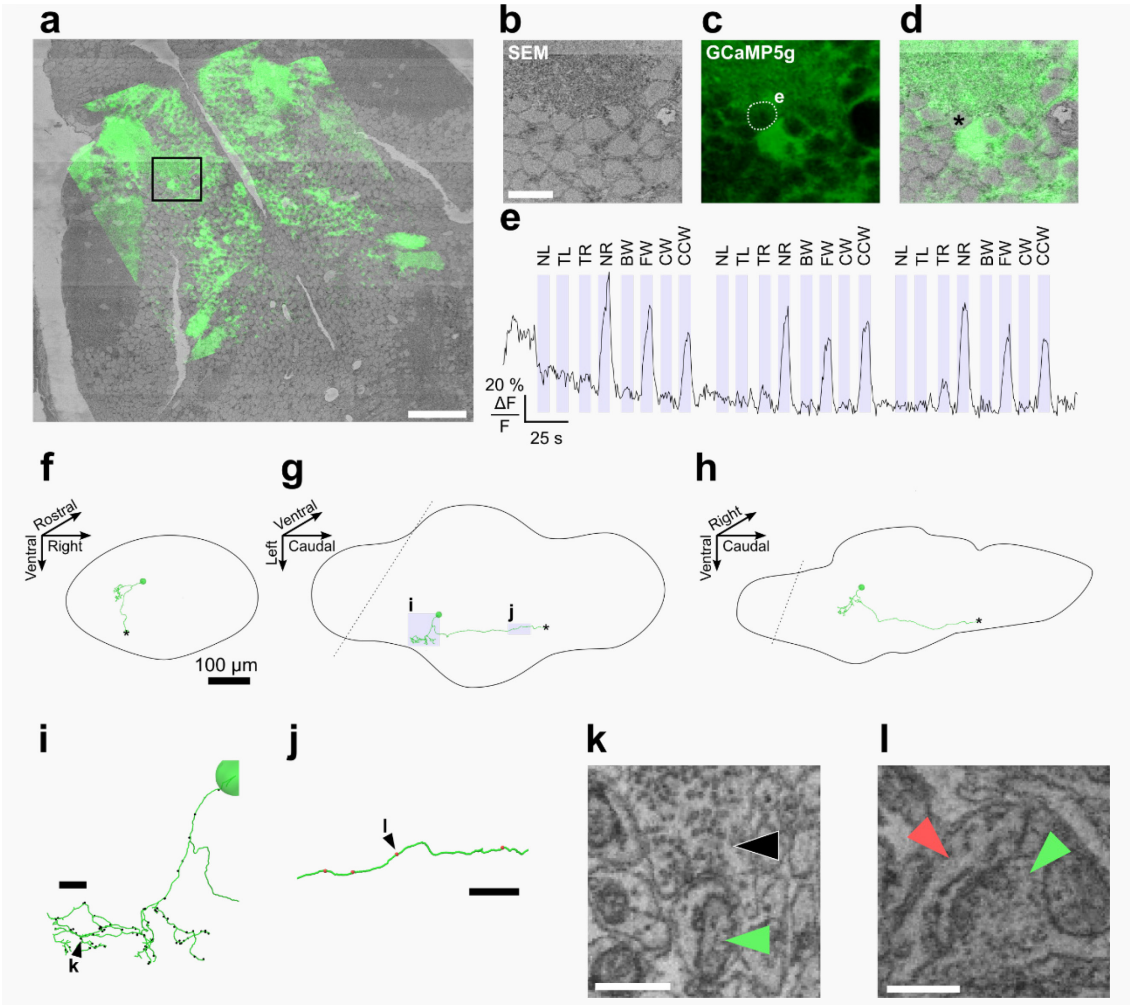

Figure 36 | Registration of the two-photon functional calcium and SBEM datasets. (**a**) Low-resolution overview of the two-photon imaged elavl3:GCaMP5G signal (green) aligned to the SBEM dataset (grey). Scale bar: 50 µm. (**b**) High resolution EM view of the region labeled in (a). Scale bar: 10 µm. (**c**) 2-photon image from the corresponding location. Dotted line labels ROI for calcium trace shown in (e). (**d**) Overlay of (b) and (c). Asterisk labels the soma used as a tracing seed point. (**e**) Time-series of the calcium trace for the ROI contoured in (c), corresponding to the reconstructed cell. The cell shows a calcium response whenever the right eye sees a grating moving in the nasal direction. NL: nasalward, left eye; TL: temporalward, left eye; TR: temporalward, right eye; NR: nasalward, right eye; BW: backward; FW: forward; CW: clockwise; CCW: counter-clockwise. (**f**) Transversal view of a 3-dimensional rendering of the tracing for the cell highlighted in (c) and (d). Scale bar: 100 µm. (**g**) as in (f), coronal view. (**h**) As in (f), sagittal view. (**i**) Close-up of the dendritic tree, corresponding to the region highlighted in (g). Black dots represent synapse

locations. Arrowhead points at synapse shown in (k). Scale bar: 10 µm. (**j**) Close-up of a piece of the axon, corresponding to the region highlighted in (g). Red dots represent synapse locations. Arrowhead points at synapse shown in (l). Scale bar: 10 µm. (**k**) Close up of synapse made onto the dendrite. Black arrowhead: Presynaptic compartment. Green arrowhead: Postsynaptic compartment. Scale bar: 500 nm. (**l**) Close up of a synapse made in the ventral hindbrain by the axon. Red arrowhead: Postsynaptic compartment. Green arrowhead: Presynaptic compartment. Scale bar: 500 nm. *The two-photon data shown here was acquired by Dr. F. Kubo.*

SBEM preparation, correspondence points were only selected from small corresponding areas and not over the entire volume. This allowed a proof of concept identification of individual somata between the two modalities (Figure 36a – d). One of the identified somata was a simple cell responding to monocular stimulation in the right eye in a nasalward direction-selective fashion (Figure 36c – e), located on the left side of the brain, suggesting that it receives direct DS-RGC input. This cell was selected for a test reconstruction. It had a monopolar soma, with a dendritic tree branching from the primary neurite and extending ventrally and laterally and an axon that coursed caudally and ventrally into the hindbrain (Figure 36f – h). The dendritic tree was covered with 86 synapses (Figure 36i, k) and the axon sporadically made a total of 5 synapses in the hindbrain (Figure 36j, l). Importantly, the lateral region, close to the surface of the brain, in which the dendritic tree arborized, was very close to the expected locations of the RGC arborization fields 4 and 5 (Robles et al., 2014), making a direct innervation by RGC axons likely. The other functionally identified cells will now have to be reconstructed to relate their response patterns to the connectivity of the complete circuit.

Discussion

The goal of this thesis was two-fold: First, to acquire a SBEM stack of the larval zebrafish spinal cord using established technology and to reconstruct parts of the network connectivity with the aim of gaining a precise, mechanistic understanding of how the spinal CPG for swimming achieves the orderly, gradual recruitment of MNs of different sizes that underlies the gradation of muscle force output. Second, to develop and to implement technological improvements in SBEM that would allow a complete larval zebrafish brain to be acquired at a resolution sufficient for the identification of individual synapses within a realistic time-frame.

The zebrafish spinal cord was chosen as a reconstruction target because the networks contained within it are thought to be relatively simple (Kiehn, 2016), with many circuit components being known and morphologically identifiable (Hale et al., 2001; Higashijima et al., 2004b). Yet, while the ground plan of the CPG for swimming is known, the functional role of many cell types is unknown, some observations contradict the simple ground plan consisting of rhythmic, ipsilaterally descending excitation and commissural inhibition and key physiological observations still lack a mechanistic explanation. For example, it is unknown how the well-described phenomenon of orderly MN recruitment, with small MNs being recruited during weak swims and large MNs being added to the active pool during strong swims, is mechanistically implemented. Since the CPGs of higher vertebrates evolved from spinal networks for undulatory locomotion (Fetcho, 2007), the lack of a comprehensive understanding of such simple CPGs illustrates the importance of research on the zebrafish spinal cord. Resolving the connectivities between the different types of spinal neurons appeared particularly promising, since investigations of the spinal cord have historically been more focused on the physiology of individual neurons.

To this end, an ECS preserving fixation and staining protocol was developed, which allowed two complete segments and two partial segments to be acquired at a resolution sufficient to follow neurites and identify synapses. This allowed the reconstruction of the escape network postsynaptic to the Mauthner axon,

which confirmed the usefulness of the dataset, since it confirmed many predictions based on homology with the goldfish and added additional details not previously reported, such as the fact that ascending inhibitory interneurons are contacted by the Mauthner axon. Then, all MNs were reconstructed and characterized in one segment, which enabled the classification of MNs into different subtypes: small MNs that are presumably immature at this developmental stage, intermediate MNs and large MNs. Starting from representative MNs of the intermediate and of the large type, presynaptic neurons were reconstructed, which revealed that these MNs are embedded in different but overlapping presynaptic networks. More specifically, the large MN selected as a starting point for reconstructions was contacted by many RS axons, which was not the case for the intermediate MN. Further, CiDs contacting the large MN tended to have more dorsally located somata than those contacting the smaller MN. The CiD to MN connectivity was investigated in more detail, by identifying all CiDs located rostrally to the MNs, which showed that dorso-ventrally separated subtypes of CiDs differed in their MN subtype preference. Dorsally displaced CiDs were specific to large MNs, while the more ventrally located standard CiDs did not exhibit a strong specificity. These observations can constrain possible mechanisms of pattern generation in general and will be discussed in more detail in this section.

The Spinal Cord SBEM Dataset

While the resolution of the spinal cord dataset, 9 x 9 x 21 nm, was comparable to the resolution of other SBEM datasets in which circuit connectivity has been reconstructed (for example, see Briggman et al. (2011)) and while it did allow small neurites to be followed, complete cells to be reconstructed and synapses between them to be identified, synapses of different types could not reliably be distinguished. Chemical synapses can be subdivided ultrastructurally into symmetric and asymmetric subtypes (Gray, 1959). The symmetric type is characterized by a pronounced post-synaptic density (PSD) and is excitatory. The asymmetric type does not have an intense post-synaptic density and is inhibitory (Eccles, 1964). Yet, in this dataset, PSDs were generally difficult to identify. Further experiments would be necessary to determine whether this is a general property of larval zebrafish spinal cord tissue or whether an improved

staining protocol would allow their reliable identification. This problem was mitigated in this case by the fact that many spinal interneuron types have a characteristic morphology with defined transmitter phenotypes (Higashijima et al., 2004b). In particular, the CiD interneurons on which analyses were focused are excitatory and are the only cells with a long, ipsilaterally descending axon. On the other hand, CoBL interneurons were more problematic, since excitatory and inhibitory interneurons with commissural, bifurcating axons exist (Satou et al., 2012). Another problem were electrical synapses, which are generally difficult to identify in SBEM data. However, at least one type of electrical synapse could be seen: The Mauthner axon-CoLo contact is known to be electrical in goldfish and was ultrastructurally clearly distinct from all other Mauthner synapses, although synaptic vesicles were also present on the presynaptic side. While the resolution in SBEM is not sufficient to identify the individual gap junction protein complexes, the pre- and postsynaptic membranes appeared more closely apposed at this synapse and were in fact so close to each other that they appeared fused. Of course, the identification of an electrical synapse in this one case does not imply that electrical synapses can be identified in general. Yet, similarly closely apposed membranes were also seen at chemical CiD-to-MN synapses. These synapses were recently described to also have an electrical component (Song et al., 2016). Importantly, electrical CiD-to-MN synapses were always found to also have a chemical component, which makes it unlikely that important CiD-to-MN inputs were overlooked in this work due to their electrical nature.

Samples for EM often shrink during fixation and staining. Therefore, absolute size measures reported in this work may not always be directly comparable to sizes measured in living fish. The shrinkage caused by EM sample preparation was found to be 14% in one case (Helmstaedter et al., 2013) by correlative 2-photon and SBEM imaging. Since the preparation protocol used in that case was almost identical to the one used here for the spinal cord, it can be assumed that the shrinkage factor for the spinal cord sample lies in a similar range. Either way, the size of optically imaged spinal cord segments in published data at similar developmental time points shows remarkable variation, and can lie close to the values found here (Jao et al., 2012; Wang

and McLean, 2014; Wyart et al., 2009), but are 30 – 50% higher in some examples (Buckley et al., 2010; Menelaou et al., 2014). Assuming that these discrepancies are not, at least in part, caused by calibration errors, the differences could be explained by zebrafish strain differences or different raising conditions. In particular, the environmental temperature is known to affect the speed of development of larval fish (Westerfield, 2007).

Escape Network Reconstructions

The postsynaptic partners of the Mauthner axon were mostly those expected based on earlier physiological experiments on goldfish, which confirmed the utility of the spinal cord dataset for further, more comprehensive analyses. The commissural inhibitory CoLo interneuron had been suggested, but not proven, to be the zebrafish homolog of the escape-specific crossed inhibitory interneuron type of goldfish (Liao and Fetcho, 2008), based on its morphology and the fact that it fires during escape bends, but not during any other type of behavior. The results presented here confirm this suspicion. Like the other spinal interneurons contacted by the Mauthner axon, it receives the Mauthner synapse on its axon. This arrangement probably allows Mauthner-initiated escapes to override any other ongoing activity in the spinal cord and in particular to override any inhibition received on the soma or dendrites originating from a contralateral contraction. Our results thus support the established notion that the Mauthner escape network is a simple system that specifically elicits a stereotyped behavior in a highly reliable, low-latency fashion. Yet, additional complexity that had not previously been described was also revealed. That is, ipsilateral ascending inhibitory interneurons, the CiAs and commissural ascending interneurons, the CoSas, were also found to be contacted. While these interneurons are not typically included in classical descriptions of the Mauthner escape networks, finding them here is not entirely surprising. Preliminary, unpublished physiological evidence did suggest that CiAs might be activated during escapes (Abdel El Manira, personal communication) and CoSas were also found to sometimes be activated during the escape bend (Liao and Fetcho, 2008). It is possible that these contacts were not described previously due to a species difference: The spinal interneurons contacted by the Mauthner axons have, up to now, been

described primarily in the goldfish (*Carassius auratus*) and tench (*Tinca tinca*) (Fetcho and Faber, 1988; Yasargil and Sandri, 1990). These two species are, however, members of the same family as zebrafish, the Cyprinidae, suggesting a close homology. The discrepancy might also be explained simply be the relative sparsity of CiA and CoSa contacts, which were found here to be the most rarely contacted types of neurons. Either way, the fact that every single Mauthner synapse could be identified and classified in this dataset, allowing all Mauthner-postsynaptic interneurons to be identified in more than two segments, illustrates the power of EM based analyses. What could be the functional role of these cells? While the spinal targets of CiA cells are not fully known, they have been shown to inhibit MNs (Higashijima et al., 2004a). They may thus be involved in terminating the C-bend. Their ascending axons could cause the termination to occur more rapidly in the rostral spinal cord, perhaps allowing the counter-bend to begin rostrally and thereby ensuring that the bolus of water trapped by the C-bend is accelerated in the caudal direction. The role of the CoSa appears more elusive, particularly since it isn't clear whether these neurons are inhibitory or excitatory. The fact that the CoSas shown to fire during escape bends were glycinergic (Liao and Fetcho, 2008) makes it likely that we identified the glycinergic subtype. Other glycinergic CoSa cells fire during struggling or during normal swimming, and their postsynaptic partners are unknown, making this interneuron type ill-described and their role in the escape bend highly speculative. For example, if glycinergic CoSas also inhibited MNs, their role might simply be to support the commissural inhibition of the CoLos.

The Motoneuron Pool

In larval zebrafish, only MNs exit the spinal cord at the ventral roots (VRs). The only other spinal neuron that exits the spinal cord is the Rohon-Beard interneuron, but it exits the spinal cord dorsally (Bernhardt et al., 1990). This allowed MNs to be identified and characterized comprehensively, revealing an average of 69.5 MNs per hemisegment. Previously reported sizes of the MN pool varied greatly, probably due to technological limitations. For example, early estimates based on horseradish peroxidase (HRP) fills lead to an estimate of about 20 MNs per hemisegment (Myers, 1985), but this method

suffers from incomplete backfilling of the MN pool from distal axons. Later, the total number of MNs per hemisegment was estimated to be 40 based on the expression pattern of the *parg*^{mn2Et} enhancer trap line (Menelaou and McLean, 2012). A bacterial artificial chromosome (BAC) based transgenic approach yielded an estimate of 63 per hemisegment (Asakawa et al., 2013). These genetic approaches suffer from uncertainty about the completeness of genetic expression patterns. Interestingly, the value found here is identical to one of the first reports of the size of the MN pool in older, juvenile zebrafish (10 mm body length, corresponding to approximately 30 dpf), also based on EM-based counts of axons in the VRs (van Raamsdonk et al., 1983), showing that the complete adult pool of MNs is already present and sends its axons through the VRs at 6 dpf.

Based on morphological measures of the different MNs, they could be categorized into different classes. The MNs with the smallest somata were well separated from other MNs based on the fact that they had virtually no synaptic inputs and very short or even completely absent dendritic trees. Since the proportion of slow, red muscle fibers is small at 6 dpf and increases greatly later in development (Devoto et al., 1996), it is tempting to speculate that these small MNs are red-muscle specific MNs that are still immature at 6 dpf and are only integrated into the functional network later in life. This would also be consistent with counts of 28 – 30 red muscle contacting MNs in juvenile fish (van Raamsdonk et al., 1983), which correspond approximately to the number of SD-SMNs found here. The separation between MNs of intermediate size and large MNs was less clear, in particular because SMNs with bifurcating axons (B-SMNs) bridged the size between other MNs and PMNs. B-SMNs received considerable input from the displaced CiDs, in contrast to most other SMNs, which would support their assignment to the large MN category, together with PMNs. The different MN subtypes appear to undergo additional refinement in development, with four subtypes reported in adults (Ampatzis et al., 2013): Fast PMNs, fast SMNs, intermediate SMNs and slow SMNs. It seems conceivable therefore that the fast SMNs of the adult fish develop from the B-SMNs and perhaps some unusually large V-/D-SMNs and should be considered a separate class.

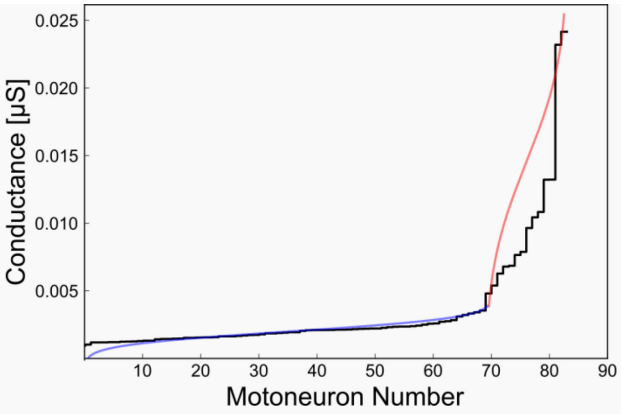

Figure 37 | Predicted Motoneuron Conductance Distribution. MN conductances predicted based on a fit of the conductance / size relationship measured by Menelaou and McLean (2012). Blue and red lines represent Gaussian fits performed individually for the MNs belonging to the intermediate and large MN clusters, respectively (compare Figure 21b).

Since the orderly recruitment of MNs crucially depends on the interaction of presynaptic networks activating the MN pool with the different MN conductances in the pool, obtaining an estimate of the conductance distribution might already constrain possible recruitment mechanism. A tight, non-linear relationship was found between conductance and soma size (Menelaou and McLean, 2012), enabling an estimation of the conductance distribution from the size distribution. The non-linear relationship causes larger MNs to be disproportionally less excitable and shapes the conductance distribution such that a small number of large MNs would require a very large current to reach a given voltage threshold, while most other MNs would require smaller currents lying in a relatively narrow range (Figure 37).

Reconstruction of Motoneuron-Presynaptic Cells

To find out whether MNs of different subtypes are embedded into different presynaptic networks, tracings were performed starting from all synaptic locations on a representative MN of the intermediate subtype and one of the large subtype. While the MNs were chosen as representative based on having a morphology typical for a MN of that class, it is not necessarily true that their synaptic contacts are representative of all synaptic contacts onto MNs of the same type. This is why, for the subsequent analysis of presynaptic CiDs, a different approach was chosen to detect these interneurons. Nevertheless, differences observed in this analysis may serve as starting points for later, more detailed investigations. Also, this analysis could only reveal interneurons

that were relatively close to the MNs chosen as starting points. Axons that contacted the MNs but exited the dataset without reaching a soma could usually not be assigned to a type. With these caveats in mind, one remarkable property of the set of cells contacting the two MNs was its relative simplicity. The expected CPG components, the CiD, CoBL and CiA cells made up almost all of the identifiable presynaptic interneurons, validating the ground plan of the CPG for swimming. It is important to note, however, that the CoBL cells, so named because they have a commissural, bifurcating and longitudinally running axon, may not represent a homogenous class. Instead, GABAergic, glycinergic and glutamatergic cells with similar morphology have been described (Satou et al., 2012), so that the identification of numerous CoBL contacts to MNs might hide additional complexity in the network. Another conspicuous feature was the absence of RS inputs to the intermediate MN, which were common on the large MN. Could RS inputs to the intermediate MN have been missed? The morphology of RS axons within the spinal cord has only been described in a few cases (Gahtan and O'Malley, 2003; Wang and McLean, 2014). In these cases, the main axonal trunk ran very ventrally or dorsally, in the vlf or dlf. This type of axonal morphology would have been easily identified, and was not present in the case of the intermediate MN. However, this does not completely exclude the possibility that other types of RS cells, for example RS cells that are involved only in weak motor outputs, do not descend in these tracts. Such an axon would have been classified as “longitudinal” in this analysis and its RS identity would not have been recognized. Either way, the results suggest that an important projection from the hindbrain to the spinal cord targets preferentially large MNs. Since most of these axons were large and myelinated, it can be speculated that they transmit signals not for routine swimming but for specific behaviors that require low initiation latencies. It is tempting to conjecture that the main reason for this difference in RS innervation between an intermediate MN and a large MN could be that intermediate MNs are usually recruited mainly by CPG components that are located in the spinal cord. These would recruit MNs independently of the brain, while the direct RS-to-MN pathway would be involved in low-latency behaviors that are particularly relevant for the animal’s survival, such as escapes or prey-directed turns. Note, however, that even a complete absence

of RS synapses on a MN does not necessarily mean that this MN can't be controlled by the brain. Coupling between MNs, in particular electrical coupling, could hypothetically make up for the lack of direct synapses.

Some inputs to the MN pool were likely missed in this analysis. In particular, no MCoDs were identified, which have been shown physiologically to synapse onto MNs (McLean et al., 2008). However, the distance between the synaptically coupled MCoD / MN pair was 16 segments in that case, and the morphology of MCoDs, with small axon collaterals far distal from the soma, suggests that MCoDs might generally not make synapses close to their soma. This would mean that, in our analysis, MCoD axons would be cut off and would be counted towards the "longitudinal" category. This means that our analysis might be missing a component that is important in generating slow swims (< 30 Hz) (McLean et al., 2007; McLean et al., 2008). However, MCoDs are silenced at higher frequencies, while it appears that CiDs also contribute to slow swims (< 30 Hz) and exclusively generate the swim patterns at moderate and high frequencies, in the 30 – 80 Hz range.

CiD-to-MN Connectivity

An unbiased identification of CiD interneurons was performed to obtain a comprehensive wiring matrix between local CiDs and MNs. This was possible because the CiDs are morphologically unique among the spinal interneurons in that they have an ipsilateral primarily descending axon (Hale et al., 2001; Kimura et al., 2006). Thus, it can be assumed that all CiDs that were close to the reconstructed MN pool were identified. However, CiDs have long axons and some of the CiD somata contacting the reconstructed MN pool might lie outside the dataset. Additionally, CiD axons course dorsally as they descend along the spinal cord, so that distal parts of the axon could conceivably have different MN specificities than proximal parts. Two points mitigate this potential issue: 1) While CiD axons are long, in the range of 200 – 1500 µm, their collaterals, where synapses are made, tend to be relatively close to the soma, in the 2 – 3 neighboring segments (Menelaou et al., 2014) and 2) the CiDs for which we find the specific connectivity to large, dorsal MNs, are the most dorsal ones. That is, if their axons ended up further dorsal at more caudal locations, it would be unlikely that they would contact smaller MNs there.

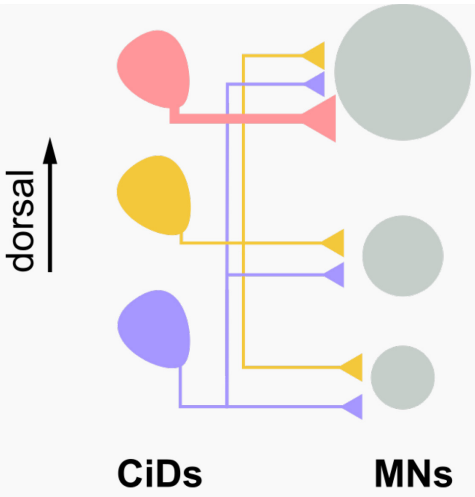

Figure 38 | Summary of CiD to Motoneuron wiring pattern found here. The most dorsal CiDs specifically form large synapses onto large MNs.

We measured synaptic efficacy indirectly, by measuring the contact area of synapses. While differences in membrane properties, through differential expression of transmembrane receptors and ion channels, could conceivably influence synaptic strength without a concomitant change in size, synaptic size has been found to correlate with synaptic strength in a number of cases, such as hippocampal CA1 dendrites (Harris and Stevens, 1989) or in CA3 axon terminals (Holderith et al., 2012). It therefore appears plausible that larger CiD synapses on MNs are also stronger than smaller synapses. However, our analysis of specificity is not affected by this point, since the specific connectivity between dorsally displaced CiDs and large MNs is also present without taking contact area into account.

Mechanistically understanding the regulation of muscle contraction strength, through the orderly recruitment of MNs, was the main focus of the CiD-to-MN connectivity reconstructions. Early models of MN recruitment assumed homogenous presynaptic networks, with diffuse wiring between presynaptic neurons and MNs. The recruitment order would then be determined by biophysical differences between the MNs. Since the recruitment of CiDs switches between ventral and dorsal subsets for different swim speeds (McLean et al., 2008), the underlying assumption of homogeneity does not hold in fish. Orderly recruitment could still be achieved with diffuse wiring, but would require the recruitment order to be encoded in synaptic strength differences between the different CiD subsets (Figure 9a). The wiring pattern we find here reflects the modular recruitment of CiDs, with the most dorsal CiDs, which are recruited during the strongest swims, also being distinct in their wiring to large MNs exclusively. In contrast, more ventral CiDs wired to the MN pool in a non-

specific fashion (Figure 38). This represents a combination of the diffuse, Henneman-style wiring (Figure 9a) and the specific, subtype-to-subtype connectivity described in adult fish (Figure 9c) (Ampatzis et al., 2014). What could be the purpose of this connectivity? It should be noted that the assumptions on which early models of MN recruitment were based and from which the idea of diffuse connectivity was derived (Henneman et al., 1965), did not take into account the possibility of different presynaptic neurons being engaged in a mutually exclusive fashion when motor outputs of different force are generated, as is the case for larval zebrafish (Figure 8) (McLean et al., 2008). This fact alone implies that the recruitment mechanism of MNs in larval zebrafish should be more complex, since the dorsally displaced CiDs and dorsal CiDs which are exclusively active during fast swims need to be able to recruit the full MN pool, including PMNs, alone. As described above, the PMNs have, based on their size, a disproportionally high input conductance. Additionally, they seem to have a lower ratio of dendritic tree length to soma size than SMNs, which would imply a lower number of synapses per soma size (Figure 20, 19e). Taken together, this suggests that the role of the displaced CiDs is to specifically add the most difficult to recruit, largest MNs to the active MN pool only during the most vigorous of swims, during which only the more dorsal CiDs are active. This picture is consistent with the finding that, when comparing slow swims to fast swims, the in-phase excitatory currents to the largest MNs increase by a much larger factor than the currents onto smaller MNs (Kishore et al., 2014).

Implications for Spinal Pattern Generation Mechanisms

What do these findings tell us about mechanisms of motor pattern generation in the spinal cord in general? In fish, motor outputs are essentially described by three parameters: 1) the muscle contraction amplitude, discussed above in the context of orderly MN recruitment, 2) The rostro-caudal phase lag, 3) the burst frequency.

Different mechanisms have been proposed for the establishment of an appropriate rostro-caudal phase lag. One important observation concerning the rostro-caudal delay, which constrains possible mechanisms of its generation, should be pointed out once again here: Axonal conduction velocities are

generally much faster than the rostro-caudal propagation of the contraction wave along the tail of a larval zebrafish, which is in the range of 0.06 – 1.2 m / s (McLean et al., 2008), depending on swim speeds. In contrast, the slowest axons have a conduction velocity of about 0.6 m / s (Waxman and Bennett, 1972). This implies that the large and mostly myelinated RS axons would excite their postsynaptic targets at the caudal end of the spinal cord earlier than the rostro-caudally propagating wave of muscle contraction should arrive at that location. If biophysical properties of the postsynaptic MNs and of the RS axons were fine-tuned along the length of the tail so that the MN recruitment threshold was reached at different, progressively later time points when going from rostral to caudal (Tunstall and Sillar, 1993), RS axons could still control MNs directly with the appropriate phase lag. However, since RS synapses appear to be rare on smaller MNs, this possibility seems less plausible than the possibility that the excitatory interneurons of the spinal cord generate the phase delay. In that view, routine swims would be driven by ongoing activity in excitatory interneurons. Recurrent connections between these excitatory interneurons would support the sustained activity of the CPG (Li et al., 2009) and the unequal distribution of their synapses over the length of the tail, with more synapses being made rostrally, would cause the rostro-caudal lag (Wolf et al., 2009).

How could bursts of the appropriate frequency be generated and regulated? Cell-intrinsic, biophysical properties have often been emphasized (see Central Pattern Generators, p. 22). Different subtypes of CiDs might have different intrinsic frequencies, which could be a possible explanation for the observation that only subtypes of CiDs are activated for specific swim frequencies. However, bursts of different frequencies might also be generated by neural networks. For example, negative feedbacks in the presence of tonic excitation could produce oscillatory activity. This could involve the descending CiD cells activating the ascending inhibitory CiA cells. At this point, such a network is speculative, but could easily be tested using the dataset produced in this work.

Whole Brain Stack Acquisition

In this work, improvements to SBEM technology were implemented that allowed the tile movement overhead to be reduced by more than 80% and that

allowed tile patterns to be adapted closely to the irregular shape of a sample, reducing the scanned volume by up to 60%. This made it possible to acquire a SBEM stack of a larval zebrafish brain at a resolution sufficient to follow neurites and to identify synapses, the first such stack obtained for a vertebrate. The dataset therefore has the potential to be applicable and useful in a broad range of behaviors that are computed by the brain. SBEM imaging was combined with 2-photon calcium imaging, to identify pretectal cells involved in the OKR and a local proof-of-concept registration was demonstrated, which allowed individual, functionally characterized somata to be identified and subsequently traced. The tracing for a monocular direction-selective pretectal cell was consistent with the idea that the cell receives direct RGC input based on the location of the synapses, but tracings of the presynaptic partners would have to be performed to confirm their identity.

Line scanning proved to be a highly effective method for increasing the size of individual image tiles, but it made a more complicated image registration procedure necessary to compensate for distortions along the stage movement axis. The dynamic tile pattern, which changed on every slice, made it necessary to adapt the scan length constantly, which in turn made it necessary to use a dynamic model of the piezo behavior to pre-compute voltages that would lead to an approximately linear piezo motion. If the requirement of changing tile sizes did not exist, as is the case for most SBEM stacks which only contain small parts of a much larger piece of tissue, a more straightforward approach could have been taken. Voltage patterns leading to perfectly linear motion could have been determined ahead of time and simply played back repeatedly. This approach would make the subsequent image registration step considerably less complex. A different and complementary approach of reducing the stage movement overhead would be to reduce the settling time for a single motor move. This settling time was 3 seconds on the setup used in this work, which was mostly spent waiting on movement-induced vibrations to settle. With a less vibration-prone microtome, such as a microtome based on a commercially available SEM stage, this number could be significantly reduced (Kevin Briggman, personal communication).

Running the downstream asher periodically to remove hydrocarbon deposits from the backscatter detector diode proved effective at maintaining the detector's sensitivity over the duration of the stack. However, running the downstream asher caused changes in sample contrast due to changes in the detector's sensitivity and caused changes in focus and astigmatism. This made it necessary to manually interrupt and re-start the acquisition every few days to activate the asher and re-focus the stack afterwards. This could likely be avoided by running the downstream asher much more often for much shorter durations. It could be promising to activate the downstream asher for ca. 3 seconds on every slice, which would yield the same total ashing duration but might allow manual interruptions to be avoided and would also avoid sudden changes in image contrast caused by changes in detector sensitivity. Additional experimentation is necessary to determine whether this approach can work and allow a fully unattended acquisition of large SBEM stacks over several months.

With the improvements demonstrated here in place, 85% of the total acquisition time was spent either cutting or imaging the sample. This means that no simple to reduce overheads remain that would allow even faster SBEM acquisitions. Even more rapid data acquisition, as would be required to scale the technology to samples much bigger in size than those considered here, such as a complete mouse brain, will therefore require significant novel technological developments. One such novel development would be the use of a multi-beam SEM microscope. In these microscopes, several beams scan the same in parallel, which allows the acquisition speed to be multiplied by the number of beams (Keller et al., 2014). Another, parallel approach would be to parallelize the stack acquisition over several microscopes. This could be achieved by cutting a sample into different pieces which would then be imaged independently. Lossless partitioning has recently been demonstrating using a heated knife (Hayworth et al., 2015).

Due to the loss of tile overlap caused by a change in pixel scaling for a series of sections in the border region between the midbrain and forebrain, the telencephalon was not included in the final registration of the complete dataset. In principle, the missing telencephalic regions could be included in the global registration, but the lack of tile-tile overlap means that it might not be possible

to follow some of the neurites that pass through the affected region. Tracing axons that run orthogonally to the imaging plane should, however, in most cases not be problematic. If this proved to be particularly problematic for a given reconstruction target, a new dataset could be acquired with a realistic amount of effort using the technologies implemented in this work.

Pretectal OKR Network Reconstructions

By manually choosing correspondence points from a local region surrounding a blood vessel bifurcation, it was possible to register a 2-photon GCaMP5G stack of the pretectum to the SBEM stack using an affine transformation applied to the 2-photon data. Cell bodies could be matched between both modalities in that local region. A registration that would allow all functionally characterized pretectal cell bodies to be matched was not yet performed. During the EM preparation, different brain regions could deform differently and could translate and / or rotate relative to each other, particularly when they are separated by ventricles and therefore not tightly held together. For this reason, it might not be possible to register both datasets globally using just one affine transformation and it might be necessary to align different regions independently. Alternatively, a non-linear transformation, for example using a thin plate spline transformation (Bogovic et al., 2015), could be used for global registration. In future experiments, the registration might be aided by using markers that are visible in both imaging modalities, such as injectable fluorescent beads or by genetically expressing proteins that can be detected both optically and in EM, such as the fluorescent ascorbate peroxidase APEX fused to GFP (Martell et al., 2012).

The proof-of-concept tracing for a MoNR (monocular direction-selective) pretectal cell showed that it had a dendritic arbor that finely arborized and received synaptic inputs in the region in which the optic nerve arborization fields 4 and 5 are expected to lie (Figure 36) (Robles et al., 2014). Whether the synapses made there are actually from RGCs could not be directly determined at this point. The presynaptic axons would need to be followed to make that decisions. Since the eyes are not contained in the dataset, RGC axons could be identified by following them backwards up to the optic chiasm, but a further categorization could only be performed based on the axonal morphology, not the morphology of the dendrites in the retina.

The functional imaging experiments make strong predictions about the trajectory of at least a subset of MoNR cells: Since direction selective input from the contralateral eye is necessary to explain response patterns of cells with binocular receptive fields, some of the simple direction selective cells should have commissural axons. This does not appear to be the case for the cell reconstructed here, implying that either an additional relay neuron is involved or that the MoNR population is not homogenous, and consists of a morphologically diverse set of cells.

Conclusions and Outlook

By reconstructing a MN pool and parts of the presynaptic spinal network that controls it, it was shown that different MN types were embedded into different spinal subnetworks. That is, a large MN received considerable RS input, and large MNs in general received synapses from the most dorsal CiD cells, which barely contacted smaller MNs. The direct RS wiring likely reflects the fact that large MNs are specifically recruited in life and death situations, in which low latency reactions, mediated by large, myelinated axons, are essential. The specific connectivity from dorsal CiDs, which generate the high-frequency rhythm of fast swims, probably serves to compensate for the very low input resistance of large MNs, allowing them to be recruited despite their low excitability. The unspecific connectivity from ventral CiDs to MNs means that the recruitment order of MNs during weaker swimming must be determined by biophysical MN properties. These data also lead to detailed predictions of further developmental changes. To reach the connectivity of adult fish (Ampatzis et al., 2014), two things must happen: 1) The unspecific CiDs must refine their connectivity through the elimination of synapses and 2) the set of MNs that received no synapses at the developmental time point considered here must mature and receive specific synapses from a set of CiDs that either is yet to be born or develops from a subset of the ventral CiDs.

The patterns of connectivity analyzed here contain only a small part of the cells and synapses present in the SBEM stack, which allows many further analyses. As discussed above, the mechanisms of burst generation and rostro-caudal propagation of activity along the tail might involve connections between different types of spinal interneurons. In that context, reconstructing the connections between CiDs and CiAs would be particularly interesting and might reveal distinct subnetworks that generate bursts of different frequencies. The recurrent connections between CiDs would also be potentially enlightening, since the exclusive activity of either ventral or dorsal subsets of CiDs might be reflected in these connections.

Physiological experiments would complement these future reconstructions. For a complete understanding of burst generation mechanisms, it would be important to measure the differences in cell-intrinsic biophysical properties of different CiDs, by measuring their transfer functions depending on their positions. These might contribute to their activity during swims of different frequencies. Possible mechanisms of rostro-caudal activity propagation could be considerably constrained by measuring whether MNs and excitatory interneurons differ in their excitabilities along the length of the tail.

Technological improvements for SBEM were implemented that allowed a stack of the complete brain of a 5 day old larval zebrafish to be acquired in considerably less time than previously, in two months instead of approximately 7. The acquisition did not run fully unattended, because the stack had to be interrupted to activate the downstream asher to remove hydrocarbon deposits from the backscattered electron detector diode in regular intervals. Automating this process would likely help considerably in making this type of experiment routine, which would allow many different whole-brain stacks to be obtained and compared, for example from different genetic lines or after various types of functional characterization.

The analysis of the whole brain dataset acquired in this work has just begun. While the OKR system was chosen as a starting point for reconstructions due to the availability of functional information about the cells that are involved in that behavior, many other reconstruction targets exist that could yield valuable insights even without a prior functional characterization. The projection from the tectum to the hindbrain would be of particular interest. The tectal cells that send motor commands to the hindbrain could be identified by tracing backwards from the tectobulbar projection. Since the tectum is retinotopically organized (Karlstrom et al., 1996; Muto et al., 2013), these cells might perform a visuo-motor transformation by contacting different sets of RS neurons in the hindbrain, or by contacting RS neurons with different strength, depending on their position in the tectum.

The great hope is that this dataset and similar datasets will become valuable, standard and public resources that can be used in any investigation of neural circuit function in the larval zebrafish.

Abbreviations

ACSF	artificial cerebrospinal fluid
AIC	Akaike information criterium
API	application programming interface
ATUM	automatic tape-collecting ultramicrotome
BAC	bacterial artificial chromosome
BDMA	benzyldimethylamine
BIC	Bayesian information criterium
CB	cacodylate buffer (in the context of sample fixation and staining)
CB	carbon black (in the context of plastic embedding)
CCD	charge-coupled device
CiA	circumferential ascending
CiD	circumferential descending
CNN	convolutional neural network
CoBL	commissural bifurcating longitudinal
CoLo	commissural local
CoPA	commissural primary asceding
CoSA	commissural secondary ascending
CPG	central pattern generator
CPU	central processing unit
DDSA	dodecenylsuccinic anhydride
dlf	dorsal longitudinal fasciculus
dpf	days post fertilization
DS	direction-selective
DV	dorso-ventral
ECS	extracellular space
EM	electron microscopy
ER	endoplasmic reticulum
FIB-SEM	focused ion beam milling scanning electron microscopy
FOV	field of view
GMM	Gaussian mixture model
HRP	horseradish peroxidase
kV	kilovolts
M	molar
MCoD	multipolar commissural descending
ML	medio-lateral
mM	millimolar
MN	motoneuron
mOsm	milliosmolar
MPx	megapixels
nA	nanoampere
nm	nanometer
NMA	nadic methyl anhydride
NMDA	N-methyl-D-aspartate

ns	Nanoseconds
OKR	optokinetic response
PC	principal component
PCA	principal component analysis
PMN	primary motoneuron
PSD	postsynaptic density
RB	Rohon-Beard
RGC	retinal ganglion cell
ROI	region of interest
rOTO	reduced osmium, thiocarbohydrazide, osmium
RS	reticulospinal
sAHP	slow after-hyperpolarization
SBEM	serial block-face scanning electron microscopy
SEM	scanning electron microscopy
SMN	secondary motoneuron
ssTEM	serial section transmission electron microscopy
TB	terabytes
TCH	thiocarbohydrazide
TEM	transmission electron microscopy
TTL	transistor-transistor logic
UCoD	unipolar commissural descending
vlf	ventral longitudinal fasciculus
W	Watts

References

Ahrens, M.B., Orger, M.B., Robson, D.N., Li, J.M., and Keller, P.J. (2013). Whole-brain functional imaging at cellular resolution using light-sheet microscopy. Nature Methods 10, 413-420.

Akerboom, J., Chen, T.W., Wardill, T.J., Tian, L., Marvin, J.S., Mutlu, S., Calderon, N.C., Esposti, F., Borghuis, B.G., Sun, X.R.*, et al.* (2012). Optimization of a GCaMP Calcium Indicator for Neural Activity Imaging. Journal of Neuroscience 32, 13819-13840.

Ampatzis, K., Song, J., Ausborn, J., and El Manira, A. (2013). Pattern of innervation and recruitment of different classes of motoneurons in adult zebrafish. Journal of Neuroscience 33, 10875-10886.

Ampatzis, K., Song, J., Ausborn, J., and El Manira, A. (2014). Separate microcircuit modules of distinct V2a interneurons and motoneurons control the speed of locomotion. Neuron 83, 934-943.

Asakawa, K., Abe, G., and Kawakami, K. (2013). Cellular dissection of the spinal cord motor column by BAC transgenesis and gene trapping in zebrafish. Frontiers in Neural Circuits 7, 100.

Bear, M., Connors, B., and Paradiso, M. (2015). Neuroscience: Exploring the Brain, 4 edn (Wolters Kluwer Health).

Bernhardt, R.R., Chitnis, A.B., Lindamer, L., and Kuwada, J.Y. (1990). Identification of spinal neurons in the embryonic and larval zebrafish. Journal of Comparative Neurology 302, 603-616.

Berning, M., Boergens, K.M., and Helmstaedter, M. (2015). SegEM: Efficient Image Analysis for High-Resolution Connectomics. Neuron 87, 1193-1206.

Biro, Z., Hill, R.H., and Grillner, S. (2006). 5-HT modulation of identified segmental premotor interneurons in the lamprey spinal cord. Journal of Neurophysiology 96, 931-935.

Bock, D.D., Lee, W.C.A., Kerlin, A.M., Andermann, M.L., Hood, G., Wetzel, A.W., Yurgenson, S., Soucy, E.R., Kim, H.S., and Reid, R.C. (2011). Network anatomy and in vivo physiology of visual cortical neurons. Nature 471, 177-182.

Bogovic, J.A., Hanslovsky, P., Wong, A., and Saalfeld, S. (2015). Robust Registration of Calcium Images by Learned Contrast Synthesis. In ArXiv e-prints.

Briggman, K.L., and Bock, D.D. (2012). Volume electron microscopy for neuronal circuit reconstruction. Current Opinion in Neurobiology 22, 154-161.

Briggman, K.L., Helmstaedter, M., and Denk, W. (2011). Wiring specificity in the direction-selectivity circuit of the retina. Nature 471, 183-188.

Buchanan, J.T. (1982). Identification of Interneurons with Contralateral, Caudal Axons in the Lamprey Spinal-Cord - Synaptic-Interactions and Morphology. Journal of Neurophysiology 47, 961-975.

Buchanan, J.T., and Grillner, S. (1987). Newly identified 'glutamate interneurons' and their role in locomotion in the lamprey spinal cord. Science 236, 312-314.

Buchanan, J.T., Grillner, S., Cullheim, S., and Risling, M. (1989). Identification of Excitatory Interneurons Contributing to Generation of Locomotion in Lamprey - Structure, Pharmacology, and Function. Journal of Neurophysiology 62, 59-69.

Buckley, C.E., Marguerie, A., Alderton, W.K., and Franklin, R.J.M. (2010). Temporal Dynamics of Myelination in the Zebrafish Spinal Cord. Glia 58, 802-812.

Budick, S.A., and O'Malley, D.M. (2000). Locomotor repertoire of the larval zebrafish: swimming, turning and prey capture. Journal of Experimental Biology 203, 2565-2579.

Burke, R.E. (1968). Group Ia Synaptic Input to Fast and Slow Twitch Motor Units of Cat Triceps Surae. Journal of Physiology-London 196, 605-630.

Butler, A.B., and Hodos, W. (2005). Comparative vertebrate neuroanatomy: evolution and adaptation, 2nd edn (Hoboken, N.J.: Wiley-Interscience).

Cangiano, L., and Grillner, S. (2003). Fast and slow locomotor burst generation in the hemispinal cord of the lamprey. Journal of Neurophysiology 89, 2931-2942.

Cope, T.C., and Pinter, M.J. (1995). The size principle: Still working after all these years. News in Physiological Sciences 10, 280-286.

Cragg, B. (1979). Overcoming the Failure of Electron-Microscopy to Preserve the Brains Extracellular-Space. Trends in Neurosciences 2, 159-161.

Cragg, B. (1980). Preservation of Extracellular-Space during Fixation of the Brain for Electron-Microscopy. Tissue & Cell 12, 63-72.

Dale, N. (1985). Reciprocal Inhibitory Interneurones in the Xenopus Embryo Spinal-Cord. Journal of Physiology-London 363, 61-70.

Dale, N., and Roberts, A. (1985). Dual-Component Amino-Acid-Mediated Synaptic Potentials - Excitatory Drive for Swimming in Xenopus Embryos. Journal of Physiology-London 363, 35-59.

Denk, W., Helmstaedter, M., and Briggman, K.L. (2012). Structural neurobiology: missing link to a mechanistic understanding of neural computation. Nature Reviews Neuroscience 13, 351-358.

Denk, W., and Horstmann, H. (2004). Serial block-face scanning electron microscopy to reconstruct three-dimensional tissue nanostructure. PLoS Biology 2, 1900-1909.

Devoto, S.H., Melancon, E., Eisen, J.S., and Westerfield, M. (1996). Identification of separate slow and fast muscle precursor cells in vivo, prior to somite formation. Development 122, 3371-3380.

Di Prisco, G.V., Wallen, P., and Grillner, S. (1990). Synaptic Effects of Intraspinal Stretch-Receptor Neurons Mediating Movement-Related Feedback during Locomotion. Brain Research 530, 161-166.

Drapeau, P., Saint-Amant, L., Buss, R.R., and Chong, M. (2002). Development of the locomotor network in zebrafish. Progress in Neurobiology 68, 85-111.

Eccles, J.C. (1964). The physiology of synapses (New York: Springer).

El Manira, A., Tegner, J., and Grillner, S. (1994). Calcium-Dependent Potassium Channels Play a Critical Role for Burst Termination in the Locomotor Network in Lamprey. Journal of Neurophysiology 72, 1852-1861.

Fetcho, J.R. (1991). Spinal Network of the Mauthner Cell. Brain Behavior and Evolution 37, 298-316.

Fetcho, J.R. (1992). Excitation of Motoneurons by the Mauthner Axon in Goldfish - Complexities in a Simple Reticulospinal Pathway. Journal of Neurophysiology 67, 1574-1586.

Fetcho, J.R. (2007). The utility of zebrafish for studies of the comparative biology of motor systems. Journal of Experimental Zoology Part B-Molecular and Developmental Evolution 308b, 550-562.

Fetcho, J.R., and Faber, D.S. (1988). Identification of Motoneurons and Interneurons in the Spinal Network for Escapes Initiated by the Mauthner Cell in Goldfish. Journal of Neuroscience 8, 4192-4213.

Gabriel, J.P., Ausborn, J., Ampatzis, K., and Mahmood, R. (2011). Principles governing recruitment of motoneurons during swimming in zebrafish. Nature Neuroscience 14, 93-99.

Gabriel, J.P., Trivedi, C.A., Maurer, C.M., Ryu, S., and Bollmann, J.H. (2012). Layer-specific targeting of direction-selective neurons in the zebrafish optic tectum. Neuron 76, 1147-1160.

Gahtan, E., and Baier, H. (2004). Of lasers, mutants, and see-through brains: Functional neuroanatomy in zebrafish. Journal of Neurobiology 59, 147-161.

Gahtan, E., and O'Malley, D.M. (2003). Visually guided injection of identified reticulospinal neurons in zebrafish: A survey of spinal arborization patterns. Journal of Comparative Neurology 459, 186-200.

Gahtan, E., Sankrithi, N., Campos, J.B., and O'Malley, D.M. (2002). Evidence for a widespread brain stem escape network in larval zebrafish. Journal of Neurophysiology 87, 608-614.

Gazzola, M., Van Rees, W.M., and Koumoutsakos, P. (2012). C-start: optimal start of larval fish. Journal of Fluid Mechanics 698, 5-18.

Gray, E.G. (1959). Axo-Somatic and Axo-Dendritic Synapses of the Cerebral Cortex - an Electron Microscope Study. Journal of Anatomy 93, 420-433.

Grillner, S. (2003). The motor infrastructure: From ion channels to neuronal networks. Nature Reviews Neuroscience 4, 573-586.

Grillner, S. (2006). Biological pattern generation: the cellular and computational logic of networks in motion. Neuron 52, 751-766.

Hagberg, A., Schult, D., and Swart, P. Exploring Network Structure, Dynamics and Function using Networkx. In Proceedings of the 7th Python in Science conference (SciPy 2008), G. Varoquay, T. Vaught, and J. Millman, eds., pp. 11-15.

Hale, M.E., Ritter, D.A., and Fetcho, J.R. (2001). A confocal study of spinal interneurons in living larval zebrafish. Journal of Comparative Neurology 437, 1-16.

Harris, K., and Stevens, J. (1989). Dendritic Spines of CA 1 Pyramidal Cells in the Rat Hippocampus: Serial Electron Microscopy with Reference to Their Biophysical Characteristics. The Journal of Neuroscience 9, 2982-2997.

Hayat, M.A. (1989). Principles and Techniques of Biological Electron Microscopy, 3rd edn (Cambridge University Press).

Hayworth, K.J., Xu, C.S., Lu, Z.Y., Knott, G.W., Fetter, R.D., Tapia, J.C., Lichtman, J.W., and Hess, H.F. (2015). Ultrastructurally smooth thick partitioning and volume stitching for large-scale connectomics. Nature Methods 12, 319-322.

Helmstaedter, M., Briggman, K.L., and Denk, W. (2008). 3D structural imaging of the brain with photons and electrons. Current Opinion in Neurobiology 18, 633-641.

Helmstaedter, M., Briggman, K.L., and Denk, W. (2011). High-accuracy neurite reconstruction for high-throughput neuroanatomy. Nature Neuroscience 14, 1081-1088.

Helmstaedter, M., Briggman, K.L., Turaga, S.C., Jain, V., Seung, H.S., and Denk, W. (2013). Connectomic reconstruction of the inner plexiform layer in the mouse retina. Nature 500, 168-174.

Helmstaedter, M., and Mitra, P.P. (2012). Computational methods and challenges for large-scale circuit mapping. Current opinion in neurobiology 22, 162-169.

Henneman, E. (1957). Relation between Size of Neurons and Their Susceptibility to Discharge. Science 126, 1345-1347.

Henneman, E., Somjen, G., and Carpenter, D.O. (1965). Functional Significance of Cell Size in Spinal Motoneurons. Journal of Neurophysiology 28, 560-580.

Higashijima, S., Masino, M.A., Mandel, G., and Fetcho, J.R. (2004a). Engrailed-1 Expression Marks a Primitive Class of Inhibitory Spinal Interneuron. The Journal of Neuroscience 24, 5827-5839.

Higashijima, S., Schaefer, M., and Fetcho, J.R. (2004b). Neurotransmitter properties of spinal interneurons in embryonic and larval zebrafish. Journal of Comparative Neurology 480, 19-37.

Hill, A., Howard, C.V., Strahle, U., and Cossins, A. (2003). Neurodevelopmental defects in zebrafish (Danio rerio) at environmentally relevant dioxin (TCDD) concentrations. Toxicological Sciences 76, 392-399.

Holderith, N., Lorincz, A., Katona, G., Rózsa, B., Kulik, A., Watanabe, M., and Nusser, Z. (2012). Release probability of hippocampal glutamatergic terminals scales with the size of the active zone. Nature Neuroscience 15.

Huang, K.H., Ahrens, M.B., Dunn, T.W., and Engert, F. (2013). Spinal Projection Neurons Control Turning Behaviors in Zebrafish. Current Biology 23, 1566-1573.

Hunter, J.D. (2007). Matplotlib: A 2D graphics environment. Computing in Science & Engineering 9, 90-95.

Jao, L.E., Appel, B., and Wente, S.R. (2012). A zebrafish model of lethal congenital contracture syndrome 1 reveals Gle1 function in spinal neural precursor survival and motor axon arborization. Development 139, 1316-1326.

Jeffress, L.A. (1948). A Place Theory of Sound Localization. Journal of Comparative and Physiological Psychology 41, 35-39.

Joris, P.X., Smith, P.H., and Yin, T.C.T. (1998). Coincidence detection in the auditory system: 50 years after Jeffress. Neuron 21, 1235-1238.

Kanda, K., Burke, R., and Walmsley, B. (1977). Differential control of fast and slow twitch motor units in the decerebrate cat. Experimental Brain Research 29, 57-74.

Karlstrom, R.O., Trowe, T., Klostermann, S., Baier, H., Brand, M., Crawford, A.D., Grunewald, B., Haffter, P., Hoffmann, H., Meyer, S.U.*, et al.* (1996).

Zebrafish mutations affecting retinotectal axon pathfinding. Development 123, 427-438.

Karnovsky, M.J. (1971). Use of ferrocyanide-reduced osmium tetroxide in electron microscopy. Journal of Cell Biology 51, 146a.

Kasthuri, N., Hayworth, K.J., Berger, D.R., Schalek, R.L., Conchello, J.A., Knowles-Barley, S., Lee, D., Vazquez-Reina, A., Kaynig, V., Jones, T.R.*, et al.* (2015). Saturated Reconstruction of a Volume of Neocortex. Cell 162, 648-661.

Keller, A.L., Zeidler, D., and Kemen, T. (2014). High throughput data acquisition with a multi-beam SEM. Scanning Microscopies 2014 9236.

Kiehn, O. (2016). Decoding the organization of spinal circuits that control locomotion. Nature Reviews Neuroscience 17, 224-238.

Kimmel, C.B., Powell, S.L., and Metcalfe, W.K. (1982). Brain Neurons Which Project to the Spinal-Cord in Young Larvae of the Zebrafish. Journal of Comparative Neurology 205, 112-127.

Kimura, Y., Okamura, Y., and Higashijima, S. (2006). alx, a zebrafish homolog of Chx10, marks ipsilateral descending excitatory interneurons that participate in the regulation of spinal locomotor circuits. Journal of Neuroscience 26, 5684-5697.

Kishore, S., Bagnall, M.W., and McLean, D.L. (2014). Systematic Shifts in the Balance of Excitation and Inhibition Coordinate the Activity of Axial Motor Pools at Different Speeds of Locomotion. Journal of Neuroscience 34, 14046-14054.

Knogler, L.D., and Drapeau, P. (2014). Sensory gating of an embryonic zebrafish interneuron during spontaneous motor behaviors. Frontiers in Neural Circuits 8.

Knott, G., Marchman, H., Wall, D., and Lich, B. (2008). Serial section scanning electron microscopy of adult brain tissue using focused ion beam milling. Journal of Neuroscience 28, 2959-2964.

Kohashi, T., and Oda, Y. (2008). Initiation of Mauthner- or Non-Mauthner-Mediated Fast Escape Evoked by Different Modes of Sensory Input. Journal of Neuroscience 28, 10641-10653.

Kriellaars, D.J., Brownstone, R.M., Noga, B.R., and Jordan, L.M. (1994). Mechanical Entrainment of Fictive Locomotion in the Decerebrate Cat. Journal of Neurophysiology 71, 2074-2086.

Kubo, F., Hablitzel, B., Dal Maschio, M., Driever, W., Baier, H., and Arrenberg, A.B. (2014). Functional Architecture of an Optic Flow-Responsive Area that Drives Horizontal Eye Movements in Zebrafish. Neuron 81, 1344-1359.

Le, S., Josse, J., and Husson, F. (2008). FactoMineR: An R package for multivariate analysis. Journal of Statistical Software 25, 1-18.

Li, W.-C.C., Soffe, S.R., Wolf, E., and Roberts, A. (2006). Persistent responses to brief stimuli: feedback excitation among brainstem neurons. Journal of Neuroscience 26, 4026-4035.

Li, W.C., Higashijima, S., Parry, D.M., Roberts, A., and Soffe, S.R. (2004). Primitive roles for inhibitory interneurons in developing frog spinal cord. Journal of Neuroscience 24, 5840-5848.

Li, W.C., and Moult, P.R. (2012). The Control of Locomotor Frequency by Excitation and Inhibition. Journal of Neuroscience 32, 6220-6230.

Li, W.C., Perrins, R., Soffe, S.R., Yoshida, M., Walford, A., and Roberts, A. (2001). Defining classes of spinal interneuron and their axonal projections in hatchling Xenopus laevis tadpoles. Journal of Comparative Neurology 441, 248-265.

Li, W.C., Roberts, A., and Soffe, S.R. (2009). Locomotor rhythm maintenance: electrical coupling among premotor excitatory interneurons in the brainstem and spinal cord of young Xenopus tadpoles. The Journal of Physiology 587.

Li, W.C., Soffe, S.R., and Roberts, A. (2003). The spinal Interneurons and properties of glutamatergic synapses in a primitive vertebrate cutaneous flexion reflex. Journal of Neuroscience 23, 9068-9077.

Liao, J.C., and Fetcho, J.R. (2008). Shared versus Specialized Glycinergic Spinal Interneurons in Axial Motor Circuits of Larval Zebrafish. The Journal of Neuroscience 28.

Liddell, E.G.T., and Sherrington, C.S. (1925). Recruitment and some other features of reflex inhibition. Proceedings of the Royal Society of London B 97, 488-518.

Lister, J.A., Robertson, C.P., Lepage, T., Johnson, S.L., and Raible, D.W. (1999). nacre encodes a zebrafish microphthalmia-related protein that regulates neural-crest-derived pigment cell fate. Development 126, 3757-3767.

Liu, K.S., and Fetcho, J.R. (1999). Laser ablations reveal functional relationships of segmental hindbrain neurons in zebrafish. Neuron 23, 325-335.

Ljunggren, E.E., Haupt, S., Ausborn, J., Ampatzis, K., and El Manira, A. (2014). Optogenetic activation of excitatory premotor interneurons is sufficient to generate coordinated locomotor activity in larval zebrafish. Journal of Neuroscience 34, 134-139.

Marder, E., and Bucher, D. (2007). Understanding circuit dynamics using the stomatogastric nervous system of lobsters and crabs. Annual Review of Physiology 69, 291-316.

Martell, J.D., Deerinck, T.J., Sancak, Y., Poulos, T.L., Mootha, V.K., Sosinsky, G.E., Ellisman, M.H., and Ting, A.Y. (2012). Engineered ascorbate peroxidase as a genetically encoded reporter for electron microscopy. Nature Biotechnology 30, 1143-+.

Masino, M.A., and Fetcho, J.R. (2005). Fictive swimming motor patterns in wild type and mutant larval zebrafish. Journal of Neurophysiology 93, 3177-3188.

Masland, R.H. (2012). The neuronal organization of the retina. Neuron 76, 266-280.

Mathieson, W.B., and Maler, L. (1988). Morphological and Electrophysiological Properties of a Novel Invitro Preparation: the Electrosensory Lateral Line Lobe Brain Slice. Journal of Comparative Physiology A 163, 489-506.

McClenahan, P., Troup, M., and Scott, E.K. (2012). Fin-Tail Coordination during Escape and Predatory Behavior in Larval Zebrafish. PLoS One 7.

McDearmid, J.R., and Drapeau, P. (2006). Rhythmic motor activity evoked by NMDA in the spinal zebrafish larva. Journal of Neurophysiology 95, 401-417.

McElligott, M.B., and O'Malley, D.M. (2005). Prey tracking by larval zebrafish: Axial kinematics and visual control. Brain Behavior and Evolution 66, 177-196.

McLean, D.L., Fan, J., Higashijima, S., Hale, M.E., and Fetcho, J.R. (2007). A topographic map of recruitment in spinal cord. Nature 446, 71-75.

McLean, D.L., Masino, M.A., Koh, I.Y., Lindquist, W.B., and Fetcho, J.R. (2008). Continuous shifts in the active set of spinal interneurons during changes in locomotor speed. Nature Neuroscience 11, 1419-1429.

Mendell, L.M. (2005). The size principle: a rule describing the recruitment of motoneurons. Journal of Neurophysiology 93, 3024-3026.

Menelaou, E., and McLean, D.L. (2012). A Gradient in Endogenous Rhythmicity and Oscillatory Drive Matches Recruitment Order in an Axial Motor Pool. Journal of Neuroscience 32, 10925-10939.

Menelaou, E., VanDunk, C., and McLean, D.L. (2014). Differences in the morphology of spinal V2a neurons reflect their recruitment order during swimming in larval zebrafish. Journal of Comparative Neurology 522, 1232-1248.

Muto, A., Ohkura, M., Abe, G., Nakai, J., and Kawakami, K. (2013). Real-Time Visualization of Neuronal Activity during Perception. Current Biology 23, 307-311.

Myers, P.Z. (1985). Spinal motoneurons of the larval zebrafish. Journal of Comparative Neurology 236, 555-561.

Myers, P.Z., Eisen, J.S., and Westerfield, M. (1986). Development and axonal outgrowth of identified motoneurons in the zebrafish. Journal of Neuroscience 6, 2278-2289.

Ohta, Y., Dubuc, R., and Grillner, S. (1991). A New Population of Neurons with Crossed Axons in the Lamprey Spinal-Cord. Brain Research 564, 143-148.

Orger, M.B., Kampff, A.R., Severi, K.E., Bollmann, J.H., and Engert, F. (2008). Control of visually guided behavior by distinct populations of spinal projection neurons. Nature Neuroscience 11, 327-333.

Pedregosa, F., Varoquaux, G., Gramfort, A., Michel, V., Thirion, B., Grisel, O., Blondel, M., Prettenhofer, P., Weiss, R., Dubourg, V., *et al.* (2011). Scikit-learn: Machine Learning in Python. Journal of Machine Learning Research 12, 2825-2830.

R Core Team (2013). R: A Language and Environment for Statistical Computing. http://www.r-project.org/. (Vienna, Austria).

Ramachandran, P., and Varoquaux, G. (2011). Mayavi: 3D Visualization of Scientific Data. Computing in Science & Engineering 13, 40-50.

Roberts, A., Li, W.C., and Soffe, S.R. (2010). How neurons generate behavior in a hatchling amphibian tadpole: an outline. Frontiers in Behavioral Neuroscience 4, 16.

Robles, E., Laurell, E., and Baier, H. (2014). The Retinal Projectome Reveals Brain-Area-Specific Visual Representations Generated by Ganglion Cell Diversity. Current Biology 24, 2085-2096.

Saalfeld, S., and Tomancak, P. (2008). Automatic landmark correspondence detection for ImageJ. In Proceedings of the ImageJ User and Developer Conference, pp. 128-133.

Satou, C., Kimura, Y., and Higashijima, S. (2012). Generation of Multiple Classes of V0 Neurons in Zebrafish Spinal Cord: Progenitor Heterogeneity and Temporal Control of Neuronal Diversity. Journal of Neuroscience 32, 1771-1783.

Scheffer, L.K., Karsh, B., and Vitaladevun, S. (2013). Automated Alignment of Imperfect EM Images for Neural Reconstruction. In arXiv e-prints.

Schneider, C.A., Rasband, W.S., and Eliceiri, K.W. (2012). NIH Image to ImageJ: 25 years of image analysis. Nature Methods 9, 671-675.

Seligman, A.M., Wasserkrug, H.L., and Hanker, J.S. (1966). A New Staining Method (OTO) for Enhancing Contrast of Lipid-Containing Membranes and Droplets in Osmium Tetroxide-Fixed Tissue with Osmiophilic Thiocarbohydrazide (TCH). Journal of Cell Biology 30, 424-432.

Song, J., Ampatzis, K., Björnfors, E.R., and El Manira, A. (2016). Motor neurons control locomotor circuit function retrogradely via gap junctions. Nature 529, 399-402.

Svara, F., Kornfeld, J., Pfeiler, N., Nguyen, M., Stepanov, A., Pronkin, A., and Shatz, O. www.knossostool.org.

Tegner, J., Hellgren-Kotaleski, J., Lansner, A., and Grillner, S. (1997). Low-voltage-activated calcium channels in the lamprey locomotor network: Simulation and experiment. Journal of Neurophysiology 77, 1795-1812.

Trivedi, C.A., and Bollmann, J.H. (2013). Visually driven chaining of elementary swim patterns into a goal-directed motor sequence: a virtual reality study of zebrafish prey capture. Frontiers in Neural Circuits 7.

Tunstall, M.J., and Sillar, K.T. (1993). Physiological and developmental aspects of intersegmental coordination in Xenopus embryos and tadpoles. Seminars in Neuroscience 5, 29-40.

van der Walt, S., Colbert, S.C., and Varoquaux, G. (2011). The NumPy Array: A Structure for Efficient Numerical Computation. Computing in Science & Engineering 13, 22-30.

van Raamsdonk, W., Mos, W., Smit-Onel, M.J., van der Laarse, W.J., and Fehres, R. (1983). The development of the spinal motor column in relation to the myotomal muscle fibers in the zebrafish (Brachydanio rerio). I. Posthatching development. Anatomy and Embryology 167, 125-139.

Wallen, P., and Williams, T.L. (1984). Fictive locomotion in the lamprey spinal cord in vitro compared with swimming in the intact and spinal animal. Journal of Physiology 347, 225-239.

Walton, J. (1979). Lead Aspartate, an En-Bloc Contrast Stain Particularly Useful for Ultrastructural Enzymology. Journal of Histochemistry & Cytochemistry 27, 1337-1342.

Wang, W.C., and McLean, D.L. (2014). Selective responses to tonic descending commands by temporal summation in a spinal motor pool. Neuron 83, 708-721.

Wanner, A. https://github.com/adwanner/PyKNOSSOS.

Waxman, S.G., and Bennett, M.V. (1972). Relative conduction velocities of small myelinated and non-myelinated fibres in the central nervous system. Nature New Biology 238, 217-219.

Westerfield, M. (2007). A guide for the laboratory use of zebrafish (Danio rerio). The zebrafish book., 5th ed. edn (Eugene: University of Oregon Press).

White, J.G., Southgate, E., Thomson, J.N., and Brenner, S. (1986). The Structure of the Nervous System of the Nematode Caenorhabditis elegans. Philosophical Transactions of the Royal Society B 314, 1-340.

Wolf, E., Soffe, S.R., and Roberts, A. (2009). Longitudinal neuronal organization and coordination in a simple vertebrate: a continuous, semi-quantitative computer model of the central pattern generator for swimming in young frog tadpoles. Journal of Computational Neuroscience 27, 291-308.

Wyart, C., Del Bene, F., Warp, E., Scott, E.K., Trauner, D., Baier, H., and Isacoff, E.Y. (2009). Optogenetic dissection of a behavioural module in the vertebrate spinal cord. Nature 461, 407-410.

Yasargil, G.M., and Sandri, C. (1990). Topography and Ultrastructure of Commissural Interneurons That May Establish Reciprocal Inhibitory Connections of the Mauthner Axons in the Spinal-Cord of the Tench, Tinca-Tinca L. Journal of Neurocytology 19, 111-126.

Zucker, R.S. (1973). Theoretical Implications of Size Principle of Motoneuron Recruitment. Journal of Theoretical Biology 38, 587-596.